

Epoxy Based Nanodielectrics for High Voltage DC-Applications – Synthesis, Dielectric Properties and Space Charge Dynamics

Thomas ANDRITSCH

November 2010

Epoxy Based Nanodielectrics for High Voltage DC-Applications – Synthesis, Dielectric Properties and Space Charge Dynamics

Proefschrift

ter verkrijging van de graad van doctor
aan de Technische Universiteit Delft
op gezag van de Rector Magnificus Prof.ir. K.C.A.M. Luyben
voorzitter van het College voor Promoties,
in het openbaar te verdedigen,
op dinsdag 2 november 2010 om 10:00 uur
door

Thomas Michael ANDRITSCH

Diplom-Ingenieur TU Graz,
geboren te Innsbruck (Oostenrijk)

Dit proefschrift is goedgekeurd door de promotor:
Prof.dr. J.J. Smit

Samenstelling promotiecommissie:

Rector Magnificus	Voorzitter
Prof.dr. J.J. Smit	Technische Universiteit Delft, promotor
Dr.ir. P.H.F. Morshuis	Technische Universiteit Delft
Prof.dr. S.J. Picken	Technische Universiteit Delft
Ord.Prof. Dr.-Ing. J. Kindersberger	Technische Universität München
Prof.dr. A.S. Vaughan	University of Southampton
Prof.ir. L. van der Sluis	Technische Universiteit Delft
O.Univ.-Prof Dipl.-Ing.Dr. Dr.H.C. M. Muhr	Technische Universität Graz

This research was funded by the following companies:

Comet AG, Flamatt, Switzerland
Jensen Capacitors, Broendby, Denmark
PBF Electronics, Almelo, The Netherlands
Philips Healthcare DMC, Hamburg, Germany
Thales Electron Devices, Ulm, Germany
Thales, Hengelo, The Netherlands

ISBN: 978-90-5335-331-8

© by Thomas M. Andritsch, use for non-commercial and educational purpose permitted

Cartoon on page V printed with kind permission by *The Times* and Jonathan Pugh (<http://www.timesonline.co.uk> & <http://www.pughcartoons.co.uk>).

Cover: from sub-nanometre to sub-terametre (explanation on page 204).

Printing: Ridderprint grafisch bedrijf, Ridderkerk, the Netherlands



**"I always thought nanotechnology
was an iPod"**

Summary

There are two big frontiers on opposite sides of the size spectrum in the 21st century. Space exploration is on one end of the spectrum. The other side of the spectrum is the exploration of the nanoscale. In both cases we have limitations of how much of it we can see, even with the help of modern telescopes and microscopes. Nanotechnology has been inadvertently in use already for centuries. But only with recent advancement in imaging technology we are actually able to get a glimpse into the nanorealm and can comprehend its implications. Nanostructured materials for high voltage design and engineering have been an important research topic since the early 1990ies, and gained recognition by the end of the 20th century as first experimental results promised unbridled potential. It turned out soon, that nanocomposites can only reach their potential if the filler material is well distributed within the base material.

Main goal of the research described in this PhD thesis was to determine the influences of filler size, material and distribution on the DC breakdown strength, permittivity and space charge behaviour of nanocomposites. This should lay the groundwork for tailored insulation materials for HVDC applications. Examples for this are medical and industrial X-ray imaging, radar and cable terminations. In the course of this project a manufacturing process was devised, which enabled the fabrication of epoxy based nanocomposites with a good dispersion of different types of nanoparticles.

Models from literature, which explain the behaviour nanodielectrics exhibit, are discussed: electric double-layer model, intensity model, multi-core model and the interphase volume model. Based on these theories, a new model was devised for explaining the behaviour of epoxy based nanocomposites: the polymer chain alignment model. The underlying idea of this model is that the restructuring of the base polymer on the molecular scale, due to the presence of surface modified nanoparticles, plays a fundamental part in the properties of the bulk material. Each modified particle will act as centre for crosslinking of the polymer, leading to a rigid layer of polymer chains around each particle. These rigid layers have a much lower permittivity than both host and filler material, thus their presence

can easily be identified by dielectric spectroscopy, since the relative permittivity of the bulk material decreases. In literature it is shown, that the strong bonding of particles and host material due to the surface modification gives rise to improved resistance to partial discharges and electrical treeing. More energy is needed to break these bonds than it would be the case in unmodified polymers. The particles themselves can also act as recombination centres for electrons and holes, which travel between or along polymer chains. This has an effect on the space charge dynamics. Agglomerations of nanoparticles can nullify these effects however: it is explained how agglomerations can act as charge traps, lead to field enhancements and cause interfacial polarization.

Claims from theory are tested with three measurement methods: short term DC breakdown tests, dielectric spectroscopy and space charge measurement. It is shown that nanocomposites exhibit improved DC breakdown strength for very low fillgrades of 0.5 to 2 % by weight. Compared to the unmodified base material improvements of up to 80% could be measured. Dielectric spectroscopy reveals that the relative permittivity in nanocomposites is lower than of the host and filler materials, with a minimum at a fillgrade of approximately 2 % by weight. For higher fillgrades the permittivity of the composite increases depending on the ratio between the permittivity values of filler and host material. Above 2 wt.% the permittivity of the filler material starts to overshadow the low permittivity of the rigid layers around the particles. Results from space charge measurement with the pulsed electro-acoustic method show that the quality of particle dispersion has an impact on the charge intake. Based on these measurements it is concluded that particle agglomerations act as charge traps, while the amount of charges in nanocomposites with good particle dispersion is lower than in the unmodified epoxy. This confirms that the particles indeed act as recombination centres, actively mitigating charge buildup inside the material.

These results show why nanocomposites are very interesting for HVDC equipment. Space charges are a limiting factor for DC applications. Their reduction improves the reliability of the insulation system. The increased DC breakdown strength enables more compact high voltage equipment, respectively the utilization at higher field strengths. The work presented

here is a stepping stone on the way to industrial applications of nanostructured insulation material and fundament for further investigations on topics like nanofluids.

Samenvatting

Aan het begin van deze eeuw, zetten wij de eerste stappen in twee belangrijke onderzoeksgebieden, die op het eerste gezicht heel veel van elkaar verschillen. Aan de ene kant, de verkenning van de ruimte, aan de andere kant is er de nanotechnologie. In beide gevallen is het lastig om in deze gebieden te kijken, ondanks onze moderne telescopen en microscopen. Nanotechnologie heeft de reputatie revolutionair te zijn, maar kent eigenlijk al eeuwenlang toepassingen in ons dagelijks leven. Dankzij ontwikkelingen in de elektronenmicroscopie zijn wij nu in staat om inzicht te krijgen in de nog nieuwe nanowereld en om hun wetten te begrijpen. Sinds de jaren negentig, zijn in de hoogspanningstechnologie nano-gestructureerde materialen een belangrijk onderzoeksonderwerp. Deze materialen hebben sindsdien een hoge zichtbaarheid in de industrie gekregen, omdat verrassende resultaten uit experimenten ongekende nieuwe mogelijkheden voorspelden. Al snel bleek echter dat het potentieel van nanocomposieten alleen goed benut kon worden, als het vulmiddel zo gelijkmatig mogelijk in het basismateriaal verdeeld werd.

De belangrijkste doelstelling van het onderzoek dat in dit proefschrift beschreven wordt, was het onderzoeken van de invloed van de deeltjesgrootte, materiaal eigenschappen en de verdeling van de vulstof in nanocomposieten op de elektrische eigenschappen. Van deze elektrische eigenschappen zijn de voornaamste: de DC doorslagspanning, permittiviteit en de accumulatie van ruimtelading. Dit wordt als leidraad gebruikt om isolatiematerialen 'op maat' voor hoogspannings-applicaties te ontwikkelen. Voorbeelden van deze toepassingen zijn computertomografie, industriële X-ray apparatuur, radar en kabeleindsluitingen. Tijdens dit project is een methode voor de productie van nanocomposieten op basis van epoxy ontwikkeld, waarmee een goede verdeling van verschillende soorten nanodeeltjes wordt bereikt.

Modellen uit de literatuur, die proberen het gedrag van nanodielektrika te verklaren worden behandeld: het model van de elektrische dubbellaag, het intensiteitsmodel, het multi-core model en het interphase volume model. Uit deze theorieën is een nieuw model ontwikkeld, om het gedrag van

op polymeren gebaseerde nanocomposieten te verklaren: het PCA model. De idee achter dit model is dat de aanwezigheid van nanodeeltjes met gemodificeerde oppervlakken een herstructurering van het basismateriaal op moleculair niveau veroorzaakt. Deze herstructurering speelt een fundamentele rol met betrekking tot de eigenschappen van het materiaal. Elk gemodificeerde deeltje fungeert als een centraal punt in de ketenvorming in de nanocomposiet. Dit leidt tot een rigide laag van polymeerketens, die zich rond elk nanodeeltje vormen. Deze rigide lagen hebben een veel lagere permittiviteit vergeleken met zowel het basispolymeer als de vulstof. De aanwezigheid van deze lagen kan daarom gemakkelijk met behulp van diëlektrische spectroscopie worden geïdentificeerd. In de literatuur zijn er aanwijzingen dat de sterke bindingen van de gemodificeerde deeltjes met de basispolymeren op moleculair niveau leiden tot een verbeterde weerstand tegen deelontladingen en tegen de vorming van elektrische bomen. Vergeleken met het polymeer zonder nanodeeltjes, is er een veel hogere energie nodig om deze banden te verbreken. De nanodeeltjes zijn ook centra voor recombinatie van vrije elektronen en gaten, die zich tussen en langs de polymeerketen bewegen. Dit heeft positieve effecten op de dynamica van de ruimtelading. Echter, door agglomeraties van nanodeeltjes kunnen deze positieve effecten teniet gedaan worden. Agglomeraten van nanodeeltjes leiden tot veldverhogingen in het isolatiemateriaal. Bij grote agglomeraties kan er ook sprake zijn van grensvlak-polarisatie. Dit leidt vervolgens tot een onregelmatige distributie van het elektrische veld.

Dit model wordt getoetst met drie methoden: tests van de DC doorslagspanning, diëlektrische spectroscopie en metingen van de ruimtelading. Er wordt aangetoond dat nanocomposieten met zeer lage vullingen van 0,5 tot 2 gew. % de hoogste DC doorslagspanning hebben. Vergeleken met het onge vulde polymeer zijn er verbeteringen van 80% gemeten. Uit diëlektrische spectroscopie blijkt dat de permittiviteit van nanocomposieten lager is dan die van zowel het basismateriaal als het vulmateriaal. De laagste permittiviteit werd gemeten bij een vulratio van ongeveer 2% van het gewicht. Voor hogere vulraties neemt de relatieve permittiviteit weer toe, omdat het effect van de rigide lagen overstemd wordt door de hogere permittiviteit van het vulmiddel. Uit metingen van de ruimtelading blijkt dat de kwaliteit van de dispersie van de deeltjes de elektrische ladingsoptname

beïnvloedt. Op basis van deze metingen wordt geconcludeerd, dat agglomeraten leiden tot lokale elektrische oplading in het nanocomposiet conform de verwachtingen gebaseerd op de geraadpleegde theorie. De hoeveelheid opgenomen ruimtelading in composieten met een homogene verdeling van nanodeeltjes is lager dan in gewone onbehandelde epoxy. Dit doet vermoeden dat de nanodeeltjes door recombinitie actief de ladingsopname in het materiaal voorkomen.

Deze resultaten laten zien waarom nanocomposieten zeer aantrekkelijk voor HVDC toepassingen kunnen zijn. Ruimteladingen zijn namelijk een limiterende factor voor DC toepassingen en de vermindering hiervan door nanocomposieten verhoogt de betrouwbaarheid van het isolerend materiaal. De hogere doorslagspanning maakt compactere hoogspanningsapparatuur en/of het gebruik van hogere elektrische veldsterktes mogelijk. Het hier gepresenteerde werk en opgebouwde kennis is een springplank naar de industriële toepassing van nano-isolatiematerialen, welke tevens kan dienen als basis voor verdere studies over onderwerpen zoals nano-vloeistoffen.

Zusammenfassung

Zu Beginn dieses Jahrhunderts sehen wir uns zwei großen Forschungsgebieten gegenüber, welche auf den ersten Blick unterschiedlicher nicht sein könnten. Auf der einen Seite ist die Erkundung des Weltraums, auf der anderen Seite steht die Nanotechnologie. In beiden Fällen sind uns trotz moderner Teleskope und Mikroskope Grenzen auferlegt diese Bereiche zu beobachten. Nanotechnologie hat den Ruf des revolutionären, findet jedoch bereits seit Jahrhunderten Anwendungen im täglichen Leben. Doch erst dank einer Reihe von Fortschritten in der Elektronenmikroskopie sind wir nun in der Lage, einen Einblick in die noch immer neuartig erscheinende Nanowelt zu erhalten und seine Gesetze zu verstehen. Nanostrukturierte Materialien sind in der Hochspannungstechnik seit den frühen 1990ern ein wichtiges Forschungsthema. Sie erlangten in dieser Zeit einen hohen Bekanntheitsgrad in der Branche, als überraschender Versuchsergebnisse unbändiges Potenzial versprochen. Es stellte sich bald heraus, dass Nanokomposite ihr Potenzial nur dann voll ausschöpfen können, wenn das Füllmaterial möglichst gleichmäßig im Grundmaterial verteilt ist.

Hauptziel des Forschungsprojektes, welches im Rahmen dieser Dissertation beschrieben wird, ist es die Einflüsse von Größe, Materialeigenschaften und Verteilung des Füllstoffes in Nanokompositen auf elektrische Eigenschaften, wie die Gleichspannungs-Durchschlagsfestigkeit, Permittivität und das Raumladungsverhalten, zu bestimmen. Dies sollte den Grundstein liefern um maßgeschneiderte Isolierstoffe für Hochspannungs-Gleichstrom-Anwendungen herzustellen. Beispiele für solche Anwendungen sind Computertomographie, Röntgenapparate und Radar. Im Zuge dieser Arbeit wurde ein Verfahren zur Herstellung von Nanokompositen auf Epoxid-Basis entwickelt, welches eine gute Verteilung verschiedener Arten von Nanopartikel ermöglicht.

Theoretische Modelle aus der Literatur werden vorgestellt, die das Verhalten von Nanodielektrika zu erklären versuchen: das Modell der elektrischen Doppelschicht, das Intensitäten-Modell, das Multi-Core Modell und das Interphasenvolumen Modell. Basierend auf diesen Modellen, wurde ein neues Modell zur Erklärung des Verhaltens von auf Polymeren basieren-

den Nanokompositen entwickelt: das PCAM (polymer chain alignment model). Der Gedanke hinter diesem Modell ist, dass sich aufgrund der Anwesenheit von Nanopartikeln mit modifizierten Oberflächen eine Umstrukturierung des Basispolymers auf molekularer Ebene ergibt. Diese Restrukturierung spielt eine fundamentale Rolle für die Eigenschaften des Werkstoffes. Jedes Teilchen, dessen Oberfläche entsprechend modifiziert wurde um kompatibel mit dem Polymer zu sein, wird zu einem Vernetzungszentrum im Nanokomposit. Dies führt zu einer steifen Schicht von Polymerketten, welche um jedes Teilchen angeordnet sind. Diese starren Schichten haben eine viel geringere Permittivitätszahl als sowohl das Grundpolymer als auch der Füllstoff. Die Anwesenheit dieser Schichten kann deshalb leicht mit Hilfe dielektrischer Spektroskopie identifiziert werden. In der Literatur finden sich Hinweise, dass die starken Bindungen der modifizierten Teilchen zum Basispolymer auf molekularer Ebene zu verbessertem Widerstand gegenüber Teilentladungen, sowie der Bildung von elektrischen Bäumen führen. Im Vergleich zum unmodifizierten Polymer ist nämlich eine viel höhere Energie notwendig, um diese Bindungen aufzubrechen. Die Nanopartikel dienen auch als Rekombinationszentren für freie Elektronen und Löcher, welche sich zwischen bzw. entlang der Polymerketten bewegen. Dies hat positive Auswirkungen auf die Raumladungsdynamik. Durch Agglomerationen von Nanopartikeln werden diese Effekte jedoch zunichte gemacht: Agglomerate von Nanopartikeln führen dazu, dass das Isoliermaterial lokal mit Ladungen angereichert wird, sowie zu Grenzflächenpolarisation. Dies führt in weiterer Folge zu einem unregelmäßigen Verlauf des elektrischen Feldes.

Annahmen aus der Theorie werden mit drei Messmethoden überprüft: Tests der Gleichspannungs-Durchschlagsfestigkeit, dielektrischer Spektroskopie und Raumladungsmessung. Es wird gezeigt, dass Nanokomposite für sehr niedrige Füllgrade von 0,5 bis 2 gew.% eine erhöhte Gleichspannungsdurchschlagsfestigkeit haben. Im Vergleich zum unmodifizierten Basispolymer wurden Verbesserungen um bis zu 80% gemessen. Dielektrische Spektroskopie zeigt, dass die Permittivitätszahl von Nanokompositen niedriger ist, als jene von sowohl dem Basismaterial als auch dem Füllstoff. Ein Minimum für die Permittivitätszahl konnte bei einem Füllgrad von etwa 2 Gew.% gemessen werden. Für höhere Füllgrade steigt die relative

Permittivität wieder, da bei mehr als 2% die höhere relative Permittivität des Füllstoffes den die Permittivität vermindernenden Effekt der starren Schichten überschattet. Ergebnisse der Raumladungsmessung zeigen, dass die Qualität der Partikeldispersion Auswirkungen auf die Ladungsaufnahme hat. Basierend auf diesen Messungen wurde der Schluss gezogen, dass Agglomerate zu lokaler Ladungsanreicherung in den Kompositen führen, was in der Theorie vermutet wurde. In Nanokompositen mit gleichmäßiger Partikelverteilung ist die Höhe der aufgenommenen Raumladung hingegen geringer als in unmodifiziertem Epoxidharz. Dies deutet darauf hin, dass es sich bei den Nanopartikeln um Rekombinationszentren handelt, welche aktiv eine Aufladung im Inneren des Materials verhindern.

Diese Ergebnisse zeigen, warum Nanokomposite sehr interessant für Hochspannungs-Gleichspannungs-Anwendungen sind. Raumladungen sind ein einschränkender Faktor für Gleichspannungs-Anwendungen. Ihre Reduktion verbessert die Zuverlässigkeit des Isolierstoffes. Die erhöhte Durchschlagsfestigkeit ermöglicht kompaktere Hochspannungsanlagen, bzw. die Nutzung bei höheren elektrischen Feldstärken. Die hier vorgestellte Arbeit ist ein Sprungbrett auf dem Weg zur industriellen Anwendung von nanostrukturiertem Isolationsmaterial. Sie soll als Grundlage für weitere Untersuchungen zu Themen wie zum Beispiel Nanofluide dienen.

CONTENTS

1. Introduction	1
1.1. Nanotechnology?	1
1.1.1. Definitions	2
1.1.2. Nanotechnology in daily life	4
1.1.3. Nanotechnology in high voltage and power engineering	5
1.1.4. State of the art	7
1.1.5. Nanotoxicity	8
1.2. Goals of this research	9
1.3. Approach	9
2. Synthesis of Nanocomposites	11
2.1. An Overview of common Polymers in Electrical Engineering	12
2.1.1. Epoxies	13
2.2. Fillers for Polymer based Insulation Material	14
2.3. Materials used	15
2.3.1. Host material	15
2.3.2. Filler materials	15
2.3.3. Coupling Agent	16
2.4. Preparation procedure	16
2.4.1. Particle preparation	18

2.4.2. Surface functionalization	19
2.4.3. Mixing	22
2.4.4. Casting and Curing	23
2.4.5. Validation of the particle dispersion	23
3. Theory and Modelling	29
3.1. Conventional Theory – Limitations when dealing with Nanocomposites	30
3.2. Topology of Nanocomposites	30
3.2.1. Intramolecular interactions	31
3.2.2. Intermolecular interactions	31
3.3. Theories for describing Nanocomposites	33
3.3.1. Electric double layer	33
3.3.2. Intensity model	34
3.3.3. Multi-core model	36
3.3.4. Interphase Volume Model	38
3.4. Polymer Chain Alignment Model	40
3.4.1. Philosophy (PCAM in a nutshell)	40
3.4.2. Assumptions and Definitions for this model	43
3.4.3. Morphology of NC	43
3.4.4. Layer Volume Calculation	45
3.4.5. Effects of Chain Alignment	50
3.4.6. Influence of the Material	52
3.4.7. Influence on the dielectric properties of the bulk material	55
4. Breakdown Strength	59
4.1. Measurement Setup	60
4.2. Sample Preparation	60
4.3. Analysis	61
4.4. Filler Type	61
4.5. Fillgrade	62
4.6. Filler Size	68
4.7. Summary	70

5. Dielectric Response	71
5.1. Test setup	72
5.2. Sample Preparation	72
5.3. Dielectric Response of Unfilled Epoxy	73
5.4. Impact of curing time and particle modification	74
5.5. Filler Type	77
5.6. Fillgrade	81
5.7. Filler Size	85
5.8. Summary	88
6. Space Charges	91
6.1. Measurement Principle	91
6.1.1. Measurement setup	92
6.1.2. Measurement process	92
6.2. Sample Preparation	93
6.2.1. Spatial resolution	93
6.3. Space Charge Parameters	94
6.3.1. Field enhancement factor	95
6.4. Space Charge Accumulation	95
6.5. Space Charge Profiles	98
6.5.1. Unmodified epoxy	98
6.5.2. MgO Nanocomposites	99
6.5.3. AlN and Al ₂ O ₃ Nanocomposites	103
6.6. Charge Depletion During Depoling	106
6.7. Electric Field	107
6.8. Discussion	107
6.9. Summary	108
7. Industrial Processing	111
7.1. Upscaling	112
7.1.1. Different solvent	113
7.1.2. Seperate particle preparation	114
7.1.3. Masterbatch	115
7.1.4. In-situ synthesis	115
7.1.5. Dispersion in final products	117

Contents

7.2. Possibilities for the near future	118
7.2.1. Nano-micro composites	118
7.2.2. Field-structured nanocomposites	118
7.2.3. Nanofluids	118
8. Conclusions	121
9. Recommendations	125
A. Specimen Characterization	127
A.1. X-ray Diffraction	127
A.2. Laser Diffraction	129
A.2.1. Sample preparation	129
A.2.2. Results	129
A.2.3. Summary	130
A.3. Thermogravimetric Analysis	133
A.3.1. Validation of the surface functionalization	133
A.3.2. Particle concentration profile	134
A.4. Electron Microscopy	135
A.4.1. TEM Analysis of NC	137
A.4.2. Quantitative Analysis of NC with SEM	140
A.4.3. Summary	141
A.5. Dynamic Mechanical Thermal Analysis	142
B. Experimental Setup	145
B.1. Dielectric Spectroscopy	145
B.1.1. Measurement principle	145
B.1.2. Measurement setup	145
B.1.3. Sample Preparation	149
B.2. Space Charge Measurement	149
B.2.1. Measurement principle	150
B.2.2. PEA Setup	151
B.2.3. Evaluation of Space Charge Evolution	154
C. Health and Safety Issues	159

Contents

D. Zeta potential

161

CHAPTER 1

INTRODUCTION

There's plenty of room at the bottom.

-Richard Feynman

When the crusaders tried to recapture Jerusalem from the Muslims, they found themselves on the wrong end of swords made from Damascus steel. Strong but still flexible enough to be bent from hilt to top, these formidable weapons quickly gained their reputation for being able to cut through swords and armor of the European knights alike. The secret of producing these swords got lost over the centuries. But the secret behind the remarkable quality of Damascus steel has been identified as carbon nanotubes [1]. The Muslim swordsmiths of the 17th century were inadvertently using nanotechnology.

1.1. Nanotechnology?

The concept of nanotechnology was first introduced by Richard Feynman in his lecture *There's Plenty of Room at the Bottom*, at an American Physical Society meeting at Caltech in 1959 [2]. Inspired by the ongoing minia-

turization, he was talking about the possibility of direct manipulation of individual molecules or atoms. The term nanotechnology was first coined by prof. Norio Taniguchi in 1974, to describe semiconductor processes like thin film deposition or ion beam milling. For him, '*Nano-technology*' mainly consists of the processing of separation, consolidation, and deformation of materials by one atom or one molecule [3]. In 1984 the term nanocomposite (NC) was mentioned the first time by Roy and Komarneni, meaning a "polymeric product consisting of two or more phases of nanometric sizes" [4]. Since then the term *nanocomposite* has been universally accepted as describing a wide range of materials, involving structures in the nanometer size range, e.g. in [5].

But it was in the early 80ies that nanoscience could come into being with the birth of cluster science and the invention of the scanning tunneling microscope (STM) by Gerd Binnig and Heinrich Rohrer at IBM Zürich [6]. This lead to the discovery of the C₆₀ fullerene – also called Buckminster fullerene – in 1985 and the wide acclaim of the carbon nanotube (CNT) short after. The discovery of CNT actually predates Richard Feynman's talk: Russian scientists Radushkevich and Lukyanovich published transmission electron microscopy (TEM) images of CNT already in 1952 [7]. But since the publication was written in Russian and due to the scarce availability of Russian journals in the cold war era, this discovery went unnoticed by the western dominated science community. In 1995 the first single-electron transistors based on CNT were shown by research groups at UC Berkley [8] and TU Delft [9].

1.1.1. Definitions

The fundamental aspect of nanotechnology is obviously size: we usually speak about nanostructures, when at least one spacial dimension is below 100 nm. Table 1.1 gives an overview of small scale structures as point of reference. Nanostructures and devices usually utilize the characteristic effects and phenomena between atoms and clusters of atoms and molecules, especially surface effects. Figure 1.1 illustrates how the interface area gets more important, the smaller the particles become. More about this in Chapter 3 on page 29. Because of the interfacial area becoming more

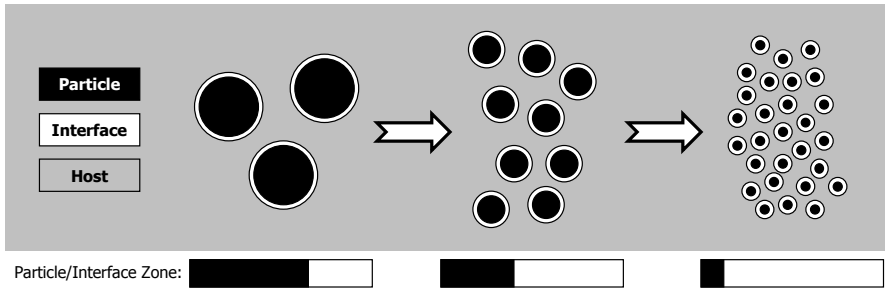


Figure 1.1.: Illustration of how the ratio of the filler material to the interfacial area changes with the size of the filler.

dominant, nanomaterials often show novel, or at least unexpected, properties. Last but not least important aspect of nanotechnology is of course the manipulation and manufacturing of aforementioned structures and devices.

Agglomerations of nanoparticles (NP) in the micrometer range can nullify the beneficial effects that come with the small filler size. But since it is not certain at which agglomeration size nanocomposites lose their effects, there is still controversy about what can be called nanocomposite. In the course of this work we use the following terminology:

Nanocomposite (NC) is a binary system consisting of a host material with a filler material whose size in at least one dimension does not exceed 100 nm on average. This includes agglomerations which must not exceed 100 nm on average.

Conventional filled composite (CFC) is a composite in which the filler material exceeds 500 nm on average in each dimension. This limit was set since it was suspected that NC lose their special properties if particles or agglomerates exceed 500 nm.

Mesocomposite (MC) is similar to NC but with a filler material whose dimensions are between 100 and 500 nm on average. Agglomerations also must not exceed 500 nm on average. This depicts composite materials that are on the borderline between NC and CFC.

Table 1.1.: Examples of small-scale structures and events, taken from [5]

Object	Dimension in nm
Red blood cell	6000-8000
Electric tree length in polymer	2000-5000
UV Spectrum (upper wavelength)	400
Mean free path in gas (electron)	200
X-rays	100-0.1
Aerogel particle size	10
Coherence length (Nb-Ti)	4
Cell membrane thickness	3
Carbon nanotube diameter	1
Silicon wafer roughness	0.73
Polyethylene monomer dimension	0.74; 0.493; 0.253
Ionic radius of Al	0.252
de Broglie wavelength (electron)	0.1
Atomic radius	0.1
Nucleus radius	10^{-5}
Electron radius	10^{-7}

Nano-micro-composite (NMC) is a composite consisting of a host material and two filler materials with different average size. In this case one filler material would be less than 100 nm on average while the other would have dimensions exceeding 500 nm in all dimensions.

Nano-meso-composite (NSC) is a composite consisting of a host material and two filler materials with different average size. In this case one filler material would be less than 100 nm on average while the other would have a size above 100 but not exceeding 500 nm in all dimensions.

This terminology applies for spherical particles or particles with an aspect ratio similar to spheres.

1.1.2. Nanotechnology in daily life

What is curious about nanotechnology is that it is surrounding us in daily life, without most people noticing it. Self-evident in the field of electron-

ics, where 32 nm CMOS structures can already be found in microprocessors [10]. The next step are CMOS structures with 22 nm, which are in development right now. But similar to the inadvertent use of CNT in Damascus steel, there are examples of NC in earlier stages of industrialization. In the 1860ies tire manufacturers mixed carbon black into their rubber compound, which by virtue of it's high surface area, surface energy and mechanical properties significantly reinforced the rubber. This makes the rubber tire the first commercialy available polymer nanocomposite. Another well known nanoscale reinforcement available in the early twentieth century is fumed silica, which has typically an average grain size between 7 and 14 nm [11]. It can be found in a variety of everyday products, ranging from toothpaste and cosmetics to milkshakes. Ultrafine precipitated calcium carbonate (PCC) is another example. PCC acts as a functional additive in sealants, adhesives, plastics, rubber, inks, paper, pharmaceuticals, nutritional supplements and many other applications and has typically dimensions of less than 100 nm.

The first company that knowingly utilized polymer nanocomposites in commercial products was Toyota. After issuing a patent on polyamide based NC filled with layered silicate in 1988 [12], NC were used as timing belt covers from 1993 on. By 2001 Toyota produced body panels and bumpers containing nanoclay, with other automakers following suit [13].

In mainstream media nanotechnology is mostly present in the form of so called assemblers. The idea of these self replicating nanomachines gained notoriety when Drexler envisioned a future built on atoms and molecules [14]. They have been prominent in books [15], tv series [16], movies [17] and video games [18] ever since. Most depictions in mainstream media show nanotechnology as a powerful tool which is very dangerous when in the wrong hands. But assemblers remain science fiction, very much like the narratives involving them.

1.1.3. Nanotechnology in high voltage and power engineering

On the first glance power engineering with its large structures and nanotechnology with exploitation of effects on the nanoscale don't seem to overlap much. On a second glance however, the possibilities of nanotechnology

in high voltage and power engineering are manifold. The possibilities range from utilization of new materials to evolution of existing solutions. One example is the Helianthos project, which utilizes nanolayers on a flexible substrate to create novel solar cells [19, 20]. Nanofluids based on either conventional transformer oil or vegetable oil can be used to quickly replace oil of power transformers. Due to their indicated improvement in terms of e.g. streamer propagation this is an easy way to improve long term stability of power transformers [21, 22].

Focus of this work is the improvement of polymer based solid dielectrics. From a theoretical standpoint reinforcement of polymers with CNT sounded very promising, since individual CNT offer mechanical strength, modulus and strain values many times larger than steel. Initial attempts at fabricating NC with CNT did not result in the expected level of performance. Instead, the NC properties were often inferior to the neat polymer. This originated in agglomerations of the nanofibres and bad interfaces at the nanoscale. The polymer matrix needs to bond to the graphene surface of CNT. But since the surface energy of nanotubes is very low, surface modification would be needed. But, the functional groups of the surfactant might damage the graphene lattice. Thus polymer NC with CNT failed to deliver the promises made by the individual tubes.

Instead NC with nanosized grains of already known filler material (e.g. alumina, zinc oxide or silica) gained notoriety within electrical engineering. In 1994 Lewis published *Nanometric Dielectrics*, which raised awareness for polymer based NC [23]. More about the intensity model he proposed in Section 3.3.2 on page 34.

Beside aforementioned CNT-NC, early research interest was focused on PE based insulation with nanoclay filler. The simple reason for this is that handling and properties of nanoclay were already known to material scientists. Soon other filler materials followed, mainly commonly known and used material like alumina or zinc oxide with nanoscale grain size. Promising initial results fueled the motivation of researchers involved in NC, e.g. leading to an exponential increase in publications with the keyword *nanotechnology* in the *compendex engineering village 2* database since 1993 [24].

1.1.4. State of the art

Initial findings about nanodielectrics seemed like magic, everything appeared possible. We are able to identify the working principles behind nanocomposites better now, yet still many questions remain unsolved [25].

Resistance to partial discharges (PD) has been repeatedly shown to increase considerably in NC [26, 27, 28]. The reason for the high PD resistance seems to be the strong bonds between polymer host and nanoparticles [29, 30]. Much more energy is needed to break these bonds as it would be in unfilled polymer or CFC. Similar reasons are believed to lead to increased resistance to electrical treeing [31, 32] and water treeing [33]. Other research groups showed that NC show increased resistance to HV arcing [34, 35].

When it comes to the dielectric breakdown strength (BD), it is still not perfectly clear how far nanoparticles grant an improvement. Nanocomposites showed both significant improvement [36, 37], as well as insignificant changes [38, 39] and even indication for BD reduction [40] for AC voltages. However, the DC BD strength has been shown to improve significantly for various nanocomposites [41, 38, 42].

Beside improved DC breakdown strength, the amount of space charges has also been shown to be reduced for certain NC [43, 44]. Especially magnesium oxide shows large potential for HVDC applications [45], for example HVDC cables made from low-density polyethylene with magnesium oxide nanofiller [46].

Thermal properties are another hot topic regarding NC. Improved thermal endurance [47] and thermal conductivity [48, 49] of dielectrics allow an increased workload of electrical machines and a more compact design. Improved flame retardancy is important for safety reasons [50, 51, 52].

Besides NC, we also see hybrids emerging that combine nano- and conventional sized fillers, dubbed NMMC for "nano-micro-mixture composite" [53, 54]. It has been shown that introduction of nanoparticles to a CFC can lead to an improvement of the AC breakdown strength [55]. More on hybrid materials in Chapter 7.

Considerable effort has been invested in understanding the role of nanofillers in both electrical tree initiation and growth [56]. Models that should

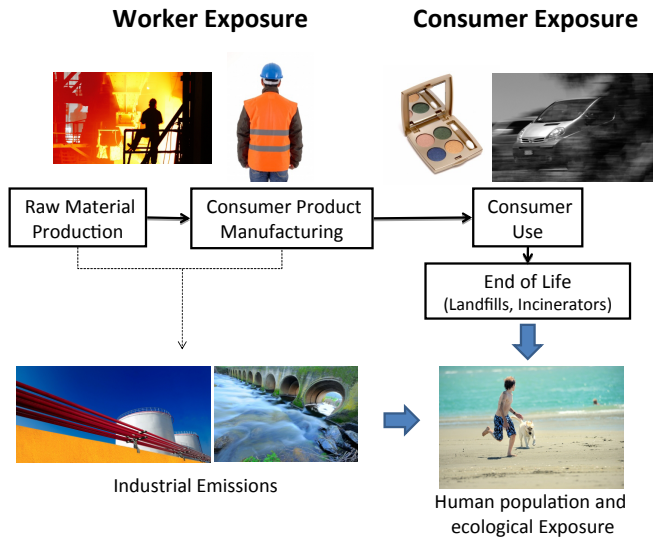


Figure 1.2.: Life cycle perspective risk assessment. Images: Suat Eman and Federico Stevanin / FreeDigitalPhotos.net

explain the behaviour of polymer based NC dielectrics emerge [57]. The role that the underlying chemistry plays is also explored [58]. More information about analytical models can be found in Chapter 3.

After years of focusing on solid insulation, the topic of nanoliquids gains notoriety. Transformer-oil based nanoliquids with conductive nanoparticles have experimentally shown to have higher positive voltage breakdown levels than conventional transformer oil [59]. Fullerene-doped insulation liquids show reduced viscosity, which would enable the use of narrower cooling channels [60].

1.1.5. Nanotoxicity

The intentional use of nanoparticles in consumer products is steadily increasing. Uncertainties in health and environmental effects associated with exposure to engineered nanomaterials – and handling of the base materials – raised questions about such exposures. The EPA nanotechnology

white paper [61] used a life cycle perspective to risk assessment regarding nanomaterials to identify, as illustrated in Figure 1.2. According to [61] the overall risk assessment approach used for conventional chemicals is generally applicable for nanomaterials. More information can be found in Appendix C.

1.2. Goals of this research

The main goal of this thesis is to determine the influences of filler material, size, surface modification and distribution within the host material on the dielectric properties of nanodielectrics. Therefore we build composites from scratch, since getting to know the individual building blocks of the material makes it easier to identify the impact they have on the dielectric properties of the overall material. The influences mentioned above on the major electrical properties, which are usually considered in selecting DC insulation systems, were determined. These properties are:

- The electric strength
- The relative permittivity and the dielectric loss, represented by the loss tangent, $\tan(\delta)$
- The space charges, which are linked to ageing processes and breakdown in polymers used for HVDC applications

From this a model should be derived, that helps comprehending the influence of nanoparticles on dielectric properties of a polymeric host material. The long term goal is the creation of tailored insulation material.

1.3. Approach

Early on the decision was made to investigate epoxy based nanocomposites. The main reason for this was that our industry partners use epoxy for various applications. Initially it was thought of receiving nanocomposites from third party companies. But the companies in question were not generous with information about the processes involved in creating

nanocomposites. Since the influences of the manufacturing stage on the dielectric properties of nanocomposites are very complex, it was important to have in-depth information about the synthesis of the insulation material.

Therefore it was concluded to start with the synthesis in cooperation with Delft ChemTech. This led to precise knowledge about the later investigated samples, and had the additional advantage of being independent from suppliers. Chapter 2 on page 11 describes the synthesis in detail.

Chapter 3 (page 29) sheds a light on the theory behind nanocomposites. After laying down the basics and an overview of theories about nanodielectrics, our own take on the subject matter is presented. This theory attributes the unique behavior of polymer nanocomposites to large extents to the change of the host material through introduction of surface functionalized nanoparticles.

Dielectric properties were investigated with three methods in the subsequent chapters:

- DC breakdown test (Chapter 4, page 59)
- Dielectric spectroscopy (Chapter 5, page 71)
- Space charge measurement (Chapter 6, page 91)

Since nanocomposites are still not common in electrical engineering, and high voltage engineering in particular, Chapter 7 (page 111) shows concepts of how nanodielectrics can be introduced into HV engineering. It also tries to envision to what degree nanotechnology can change HV engineering in the upcoming years. The subsequent Chapters 8 (page 121) and 9 (page 125) conclude this work and show interesting new directions for research on this topic.

CHAPTER 2

SYNTHESIS OF NANOCOMPOSITES

Research is what I'm doing when I don't know what I'm doing.

-Wernher Von Braun

Even binary, thus relatively simple, nanodielectrics exhibit very complex dielectric behaviour. There are a number of factors which are contributing to the properties of a nanodielectric, including:

- Particle size
- Aspect ratio
- Particle dispersion
- Host and filler material
- Surface functionalization

Since there are so many variables, it is of high importance to know about the chemistry involved when dealing with nanocomposites. The influence of the surface functionalization has been shown early on [58]. Receiving composites from e.g. an industry partner without exact knowledge of the

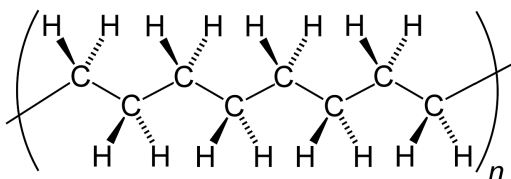


Figure 2.1.: Illustration of the polymer backbone of PE, consisting of a chain of carbon atoms.

composition of the sample results in a black box-approach when analyzing the results. As it will be shown in Chapters 4-6, even small changes in the composition of the sample or variations of the manufacturing process can have a profound effect on the dielectric properties. Therefore it was of high priority that we conduct the synthesis of the nanocomposites by ourselves, so that we are able to correlate the influences of the materials and the manufacturing stage with the measurement results.

2.1. An Overview of common Polymers in Electrical Engineering

Polymers consist of long-chain macromolecules with repeating monomer units. A polymer is usually named by putting the prefix 'poly' in front of the repeating unit. For example polyethylene, which consists of repeating ethylene units. Many polymers used in electrical engineering are based on a carbon linkage along the length of the polymer, forming the 'backbone', as illustrated in Figure 2.1 for PE. These polymers are known as homopolymers. Notable examples are the already mentioned polyethylene (PE), polytetrafluorethylene (PTFE), polyvinyl chloride (PVC) and polymethyl methacrylate (PMMA). Heterochain polymers have their backbone replaced by other elements. For example polyesters, which are formed from glycols and dicarboxylic acids, polyamide (PA) or polycarbonate (PC).

Simple polymer chains may form branches off the main chain, this is commonly found in PE. Branching can be provoked or inhibited by the conditions during polymerisation. Branching reduces the molecular pack-

aging, thus lowers the density of the polymer. In case of PE it leads to low-density polyethylene (LDPE), which is mechanically inferior to its non-branched counterpart, high-density polyethylene (HDPE), but maintains excellent dielectric properties.

Aside branching there is another important structural phenomenon: cross-linking. In this case polymer chains are joined by (sometimes polymeric) molecules which form connecting branches. Cross-linked polymers form essentially one gigantic molecule. Because of this cross-linked polymers become rubber-like rather than liquid above the melting point T_m (semicrystalline polymer) or glass transition temperature T_g (amorphous polymer). These polymers are called thermoset, since their shape is irreversible ('set') once the crosslinking process (curing) started. Rubbers are a subset of thermosets with a T_g below room temperature. Cross-linked polymers can be formed in three ways:

Catalyst: by incorporating a catalyst into the polymer after the polymer has been moulded or cast.

Chemical hardener: epoxy resins (ER) are a family of thermoset polymers in which two components are mixed to eventually form a glassy compound.

Radiation: this process can only be used in thin sections and may cause material degradation during processing. Thus the applicability is limited.

2.1.1. Epoxies

Epoxies are thermoset polymers in which the end groups contain the three-membered epoxide ring (see Figure 2.2.a.), often in a diepoxide structure (Figure 2.2.b.) where R is commonly bisphenol-A (Figure 2.2.c.). The epoxide rings are strained due to the equilateral triangle the atoms form and the resulting intermolecular forces, which makes the epoxy group highly reactive. The curing agent (commonly called 'hardener') opens the epoxide ring and interconnects the polymer chains. The high chemical re-

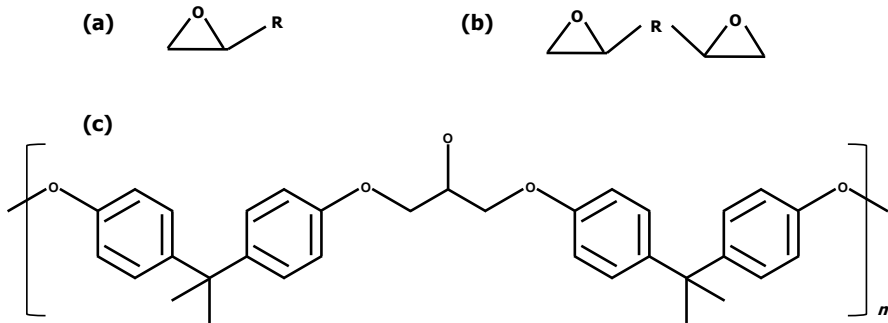


Figure 2.2.: Chemical structure of the epoxide ring (a), the diepoxide structure (b) and bisphenol-A (c).

activity and large number of epoxide rings can lead to an extensive network of connections, leading to high mechanical strength and rigidity.

2.2. Fillers for Polymer based Insulation Material

Polymeric insulation is very common in electrical engineering these days. For every application it is possible to choose a polymer fitting the requirement profile from a large variety of available materials. But the desired properties are not only influenced by the base polymer, but also by the fillers and additives that are mixed in. The main difference between filler and additive is usually the amount of material by weight, compared to the base polymer. Since the classification varies and is not entirely clear from literature, and due to the fact that we only use very low fillgrades with nanoparticles, there is no distinction between filler and additives in the following.

Fillers are often fine grained particles or fibres, which can be based both on organic and inorganic materials. Typically these particles and fibres have a size in the range of micrometers, thus called conventional sized fillers hereafter. Composites with conventional sized fillers are labelled conventional filled composites (CFC) below. Filler materials serve many purposes, for example improving mechanical strength and thermal prop-

erties. The high loads of silicon dioxide (SiO_2) in epoxy used for e.g. cast resin transformers have the additional benefit of cost reduction, since the filler material is cheaper than the host material by a substantial amount.

2.3. Materials used

2.3.1. Host material

Base material for the compounds investigated is epoxy resin. The resin consist of a diepoxide-bisphenol-A type CY231 from Huntsman, which has a chemical structure as indicated in Figure 2.2. As curing agent we used an anhydrite hardener (type HY925, also from Huntsman).

The decision to use this epoxy resin system was made because it can be mixed at room temperature, whereas thermoplastic materials require elevated temperatures for machining. Reasons for using this specific host material were the long potting time at room temperature and the easy availability within the research group. It is also a commonly used epoxy in the electrical industry in combination with (conventional sized) silicon dioxide filler.

2.3.2. Filler materials

A list of filler materials used can be found in Table 2.1, electrical properties are compiled in Table 3.4 on page 54. Aluminum oxide (Al_2O_3) particles were chosen because they are commonly used in both the scientific community and industry. Therefore a large amount of measurement data exists for comparison. Al_2O_3 was thus chosen to have a proof-of-concept to build on. This was necessary since there was no previous knowledge about synthesis of nanocomposites in our group. It is surprising how few universities did have the know-how for creating nanodielectrics themselves. Usually samples are provided by a handful of industry partners, which safeguard their knowledge well.

Magnesium oxide (MgO) was chosen as filler material because it has shown to reduce the amount of space charge [62]. Aluminum nitride (AlN)

and boron nitride (BN) on the other hand have been chosen because of their high thermal conductivity.

Silicon dioxide (SiO₂) was provided in the form of Nanopox[®] from the company Nanoresins in Hamburg, Germany. As conventional sized filler this material is widely used in cast resin transformers.

2.3.3. Coupling Agent

One major problem with the synthesis of NC is the dispersion of the nanoparticles. The dispersion of nanoparticles in the host material is of vital importance for nanodielectrics to unleash their full potential. If the particles are not dispersed the agglomerations of NP act like particles of larger size. This would nullify the beneficial effects of nanoparticles. As mentioned in section 1.1.5, particles smaller than 80 nm tend to agglomerate and form larger chunks of particles. The intermolecular forces keep nanoparticles together. To achieve an even dispersion of nanoparticles in a host material it is helpful to modify the particle surfaces. This surface modification – also called surface functionalization – serves two purposes:

1. Keeping the nanoparticles dispersed, hinder reagglomeration.
2. Provide bond between host and filler material.

A silane coupling agent (SCA) in the form of 3-(2,3-epoxypropoxy)propyl-trimethoxysilane (EPPS) was chosen for surface modification (chemical structure see Figure 2.3). EPPS consists of an organofunctional group, a linker, a silicon atom and hydrolyzable groups. The organofunctional group is an epoxy group, which can bond to the host material we use, while the hydrolyzable group can bond to hydroxyl groups on the surface of our nanoparticles.

2.4. Preparation procedure

The following procedure has been applied for creating nanocomposites with Al₂O₃, MgO, AlN and BN particles. It is applicable for all particles with

Table 2.1.: List of filler material used, properties derived from TEM and XRD measurement.

Filler type	Average Size in nm ^a	Structure	Shape
Al ₂ O ₃	25	crystalline	spherical
Al ₂ O ₃ conv.	4000	crystalline	irregular
AlN	60	crystalline	spherical, hexagonal, cubic
BN	20	amorph	spherical, truncated cubes ^b
BN	70	hexagonal crystalline	spherical
BN	500	hexagonal crystalline	platelets
BN	1500	hexagonal crystalline	spherical
BN	5000	hexagonal crystalline	spherical
MgO	22	crystalline	spherical, egg, truncated cubes
SiO ₂ ^c	20	crystalline	spherical

^aAverage size has been determined with TEM and SEM with the exception of particles with more than 100nm average diameter. In this case the information about the size has been obtained from the respective datasheet.

^bB₂O₃-shell, see text.

^cSiO₂ was used in form of Nanopox[®], provided by the company NanoresinsTM, Germany, and is the only particle type that we did not introduce into the host material ourselves.

2.4. Preparation procedure

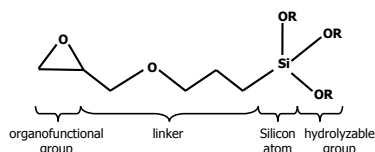


Figure 2.3.: Chemical structure of 3-(2,3-epoxypropoxy)propyltrimethoxysilane (EPPS).

hydroxyl-groups on the respective surfaces. The procedure consists of the following stages:

- Dispersion of particles
- Surface functionalization
- Mixing of particles with host material
- Evaporation of the solvent
- Casting
- Curing

2.4.1. Particle preparation

The particles are first dispersed in ethanol (C_2H_6O) by means of ultrasonification. The ultrasonic bath helps reducing the surface energy of the particles. Formic acid is added to set the pH value in order to reach a higher zeta potential. The ζ potential is a measure for the stability of a colloidal system, with the isoelectric point at a ζ potential of 0 mV being the least stable. A detailed description can be found in Appendix D. With a ζ potential between +25 and -25 mV and utilizing ultrasonication the nanoparticles disperse very well in ethanol. Due to laser diffraction (see Appendix A.2 on page 129) we know that after 90 minutes virtually all agglomerates are broken up.

2.4. Preparation procedure

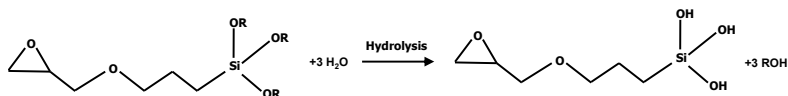


Figure 2.4.: Hydrolysis, reaction of EPPS with H₂O to form free OH-groups for bonding with the nanoparticles.

2.4.2. Surface functionalization

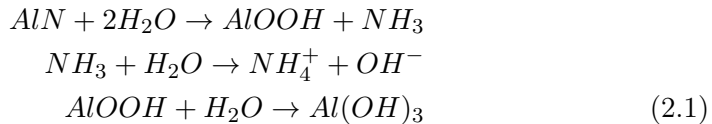
Surface functionalization introduces chemical functional groups to a surface and is done with EPPS (see page 18). The EPPS molecule, with a common formula of $R(CH_2)_nSiX_3$, serves two functions. R represents a nonhydrolysable organic radical, in our case an epoxide. On the other end is the alkoxy group X, which can bond to mineral surfaces.

The reaction of the alkoxy groups of the EPPS with H₂O is called hydrolysis. This is done in order to have free groups for bonding with the hydroxyl-groups (OH-groups) at the particle surface is illustrated in Figure 2.4. The condensation of the silanol groups with the OH-groups on the NP surface or neighbouring hydrolysed EPPS molecules is the subsequent step.

Vital for the functionalization process is the availability of free OH-groups on the particle surface. In case of oxides like Al₂O₃ or MgO the presence of OH groups on the surface is easy to predict. Alumina for example consists not only of an Al₂O₃-core. Oxidation causes the formation of an aluminum oxide hydroxide-layer ($AlO(OH)$) around each particle. For our nitrides we had to find proof for the presence of OH-groups on the surface.

The reactivity of AlN powders with water has been reported by Bowen et al. [63]. A thin aluminum hydroxide shell forms on the surface of the AlN core at room temperature. When AlN nanoparticles are hydrolyzed, an amorphous layer composed of $AlO(OH)$ is initially formed on the surface of the AlN particles, which then transforms to $Al(OH)_3$ according to reactions 2.1.

2.4. Preparation procedure



The presence of a boron oxide (B_2O_3) layer on the surface of BN particles was validated by X-ray diffraction. Therefore we can conclude that the modification of BN can be successful as well, since EPPS reacts with the B_2O_3 -layer covering the BN particles and creates covalent bonds.

One crucial question is how to calculate the exact amount of EPPS needed for particle treatment? Since many improvements in terms of dielectric behaviour are attributed to the quality of the interface, it is desirable to have a strong interface [64]. If we don't add enough EPPS this could lead to weaker interfaces, because of missing surface groups the polymer can connect to. The excess of EPPS on the other hand leads to homoreaction of the SCA molecules and to the formation of a gel. A too high concentration of this gel in the insulation material can deteriorate the electrical and mechanical properties of the nanocomposite. Therefore it is important to find the minimal amount of EPPS needed to ensure a sufficient surface modification.

$$m = \frac{4 \cdot \pi \cdot r^2 \cdot l \cdot \rho_{EPPS}}{\frac{4}{3} \cdot \pi \cdot r^3 \cdot \rho_f} = \frac{3 \cdot l \cdot \rho_{EPPS}}{r \cdot \rho_f} (\%) \tag{2.2}$$

The approximate amount of EPPS for spherical particles can be calculated as in Equation 2.2, where r is the average diameter of nanoparticles, l is the thickness of the SCA layer (see Figure 2.5), while ρ_{EPPS} and ρ_f are the density of the SCA and the filler material respectively. This is only an estimation, since we do not know the exact thickness of the EPPS layer. For our experiments we assumed a thickness of 1 nm for l . Confirmation comes from experimental data, see Appendix A.3.

The second method to approximate the amount of SCA needed is via the number of hydroxyl groups on the particle surfaces, since EPPS reacts with those groups. First it is needed to find out how many hydroxyl groups are in 1 gram of the filler material. This can be done via thermogravimetric

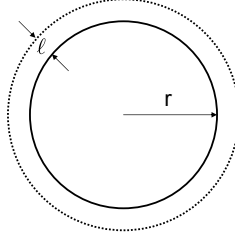


Figure 2.5.: Schematic of one nanoparticle and the EPPS layer grafted on it.

analysis (TGA) under nitrogen atmosphere. The covalent bonds between the mineral and hydroxyl groups are breaking up at temperatures ranging between 720 and 870 K. The mass of e.g. Al_2O_3 particles is decreased by 0.312 % in this temperature range. This leads to the conclusion that 1 gram of Al_2O_3 particles contain 3.12 mg of hydroxyl groups. The number of molecules can be calculated using Equation 2.3, where N_A is the Avogadro number and v the number of mol. The number of mol can be found simply with the ratio of the mass of the material to its molar mass (Equation 2.4). Equation 2.4 can be rewritten as Equation 2.5. For the example with Al_2O_3 we can calculate the number of OH molecules in 1 gram of nanopowder then according to Equation 2.6.

$$N = N_A \cdot v \quad (2.3)$$

$$v = \frac{m}{M} \quad (2.4)$$

$$N = N_A \cdot \frac{m}{M} \quad (2.5)$$

$$N = 6.02 \cdot 10^{23} \cdot \frac{3.12 \cdot 10^{-3}}{17} = 1.104 \cdot 10^{20} \quad (2.6)$$

$$m = v \cdot M = \frac{N}{N_A} \cdot M = \frac{40 \cdot 10^{-18}}{6.02 \cdot 10^{23}} \cdot 128 = 0.0085g \quad (2.7)$$

The density of hydroxyl groups per square nanometer can be found using the surface area of nanoparticles. The effective surface area of Al_2O_3

nanoparticles from Sigma Aldrich is $40 \text{ m}^2 \cdot \text{g}^{-1}$. In $40 \cdot 10^{18} \text{ nm}^2$ are $1.104 \cdot 10^{20}$ molecules, thus in 1 nm^2 2.76 molecules. This means that 1 square nanometer of particle surface contains approximately 3 hydroxyl groups. The minimum number of EPPS molecules that can attach to the surface is 1 because the EPPS has 3 hydrolyzable groups per molecule. Therefore $40 \cdot 10^{18}$ molecules are needed to modify 1 gram of Al_2O_3 . Since the molar mass of EPPS is $128 \text{ g} \cdot \text{mol}^{-1}$, the mass can be calculated using (2.7). The obtained value should be multiplied by a factor of 5¹, since we assume that not all EPPS molecules bond with all 3 hydroxyl groups. According to these calculations the amount of EPPS needed for functionalizing nanoscale Al_2O_3 equals 3% of the weight of the nanoparticles used. Main parameters for calculating the amount of EPPS needed are the surface area of the nanoparticles and the weight loss of TGA under nitrogen atmosphere between 720 and 870 K.

2.4.3. Mixing

The next step is the high shear mixing of the solution consisting of surface functionalized particles and the solvent with the epoxy. After the mixing process with typically 5000 rpm for 15 minutes, the solvent has to be removed. Ethanol has a boiling point of 351.55 K at 1 atm. To ensure quick evaporation, the solution is put into a vacuum oven (pressure <200 mBar) at 363 K. Under these pressure conditions the boiling point of ethanol is below 313 K. The evaporation process still takes between 1 and 4 days, depending on the amount of solvent in the solution. During this process the solution has to be mixed manually at regular intervals to prevent sedimentation. It is very important that the solvent is completely removed before curing. As soon as the curing agent is added, the polymerization starts and the chain-growth would trap the remaining ethanol molecules in the polymer matrix. This would lead to phase separation, thus cracks and a very brittle material.

After evaporation of the solvent, the quantitative appropriate amount of curing agent was added to the solution. The resulting mixture was stirred

¹This is an empiric value that has been obtained at Delft ChemTech.

for another 10-15 minutes with a high shear mixer. The high shear mixer helps to disperse particles which might cluster together.

2.4.4. Casting and Curing

To ensure the absence of voids, the final mixture has to be degassed. Finally the epoxy can be poured into the molds and cured at e.g. 413 K for at least 3 hours for a system based on CY231 with HY925. The samples were post-cured at 413 K for typically 14 hours.

2.4.5. Validation of the particle dispersion

One of the major problems in creating nanocomposites is obtaining an even distribution of particles in the host material. The main questions in this stage of the research were:

- How good is the dispersion of nanoparticles in the solution before adding the SCA?
- Is the surface functionalization successful?
- Do we have an even distribution of nanoparticles in the epoxy matrix?
- Is the distribution of particles even throughout the sample or do we observe sedimentation?

Size distribution and the influence of the dispersion method

Objective was to determine the best method for dispersing our nanoparticles. Previous attempts in making samples with nanoscale alumina raised the question of how good the dispersion is before introducing the particles into the epoxy resin.

Analyzing the size distribution by means of laser diffraction (see Appendix A.2) shows that water is the best solvent for our nanoscale Al_2O_3 . However, due to the difficulties of evaporating water from the composite later on, it is not the best candidate for our preparation method. Ethanol

is better due to its lower boiling point, but without appropriate mixing methods most particles cluster and form agglomerates of approximately 15 μm . High shear mixer, ultrasonic probe and ultraturrax proved to be inefficient methods for dispersing the particles. With the ultrasonic probe we also observed a drastic temperature increase of the the solution. This prevented long mixing times, because the polymer started to boil. The experiments showed that the best method for dispersing the particles is the use of an ultrasonic bath for sufficient time. After 60 minutes only 10% of the particles and agglomerates of particles still have an average size larger than 600 nm. They could be separated from the rest of the suspension. Another 30 minutes later almost all agglomerates were broken up.

The Al_2O_3 -ethanol-suspension has been shown to be stable as well: after 5 days the results were identical with the fresh samples. Apparently the particles are not re-agglomerating once they are dispersed in the solvent.

Determining the success of the surface functionalization

With laser diffraction it was not possible to determine if the silane treatment was successful, since there were no visible changes between treated and untreated Al_2O_3 . EPPS is very small compared to Al_2O_3 -particles, thus the additional layer on the particle surfaces is not visible due to measurement accuracy. Successful treatment could be indicated with TGA measurements however, as shown in Appendix A.3.

Particle dispersion within the epoxy matrix

The particle dispersion in epoxy was validated with both scanning electron microscopy (SEM, see Appedix A.4.2) and transmission electron microscopy (TEM, see Appendix A.4.1). In Figure 2.6 an Al_2O_3 -epoxy composite with a fillgrade of 2wt.% can be seen. It shows that small clusters of particles are evenly dispersed throughout the material. Given that the dispersion is the same in all three dimensions, we can assume from the TEM results that samples with 2wt.% Al_2O_3 have good dispersion of nanoparticles.

Figure 2.7 shows the dispersion of Al_2O_3 for 5wt.%. There are some

2.4. Preparation procedure

larger agglomerates, compared to 2wt.%. The overall distribution of particles is good however, since most particles and agglomerates are below 100 nm. For more details about specimen characterization, see the corresponding Appendix A, starting on page 127.

To discern if problems with sedimentation might arise, a particle concentration profile was created. This was done by thermogravimetric analysis of top, middle and bottom parts of a cylindrical sample. For details see Appendix A.3.2. The analysis showed no signs of sedimentation in the bottom of the sample. We noticed an even distribution of particles along the vertical axis of the sample instead.

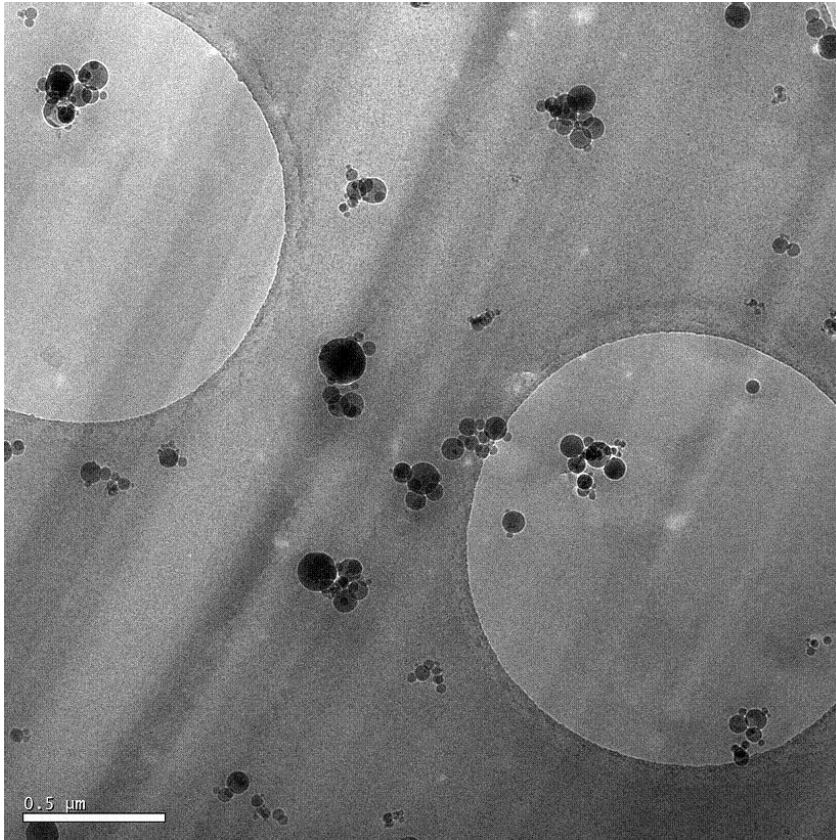


Figure 2.6.: TEM micrograph of 2 wt.% Al₂O₃ particles in an epoxy film. The bright circles larger than 1 μm are part of the sample holder in the background.

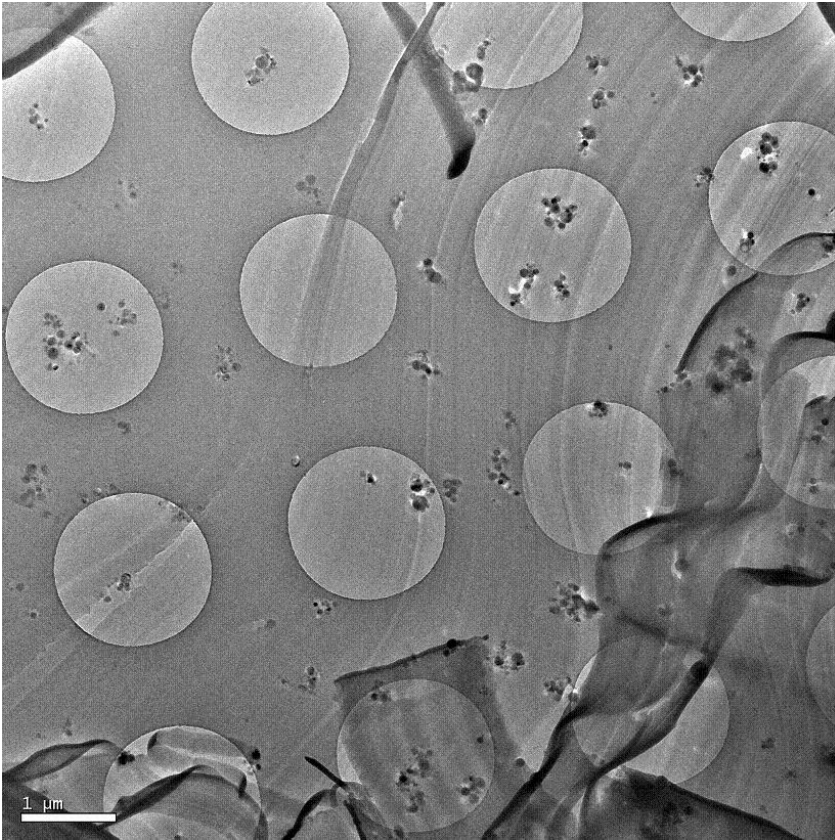


Figure 2.7.: TEM micrograph of 5 wt.% Al₂O₃ particles in an epoxy film. The bright circles larger than 1 μm are part of the sample holder.

CHAPTER 3

THEORY AND MODELLING

True ignorance is not the absence of knowledge, but the refusal to acquire it.

-Karl Popper

Initial results regarding polymer-based nanocomposites were astounding, since they defied conventional wisdom. Until recently the tendency was to assume, that the host material does not change due to the introduction of fillers. It turns out that the presence of the filler material does change the host itself however. According to this paradigm shift old ideas to model dielectrics have to be reconsidered and new models devised to explain nanocomposites.

This chapter contains the theoretical background concerning nanodielectrics, as well as models that help understanding them. It starts with a description of the interactions, bonds and forces at a molecular level, which are fundamental for understanding nanocomposites. Then four models for the description of nanocomposites are presented, which are prominent in literature: the electric double layer, the intensity model, the multi-core model and the interphase volume model. The lion's share of Chapter 3 is

3.1. Conventional Theory – Limitations when dealing with Nanocomposites

the introduction of the polymer chain alignment model (PCAM), starting on page 40. This model shares ideas with the multi-core and interphase volume models and explains the dielectric behaviour of nanodielectrics bottom-up, starting at the molecular level.

3.1. Conventional Theory – Limitations when dealing with Nanocomposites

Conventional theories in electrical engineering deal with bulk materials and macroscopic phenomena. A lot of rules in electrical engineering are empiric and don't apply for nanomaterials. Examples of this are rules of mixture for calculating the permittivity of a composite insulator. There are two main groups of theoretical approaches to the problem of composite permittivities: effective medium (or mean field) theory and integral methods [65]. The former group utilizes average fields or polarizabilities and induced dipole moments, the latter uses low concentration formulae and integrate them to higher concentration. Factors taken into account by conventional mixture rules are volume percentage of the filler, inhomogeneities, particle shape, orientation and distribution as in e.g. [66]. According to conventional mixture rules for composites the permittivity of the compound should lie between the permittivity of the filler and the matrix material. Nanoscale fillers don't necessarily show this behaviour however.

Factors that are not taken into account by laws of mixture are particle size, surface treatment or structural changes in the material due to the introduction of the filler material. It has been shown how much permittivity values can differ due to variations of particle size or surface treatment [67].

3.2. Topology of Nanocomposites

This section describes the most important interactions within the complex systems we call nanocomposites (NC). These can mostly be found between relatively few molecules, where we don't have the large numbers of participating molecules found in a macroscopic material, which would even out

individual molecules' behaviour.

3.2.1. Intramolecular interactions

Within polymer chains covalent bonds are dominant. In this case two atoms share electrons to complete their valence shell. If one atom has covalent bonds with more than one other atom, interactions between these bonds occur. Due to these interactions bonds can only arrange in certain angles, e.g. 109° in case of carbon chains [68]. Interactions can also occur between neighbouring polymer chains, but they are usually not as strong as covalent bonds. Intramolecular interactions within filler particles play no major role in NC.

3.2.2. Intermolecular interactions

Intermolecular interactions are important for polymer based NC, despite their relatively small energies. A list of bonding distances and energy of common bonds in polymers is compiled in Table 3.1. They can be divided in the following categories:

- Coulomb forces
- Polarization forces
- Hydrogen bonds
- Covalent bonds

Coulomb forces

These are purely electrostatic interactions between charges, permanent dipoles etc. Coulomb forces are considered weak intermolecular forces, even though the forces between two ions can surpass those of stonger forces like hydrogen bonds. Attraction is stronger for larger charges and smaller distance between the charges. Permittivity of the surrounding media is also important. Coulomb forces have a larger range than hydrogen or covalent bonds.

Table 3.1.: Common bonds in polymers, their bonding distance and energy [69].

bonding partners	bond distance in nm	energy in kJ/mol
C-C (aliphatic)	0.154	350
C-C (aromatic)	0.140	560
C=C	0.135	610
C-H	0.109	413
C-O	0.143	351
C=O	0.122	708
C-N	0.147	293
C-Cl	0.177	339
C-F	0.131	485
N-H	0.102	389
Si-O	0.164	444
dipole-dipole	0.5-0.8	2-12
hydrogen bond	0.5-0.8	3-25
dispersion forces	0.5-0.8	0,3-4

Polarization forces

Forces between dipoles in atoms and molecules as a result of an applied electric field are called polarization forces. It does not matter if the dipole is permanent or induced. Even uncharged molecules can have an electric dipole, e.g. H₂O or HCl. When a non polar molecule is forming a dipole after applying an electric field it is called induced dipole. In molecules with covalent bonds a permanent dipole comes into being by asymmetric displacement of common electron pairs. The dipoles of some molecules also depend on the surrounding media and change drastically when being introduced to a different medium.

Hydrogen bonds

An electrostatic bond of a hydrogen atom with an electronegative atom like oxygen, nitrogen or fluoride is called hydrogen bond. The atoms do not share electrons however, which distinguishes hydrogen bonds from covalent bonds to hydrogen (below). In order to enable a hydrogen bond, the respective hydrogen atom has to be covalently bonded to another (electronegative) atom to create the bond. These bonds can occur both inter-

and intramolecularly.

Covalent bonds

Covalent bonds are considered strong chemical bonds and are characterized by atoms that are sharing electrons, or between atoms and other covalent bonds. They can be exploited for achieving certain material properties. Polymer chains are crosslinked by creating covalent bonds between individual polymer chains. Changes in the mechanical properties are directly related to the degree of crosslinking¹ [70], while there is no clear indication for electrical properties yet [71]. Polymer chains and nanoparticles can also form covalent bonds, which might have a similar effect as crosslinking has on the material properties.

3.3. Theories for describing Nanocomposites

Various models and theoretical constructs for describing NC have been introduced in recent years. What all the models have in common is their emphasis on the interface between nanoparticle and host material. Some important models are described here.

3.3.1. Electric double layer

According to Helmholtz an electric double layer forms between a solid and a liquid phase (see Figure 3.1). For this model one phase has to be mobile. Unlike in crystalline structures the chains that make up a polymer can move slightly. Therefore we can assume the polymer to be mobile in NC for an approximation. The electric double layer is utilized in the multi-core model, where the electric double layer is superimposed over the particles. The double layer consists of the:

Stern layer the inner region where ions are strongly bound and the

Outer layer a diffuse region where ions have a higher mobility.

¹Degree of crosslinking: amount of covalent bonds between polymer chains

When a particle is moving the ions within the boundaries of this double layer travel with the particle. Any ions beyond the boundary do not move with the particle. This border is called slipping plane. The electric potential across the outer layer, between the slipping plane and the surrounding medium, is called ζ potential (for details see Appendix D).

The double layer can form in a NC when surface groups of a particle get ionized or adsorbed. At the interface between particle and host material a electric double layer is formed. The charges inside the particle are either trapped charges, mobile electrons or holes. The formed Stern layer around the particle consists of dipoles or adsorbed ions of opposite polarity. Presumably this Stern layer is of molecular thickness and very high density. The Stern potential (Figure 3.1) has the same polarity as the Stern layer and is defined by ions which are attracted by the surface potential of the particle. The outer layer or diffuse Gouy-Chapman layer is the last layer which lies between the Stern layer and the unaffected host material. Size and strength of the outer layer are inversely proportional to the conductivity of the host material.

3.3.2. Intensity model

The intensity model by Lewis is based on the idea that the intensity I_α of a material property α does not change abruptly [72]. Instead it changes gradually, over the course of several nm, the interface, as illustrated in Figure 3.2. Each atom and molecule in the interfacial area will be interacting with its surroundings via a combination of both short- and long-range forces [73]. The intensity α can be any physical or chemical property. In the simplest situation it might be a concentration of a constituent of a system, e.g. a molecular, atomic or ionic species or an electron concentration. Specific examples are the free electron concentration at a hot metal surface in vacuum (Figure 3.3(a)), the oxygen concentration at the surface of silicon (Figure 3.3(b)) or the normal electric field at a metal-n-type semiconductor contact (Figure 3.3(c)). As can be seen from those examples, I_α doesn't necessarily stay between the values of material A and B, but can reach intensities above or below both values.

This model does not offer a description about physical processes hap-

3.3. Theories for describing Nanocomposites

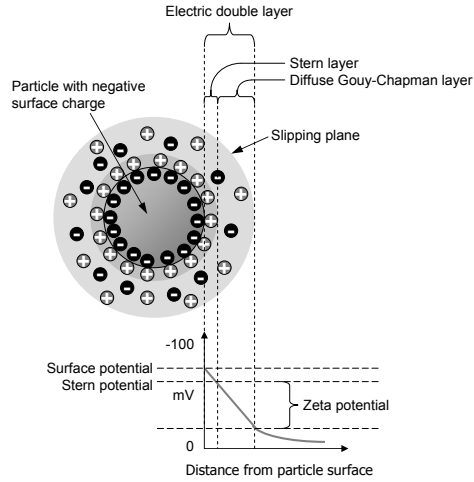


Figure 3.1.: Illustration of surface potential, Stern potential, ζ potential and the electrical double layer around a particle.

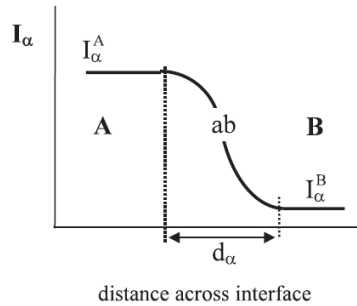


Figure 3.2.: The interface ab between two phases A and B defined by the intensity I_α of a chosen property α as it changes in passage across it [73].

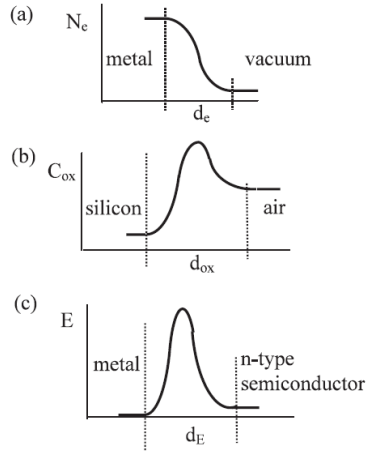


Figure 3.3.: Interfacial intensities: electron concentration at a metal vacuum interface (a), oxygen concentration at silicon-air boundary (b) and electric field at metal-n-type semiconductor interface (c) [73].

pening at the interfacial area and remains nondescript and very general. However, it serves as visualisation of the impact of nanoscale fillers on macroscopic material.

3.3.3. Multi-core model

The multi-core model is a rather complex and flexible theoretical construct, first proposed by Tanaka in 2005 [74]. It describes the interactions of a spherical inorganic particle with the surrounding media by means of three layers [64] as illustrated in Figure 3.4.

Bonded (first) layer consists of molecules that are physically bound to the particle surface by coupling agents like EPPS. This layer is presumably only 1 nm thick and formed by covalent, van der Waals or hydrogen bonds.

Bound (second) layer consists of polymer chains that have strong bonds

3.3. Theories for describing Nanocomposites

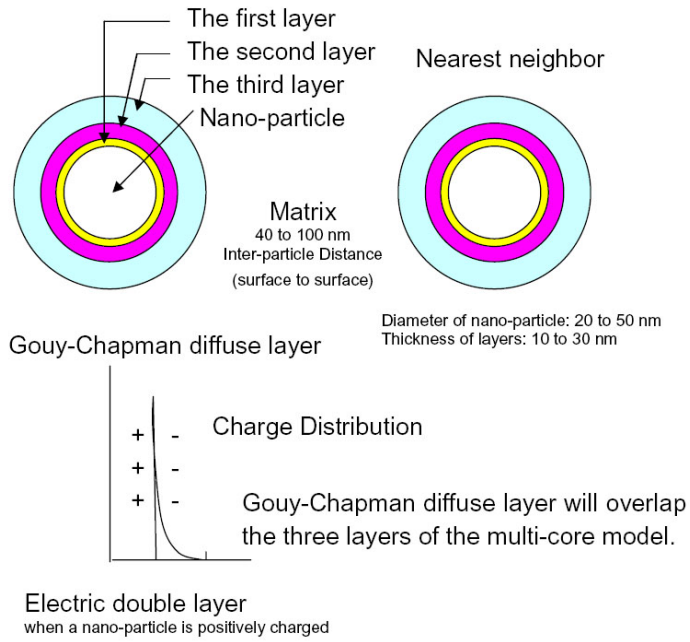


Figure 3.4.: Illustration of the multi-core model [64].

and interactions with the first layer. Due to the strong interactions the structure of the polymer is changed in this region, because chains or parts of chains are aligning perpendicular to the particle surface. Therefore this layer influences the chain mobility which can reflect in an increased glass transition temperature. The thickness of this layer is assumed to be between 2 and 9 nm.

Loose (third) layer is interacting with the bound layer and consists of polymer chains that see morphological changes due to the filler material. These changes can materialize in changes of chain formation, chain mobility, free volume or crystallinity. This layer can be several tens of nm thick.

The model is too vague to predict changes of macroscopic properties due to nanofiller but is a good base for explaining the phenomena in NC. This model does not conflict with the electric double layer. The electric double layer can be thought of overlapping with the multi core model rather than replacing it.

3.3.4. Interphase Volume Model

The Interphase Volume Model by Rätzke tries to correlate the interfacial region with the increased resistance of NC to electrical treeing, partial discharges and HV-arcing [76, 77]. It assumes that spherical particles of uniform average diameter d are dispersed homogenously within the polymer structure. To estimate the volume fraction of the interfacial regions, dubbed interphase, a mathematical model based on a body-centered crystal lattice unit cell was devised. With this and an assumption of the thickness of the interfacial zone of e.g. $i = 10$ nm, the interphase volume can be calculated as shown in Figure 3.5. It shows that there are certain maximum values for the volume fraction of the interphase, depending on the volume fraction and size of the filler material.

This model illustrates very well the influence of the particle size on the NC. Also it makes clear why we can witness a saturation effect in NC, i.e. why an increase of filler loadings above 10 wt.% doesn't significantly

3.3. Theories for describing Nanocomposites

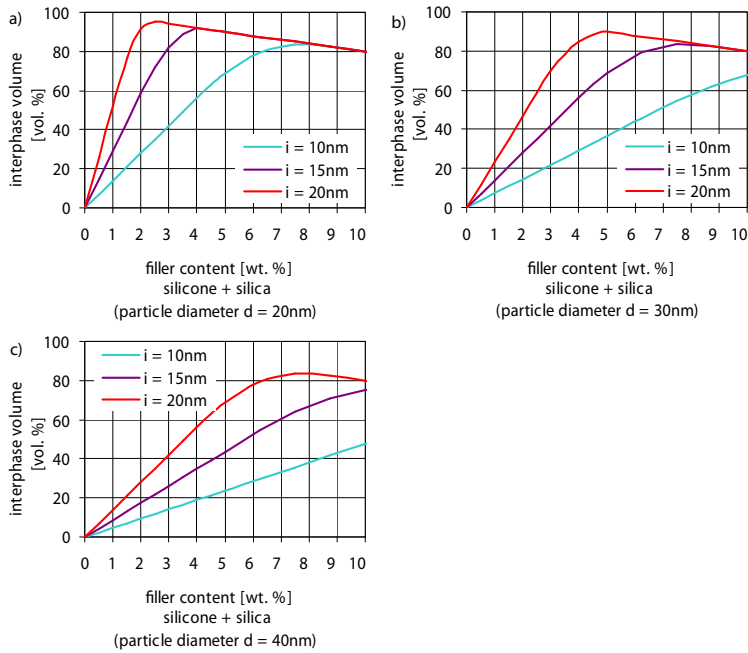


Figure 3.5.: Interphase content according to the Interphase Volume Model for silicone rubber with SiO_2 nanoparticles and interphase thickness i for average diameter d of (a) 20 nm, (b) 30 nm and (c) 40 nm [75].

improve certain properties anymore. An in-depth description about the interfacial region, like in the multi-core model, is missing.

3.4. Polymer Chain Alignment Model

It has already been firmly suggested that the surface area, thus interfaces between host material and filler particle, have a profound effect on the intrinsic and functional properties of a NC. The model presented hereafter assumes, that surface functionalized nanoparticles can lead to an alignment of polymer chains. This chain alignment in combination with the filler material leads to a restructuring of the host polymer. The model is labelled polymer chain alignment model (PCAM). Aim of the PCAM is to describe the morphology of NC and consequently derive the impact of parameters like average particle diameter and fillgrade on the bulk properties.

3.4.1. Philosophy (PCAM in a nutshell)

The idea behind this model is, that the material properties of NC strongly depend on processes prior to and during polymerization. From experiments with the surface functionalization (see page 19) we can assume that – under ideal conditions – one EPPS molecule can connect with the particle surface during hydrolysis per square nm, as illustrated in Figure 3.6. As long as no curing agent is involved, the epoxy-groups of the EPPS can't react with anything in the proximity of the particle. The intermolecular forces between the molecules will result in a parallel alignment of the EPPS molecules, because the molecules try to stay apart from each other as much as possible. That means that one polymer chain per square nm could connect with each particle during polymerisation.

During the mixing process of surface modified particles and epoxy host, bisphenol-A chains will surround the particles but not react as long as no curing agent is added. When the anhydrite is added, the curing agent attacks the epoxide groups, leading to polymerisation of the polymer chains and the EPPS on the particle surfaces [68]. In an ideal case, one bisphenol-A chain will react with one EPPS each. These chains will then align

3.4. Polymer Chain Alignment Model

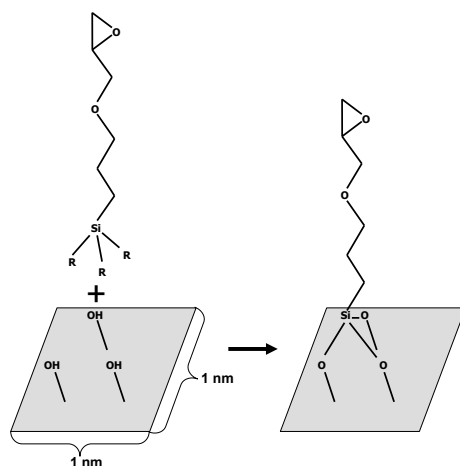


Figure 3.6.: Illustration of the reaction of a particle surface area of 1 nm^2 with a EPPS molecule.

perpendicular to the particle surfaces, due to the intermolecular forces between the chains, analogous to the forces that acted between the EPPS molecules prior to polymerisation. In between the polymer chains a interpenetrating polymer network will form with physical properties unlike host or particle [78]. This is illustrated in Figure 3.7, where (a) represents the mineral surface, (b) the covalently bonded interface and (c) the polymer network altered by the surface modification [79].

A non-modified particle has only low interaction with the host material (Figure 3.8(a)). Compared to that, a particle with surface modification would see a restructuring of the surrounding host material. As shown in Figure 3.8(b), a layer of chains aligned perpendicular to the particle surface could form. Since polymers often consist of long chains, the area surrounding these aligned zones would also be affected.

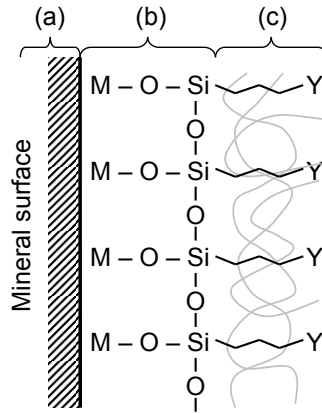


Figure 3.7.: Illustration of the interpenetrating polymer network at the interface between particle and host, with (a) being the mineral surface, (b) the covalently bonded interface and (c) the polymer network altered by the surface modification.

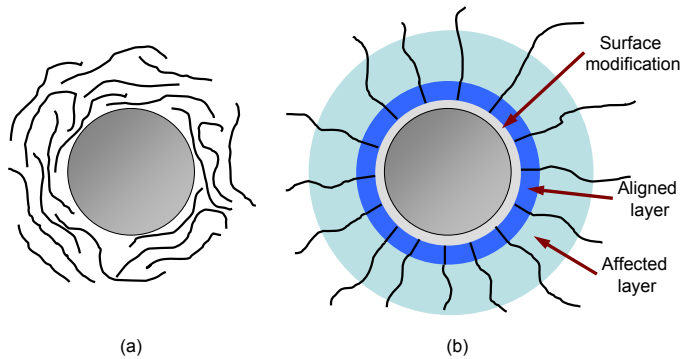


Figure 3.8.: (a) Particle without surface modification and thus only weak interaction with the host; (b) Particle with layer of surface modification, resulting layer of aligned polymer chains, further affecting the surrounding area thus restructuring the polymer.

3.4.2. Assumptions and Definitions for this model

In the following, the PCAM tries to explain the influence of nanoscale filler material on a polymeric host material. To simplify the mathematics behind the model, some assumptions are made regarding the structure of the material:

- All particles are spherical
- All particles have the same diameter d
- The particle distribution within the polymer matrix is homogeneous
- The particles are covered by a uniform SCA layer, which allows 1 polymer chain to bond to the particle per 1 nm^2
- Polymer chains bond to the particle and align according to intermolecular forces, leading to a rigid inner layer (aligned layer) with a thickness t_i
- Another layer is organizing between the well organized inner layer around each particle, and the unaffected host material, the affected outer layer with the thickness t_o

3.4.3. Morphology of NC

An ideal distribution of nanoparticles in a NC does materialise, when no clusters of particles can be found. In an ideal composite all particles would stay as far away as possible from each other. With this homogeneous distribution of particles within the polymer host, the particles can be thought of as being arranged similar to atoms in a crystal structure [76]. Analogous to crystallography we can therefore design a unit cell for polymer NC. The unit cell is in our case a box of nanometric dimensions, containing information about the

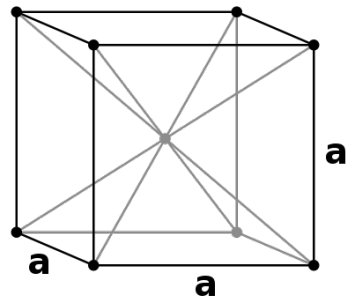


Figure 3.9.: Body-centered cubic unit cell.

3.4. Polymer Chain Alignment Model

spatial arrangement of nanoparticles and the particle density. These unit cells can be stacked in three dimensional space, describing the arrangement of particles in the bulk material. A body-centered cubic (BCC) unit cell (Figure 3.9) can be used to approximate a material with an ideal distribution of NP. In this cell one particle is located on each corner and one in the center. The length of the cell a depends on the fillgrade per volume p and the filler size d . Equation 3.2 can be used to calculate a , results are compiled in Table 3.2. Equation 3.3, which expresses the interparticle distance b , can be derived via the space diagonal of the unit cell (Figure 3.10). This represents the average distance of a particle to the nearest neighbouring particle.

$$p = \frac{V_{Particles}}{V_{BCC}} = \frac{\frac{\pi}{6} \cdot d^3 \left(1 + 8 \cdot \frac{1}{8}\right)}{a^3} = \frac{\pi \cdot d^3}{3 \cdot a^3} \quad (3.1)$$

$$a = d \cdot \sqrt[3]{\frac{\pi}{3 \cdot p}} \quad (3.2)$$

$$b = \frac{\sqrt{3}}{2} \cdot a - d \quad (3.3)$$

The interparticle distance was quantified experimentally by measuring graphs obtained via TEM. Each micrograph was divided in sections and the average distance between NP and clusters of NP was calculated. The best agreement could be found for NC with SiO₂ nanofiller. Model and measurement differ by 20 nm, which is 28%. For Al₂O₃-ER and AlN-ER the differences between calculated values and experimental results is larger than 40% (90 nm). This is due to a wider particle size distribution and more agglomerations, compared to SiO₂-ER. Differences become even larger for specimen with 5 wt.%, due to an increased amount of agglomerations in the respective specimens. NC with SiO₂ showed the best dispersion of NP in terms of both average particle size and interparticle distance. Interparticle distance between the investigated sections of SiO₂-ER NC differed by a maximum of 30%. In other NC variations of the interparticle distance of up to 100% could be found. Since the micrographs

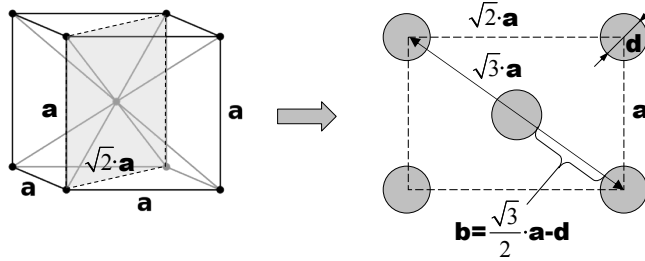


Figure 3.10.: Illustration of the interparticle distance b , body and space diagonal of a body-centered cubic unit cell.

are two dimensional, while the model estimates for a three dimensional environment, the values for model and measurement differ. The interparticle distance b of the cell projected on a 2D plane can be approximated according to Equation 3.4. This enables to calculate a correction factor according to Equation 3.5, which is about 30%. Taking the correction factor into account, the differences between measurement and model for samples with 2 wt.% are negligible in case of SiO_2 . However, for samples with 5 wt.% the difference is even larger, since the interparticle difference measured was already larger than calculated. The exception is SiO_2 with 5 wt.%, which shows very good agreement with the model.

$$b_{2D} \approx \sqrt{2} \cdot a - d \quad (3.4)$$

$$\frac{b_{2D} - b}{b} = \frac{a \cdot \left(\sqrt{2} - \frac{\sqrt{3}}{2} \right)}{\frac{\sqrt{3}}{2} \cdot a - d} \approx \frac{1}{3} \quad (3.5)$$

3.4.4. Layer Volume Calculation

For an estimation of the volume of the interface layers, the nature of the interface has to be identified first. Figure 3.7 on page 42 illustrates the ideal case for an interface. It consists of approximately one EPPS molecule

3.4. Polymer Chain Alignment Model

Table 3.2.: Theoretical length a of a BCC unit cell for different NC and average distance between particles b .

Type	Fillgrade in wt.%	a in nm	b in nm
AlN	0.5	497	370
AlN	2	312	210
AlN	5	228	138
AlN	10	179	95
Al ₂ O ₃	0.5	221	167
Al ₂ O ₃	2	139	95
Al ₂ O ₃	5	102	63
Al ₂ O ₃	10	80	44
BN	0.5	169	126
BN	2	106	72
BN	5	78	47
BN	10	61	33
MgO	0.5	188	141
MgO	2	118	80
MgO	5	86	53
MgO	10	68	37
SiO ₂	0.5	154	113
SiO ₂	2	97	64
SiO ₂	5	71	41
SiO ₂	10	56	28

3.4. Polymer Chain Alignment Model

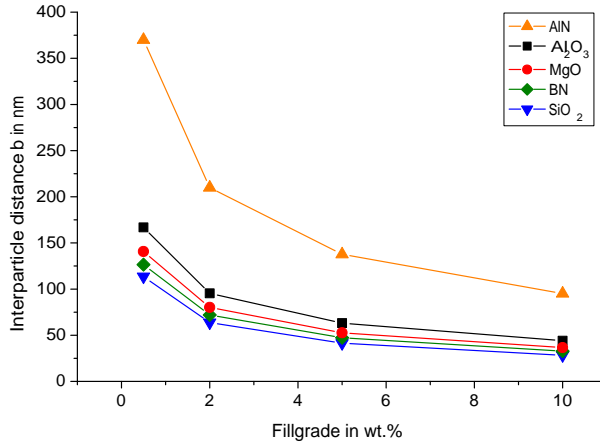


Figure 3.11.: Interparticle distance b as function of fillgrade in wt.% for different filler materials.

per nm^2 particle surface, which is connected to an epoxy chain. Since we use five times the mass of EPPS that would be needed for covering all particles with a homogeneous layer (see page 21), reactions between EPPS molecules on the surface are likely to occur. This leads to EPPS layers with a thickness in the range of \AA , up to some nm. Attached to the modified surface is the first layer of epoxy chains. Individual epoxy chains have lengths of some nm and can be up to 100 nm. The intermolecular forces lead to predominantly parallel alignment of chains close to the particle surface. This leads to crystalline structure around each particle. With increasing distance to the surface the material becomes less crystalline, as illustrated in Figure 3.12.

Aligned and affected layer volume

Volume for inner and outer layer can be calculated with Equations 3.6 and 3.7. Figure 3.13 shows the volume percentage of particles, inner layer, outer layer and unaffected polymer for a BCC unit cell. For calculations

3.4. Polymer Chain Alignment Model

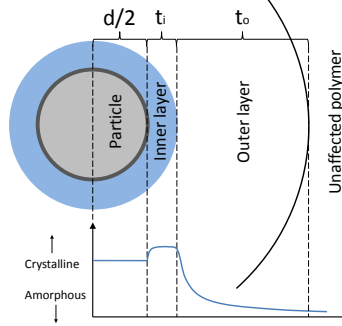


Figure 3.12.: Illustration how crystallinity can change from particle to surrounding polymer. The particle itself can be crystalline or amorphous.

values of 5 nm for the inner and 10 nm for the outer layers are defined. The thickness of the inner and outer layers is determined by the structure of the host material, the particle surface and the surface functionalization of the particles. It was defined with 5 nm, since this is the approximate length of a bisphenol-A molecule, as shown on page 14.

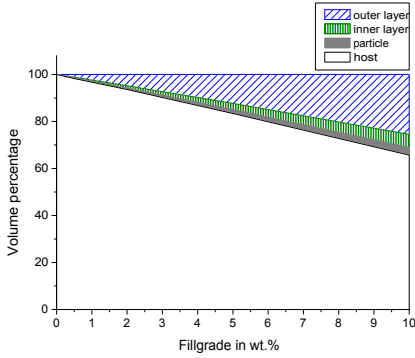
The two main characteristics of particles, that determine the layer volume are the average particle diameter d and the volume percentage of the filler p . The latter is correlated with the fillgrade in weight via the particle density. Both the particle diameter and fillgrade determine the length of a BCC unit cell a , and consequently the interparticle distance b (Equations 3.2 and 3.3).

$$V_i = \frac{8 \cdot \pi}{3} \left[\left(\frac{d}{2} + t_i \right)^3 - \left(\frac{d}{2} \right)^3 \right] \quad (3.6)$$

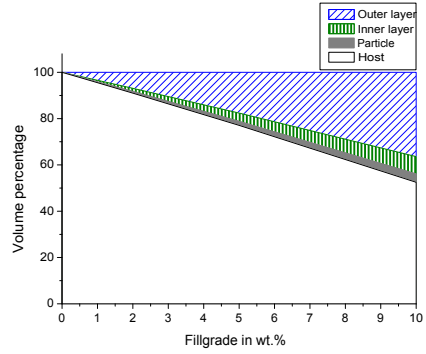
$$V_o = \frac{8 \cdot \pi}{3} \left[\left(\frac{d}{2} + t_i + t_o \right)^3 - \left(\frac{d}{2} + t_i \right)^3 \right] \quad (3.7)$$

It can be seen in Figure 3.13, that the volume percentage of inner and outer layer increases in a linear fashion for fillgrades up to 10% per weight. AlN particles, which have the largest average diameter d , show the smallest

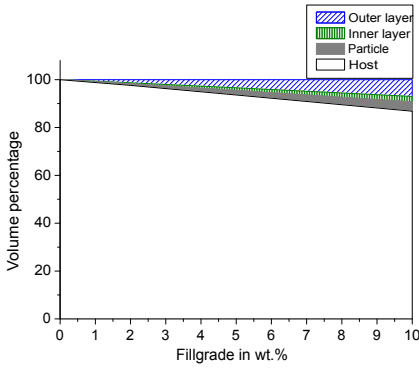
3.4. Polymer Chain Alignment Model



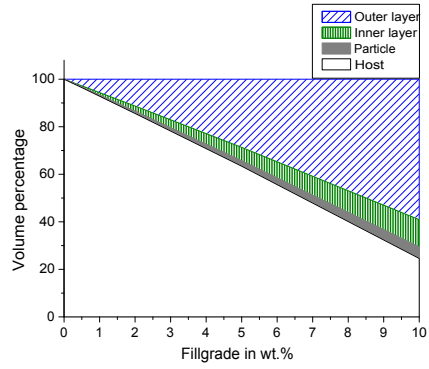
(a) Al_2O_3 particles.



(b) MgO particles.



(c) AlN particles.



(d) SiO_2 particles.

Figure 3.13.: Volume percentages of host material, particles, aligned and affected layers for one BCC unit cell, calculated for various nanoparticles: Al_2O_3 3.13(a), MgO 3.13(b), AlN 3.13(c) and SiO_2 3.13(d). For this calculation a thickness of the aligned inner layer t_i of 5 nm was chosen, while the thickness of the outer layer t_o is 10 nm.

interface volume percentage (Figure 3.13(c)). Figure 3.13(d) shows SiO₂, which has the same d as MgO, but a larger interface layer volume (Figure 3.13(b)). This is due to the lower density of SiO₂, which in turn leads to a higher p per volume for the same fillgrade per weight. In case of SiO₂ NP we also see an end of the linear increase at 9% by weight. At this point the affected layers start to overlap.

Layer interference

For higher fillgrades and a sufficiently small interparticle distance b , the layers will start overlapping. Overlapping of the outer layers of neighbouring particles will occur if condition 3.8 is fulfilled. As soon as condition 3.9 is fulfilled, inner layers will overlap as well. Overlapping of the inner layers only occurs at a very high particle density. In order to fulfill condition 3.9, a fillgrade of more than 35% by weight is necessary for SiO₂ NP. For NP with higher density, the fillgrade to achieve the same effect is higher. The average diameter d of SiO₂ would have to be smaller than 8 nm, to fulfill condition 3.9 for a fillgrade of 10% by weight.

$$b < 2 \cdot (t_i + t_o) \quad (3.8)$$

$$b < 2 \cdot t_i \quad (3.9)$$

3.4.5. Effects of Chain Alignment

It has been demonstrated, that even small amounts of NP with a sufficiently small average diameter d ($d \leq 25$ nm) lead to a significant change in the material structure. The beneficial effects do not scale with the filler content, as has been shown experimentally in e.g. [53, 80], or Chapter 4 on page 59. Hence it is not desirable to restructure too much of the volume of the base polymer.

The restructuring of the aligned layer is linked with an increased crystallinity. Crystalline areas of polymers have strong anisotropic behaviour due to intra- and intermolecular forces [81]. Effects of crystallinity in polymers include changes to both electrical and thermal conductivity. From

HDPE it is known, that an increase of the crystallinity leads to a decreased AC breakdown strength [82].

Crystalline regions of polymers tend to have a higher resistivity than amorphous regions. Hence conduction predominantly occurs in amorphous regions of the polymer [83]. In neat ER conduction is electronic, since holes and electrons can travel along and between the chains. The introduction of NP to the polymer matrix can change the conduction paths. It has been proposed that conductive particles in polymers can actively contribute to the conduction [57]. As illustrated in Figure 3.14, electrons can approach the particle between the chains, while holes can travel along them. Considering an electron flow from the left to the right, electrons should pass effortlessly into empty electron states of the particle. This would charge the particles negatively, consequently attracting positive holes. Holes can move along the chains from the right to the left, which in turn would result in an electron-hole recombination focused on the particle.

Figure 3.15 illustrates the recombination from the viewpoint of the band theory. Polymers that are common in HV engineering are assumed to have negative electron affinity, particles act as quantum wells [57]. An external voltage provides the energy needed for the electron to tunnel from the polymer to the particle. This charges the particle negatively, subsequently the particle attracts positive holes. The holes can also tunnel into the particle, where they can recombine with the electrons present. The band gap (see Table 3.3) determines how much energy is needed for recombination. A band gap in nanoparticles is in general smaller than in an insulating polymer, hence particles will become recombination centres. As indicated in Figure 3.15, the energy distance between the conduction bands of polymer and particle gives the energy needed for an electron to tunnel into the particle. The band gap of the particle defines the amount of energy needed for recombination and the distance between the valence bands indicates the amount of energy a hole needs to tunnel into the particle.

As mentioned earlier, not only electrical properties are affected. Phonon scattering is suppressed in crystalline bisphenol-A ER structures, which leads to an increase in the thermal conductivity [87].

An increase of NP fillgrade or reduction of NP size, hence an increase of nanometric crystalline regions, also increases the amount of boundaries

3.4. Polymer Chain Alignment Model

Table 3.3.: Band gaps and vacuum levels of particles from literature [84, 85, 86].

Type	Band gap in eV	Vacuum level in eV
AlN	6.3	?
Al ₂ O ₃	9.5	?
BN	5.2	?
MgO	7.8	0.8
SiO ₂	1.1 ··· 8.9	?
TiO ₂	3.2	4

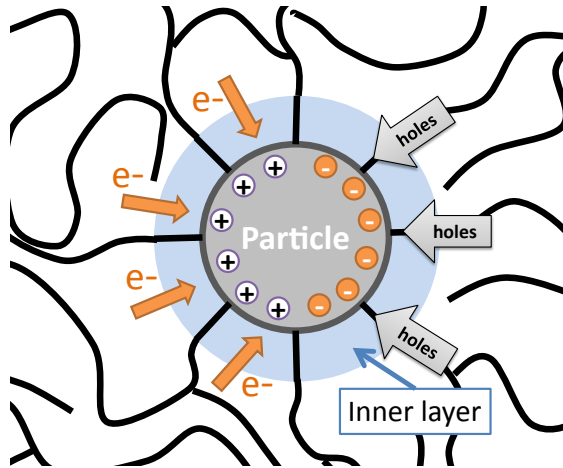


Figure 3.14.: Illustration how nanoparticles can contribute to conduction.

between crystalline and amorphous regions within the material. However, it is unclear how these boundaries alter bulk properties in polymer NC.

3.4.6. Influence of the Material

Structural changes

As hinted on page 47, the combination of filler and host material determines the aligned and affected layers, thus the structure of the material. The particle size and amount of hydroxyl groups available on the surface

3.4. Polymer Chain Alignment Model

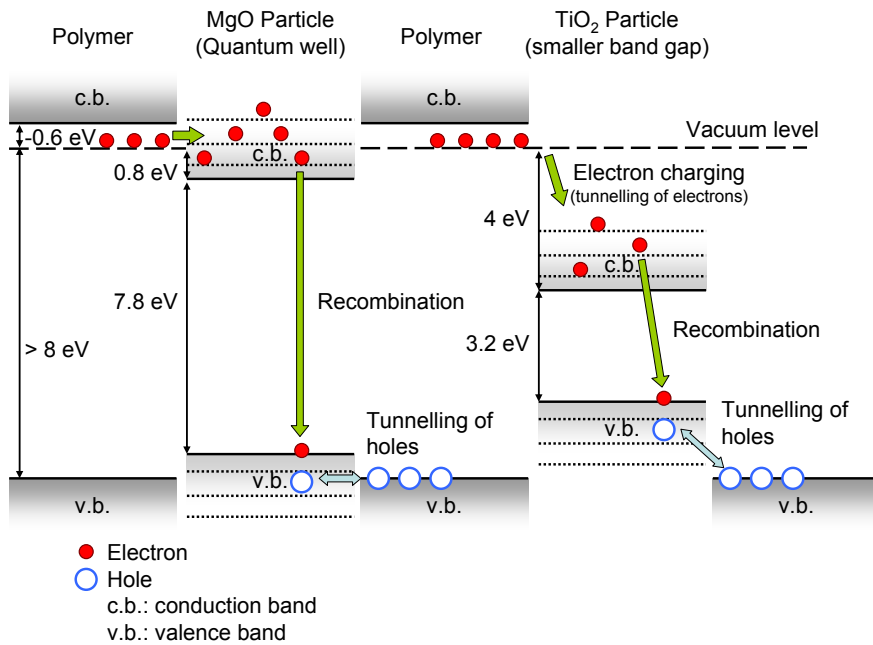


Figure 3.15.: Illustration how nanoparticles can contribute to conduction shown at two different particles: on the left MgO with bandgap of 7.8 eV and TiO₂ on the right with 3.2 eV bandgap and larger distance to the vacuum level.

3.4. Polymer Chain Alignment Model

Table 3.4.: Electrical properties of particles from literature.

Type	Vol. resist. in $\frac{\Omega}{m}$	Rel. permittivity	AC BD strength in $\frac{kV}{mm}$
AlN	$> 10^{14}$	9 at 1 MHz	17
Al ₂ O ₃	$> 10^{14}$	9.8 at 1 MHz	16.9
h-BN	$10^8 - 10^{13}$	4 at 8.8 GHz	35
MgO	$> 10^{17}$	5 at 1 MHz	10
SiO ₂ (fused)	$> 10^{10}$	3.82 at 1 MHz	40

determine how many polymer chains can react with the particle provided there is adequate surface modification. The length of the aligned layer depends on the molecular composition of the polymer host. Bisphenol-A molecules, as shown in Figure 2.2 on page 14, have an approximate length of 4 to 5 nm. The first layer of bisphenol-A molecules is the most uniform. Beyond the distance t_i , which equals the length of one molecule, the intermolecular forces that hold the molecules of the first layer in place decrease. Crosslinking will occur as well, which in combination with the decreased intermolecular forces results in a decrease of crystallinity over distance (Figure 3.12).

Changes due to material properties

The dielectric properties of the filler material have a clear impact on the bulk properties, despite the low filler content. Dielectric properties of the particles used are compiled in Table 3.4. The permittivity of the filler material affects the permittivity of NC, as shown in Chapter 5 on page 71. However, the influence of the aligned layer is more dominant for the dimension of the bulk permittivity of NC. The low permittivity layers can significantly decrease the relative permittivity of the material. The quality of dispersion, hence the quality of the NC, is determined by the solubility of the filler material. The ζ -potential gives a good indication of how difficult it is to disperse the particles. A lower ζ potential reflects in more successful dispersion with the same methods.

3.4.7. Influence on the dielectric properties of the bulk material

Short term breakdown strength

Several factors have an impact on the short term breakdown strength. We noticed a decrease with increasing fillgrade for our ER with conventional filler. For example the AC breakdown strength of an unfilled epoxy system CY231 with anhydrite hardener is 32 kV/mm, while CY231 with 60 wt.% of microscale SiO₂ filler sees a reduction to 20 kV/mm [88]. The dielectric strength of the used fillers is often lower than the dielectric strength of unfilled epoxy (see Table 3.4). But even with fillers that have a high dielectric strength the breakdown strength can see a reduction, since the interfaces are a weak spot.

However, for the low fillgrades that are investigated in this thesis, this reduction should not be dominant. More dominant in case of NC are agglomerations. Agglomerations of surface functionalized NP don't act simply like a microparticle, due to the polymeric layers in between. Instead the particles with the overlapping silane and polymer layers result in irregular areas for permittivity and conductivity. As illustrated in Figure 3.16, these agglomerates can in turn lead to a field enhancement. This field enhancement adds up to the applied field strength, subsequently leading to an earlier breakdown compared to NC with an even particle dispersion.

Resistance to electrical treeing and partial discharges

Due to the strong bonding between surface modified NP and polymer host, a lot of energy is needed to break the bond in order for the tree to grow. The length by which an electrical tree grows is in the range of μm [89, 56]. The interparticle distance b on the other hand is much smaller in NC (Table 3.2). Hence an electrical tree is forced to interact with NP and the respective aligned polymer layer, while expanding in a NC with well dispersed nanoparticles. The tree gets deflected by the particle, as illustrated in Figure 3.17, and loses more energy as it would in the unaffected polymer with larger, unmodified particles. Resistance to partial discharges of NC also benefits from the high energy needed to

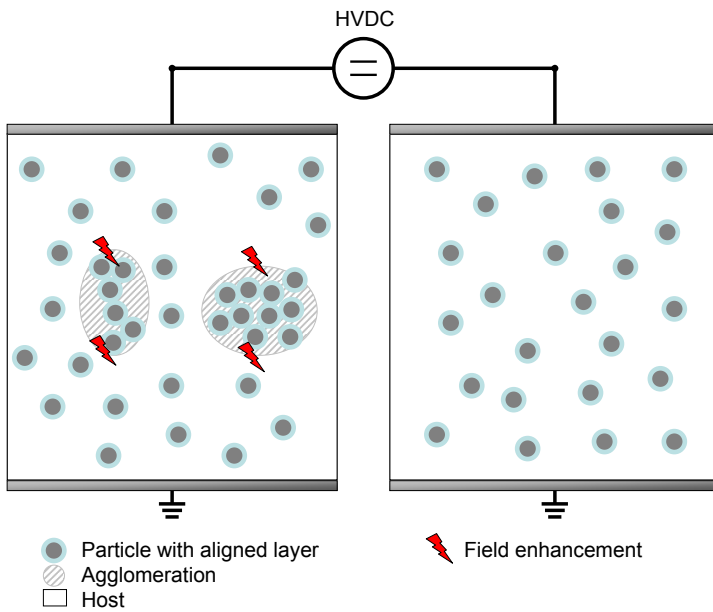


Figure 3.16.: Illustration how agglomerations of nanoparticles can lead to field enhancements, compared to a NC without agglomerations.

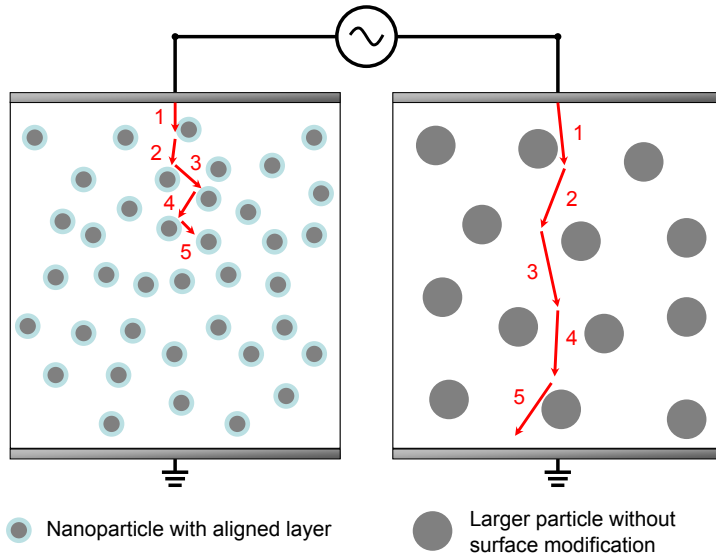


Figure 3.17.: Illustration how nanoparticles can hinder electrical treeing, compared to larger particles.

break the covalent bonds of the aligned layer.

Permittivity

The aligned layer around each particle has a very low real part of the complex permittivity ϵ' , due to its rigid structure. Affected layers will also show lower ϵ' , but not to the same extent. Consequently the ϵ' of the bulk of the host material sees a reduction, because of the volume of aligned and affected layers in the NC. However, as the fillgrade increases, the permittivity of the filler material will start to overshadow the permittivity decrease due to the aligned layers. Hence there will be a minimum value for ϵ' as function of fillgrade, after which the bulk permittivity will increase as a result of the ϵ' of the filler material. Experiments with surface modified

and non-modified microscale Al_2O_3 particles showed higher ε' values for modified particles, attributed to the better connection (thus interaction) of host and filler material (Figure 5.4(b) on page 76). This suggests that the rate at which the ε' increases after it's minimum is dependent on the permittivity of the filler material. However, if the ε' of the filler is lower than the host material we would see a different behaviour. In this case the ε' of the composite would remain lower than the host material and converge with the ε' value of the filler.

Space Charges

The space charge behaviour in NC depends on the particle distribution and filler material. With an even distribution of surface modified NP, the NP act as recombination centres according to Figure 3.14. It is likely that certain filler materials are more efficient recombination centres than others. However, agglomerations of NP will act as charge traps. The polymer layers between the agglomerated particles act as bottleneck for the electron transport, which takes place mainly between polymer chains. In case of large agglomerations additional interfacial polarization, thus charge accumulation, will occur as well.

Limitations of the PCAM

The PCAM does not take particles into account, which have a different aspect ratio than spherical particles. Various types of nanoclay – which usually have the shape of platelets – or carbon nanotubes and similar needle-like structures might show different behaviour.

The model is not limited to epoxy resin however. Any combination of a polymer host material and particles with compatibilizing surface treatment should behave in a similar fashion.

CHAPTER 4

BREAKDOWN STRENGTH

The most exciting phrase to hear in science, the one that heralds the most discoveries, is not "Eureka!" but "That's funny..."

-Isaac Asimov

The dielectric breakdown (BD) strength is one of the dominant factors for high voltage design. An evaluation of the viability of NC as high voltage insulation has to include an assertion of the BD strength. Within the scope of this work the impact of NP on the short term electrical breakdown strength was investigated threefold, as a function of:

1. Filler type
2. Fillgrade
3. Filler size

Electrode configuration and voltage form (impulse, AC or DC) have a profound effect on the measured BD strength [90]. Hence the BD strength should be accompanied by further information about the conditions under

4.1. Measurement Setup

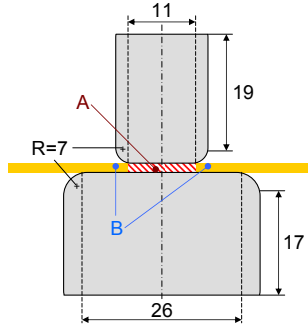


Figure 4.1.: Electrode configuration for BD tests.

which it was measured. Therefore this chapter also includes details about the measurement setup and testing conditions.

4.1. Measurement Setup

The dielectric breakdown strength (BD) was measured by means of a DC ramp test according to IEC 60243-1 and IEC 60243-2 [91, 92]. The electrode configuration can be seen in Figure 4.1. Dimensions were chosen such that the field strength is the largest in area *A*, while it stays at a minimum in areas *B*, in order to minimize the risk of flashover. Sample thickness was typically 0.6 mm. Sample and electrodes were immersed in oil to prevent flashover. The rate of voltage rise was chosen according to the aforementioned measurement standards: 500 V/s with negative polarity and a starting voltage of 10 kV. At least 5 samples from each sample batch were tested, typically 7.

4.2. Sample Preparation

The sample thickness is of considerable interest for BD tests. It has been shown that the BD strength of thin polymer films increases for decreasing sample thickness [93]. The increase is not linear but logarithmic, for a

sample thickness of less than 0.3 mm [94]. This means that when samples with a thickness of 0.3 mm are tested, a small variation in the sample thickness can already lead to strong scattering of the measurement results. The molds for casting and curing the samples were open topped, which led to variations of the sample thickness between batches of up to 0.1 mm. Therefore it was decided to use relatively thick samples of 0.6 mm for BD testing. Variations of 0.1 mm do not lead to significant changes of the BD strength for thick samples.

4.3. Analysis

The BD data were analyzed using a two-parameter Weibull function, which is commonly used for the analysis of insulation failure data, in batches of 7 samples on average. Equation 4.1 shows the cumulative distribution function with E being the BD field strength, F the cumulative failure probability, η and β the scale and shape parameters respectively. The scale parameter η represents the electric field strength for which the probability for a failure is 63.2%. The scale parameter β is analogous to the inverse of the standard deviation.

$$F(E) = 1 - e^{(-\frac{E}{\eta})^\beta} \quad (4.1)$$

The results are presented in form of a probability plot, where the x-axis shows the DC breakdown strength and the y-axis the unreliability. The unreliability gives information about the probability of failure for a given sample type at a certain DC field strength.

4.4. Filler Type

Table 4.1 shows BD data for four types of NC: Al₂O₃-ER, AlN-ER, MgO-ER and SiO₂-ER. Additionally CFC samples with EPPS modified Al₂O₃ filler were investigated. The NC are sorted by increase of η compared to the unfilled epoxy, which serves as reference. The scale parameter corresponds to the BD strength in kV/mm. Figure 4.2 illustrates results for NC with SiO₂ filler, which show the highest BD values measured. Al₂O₃-ER

NC had the second highest values (Figure 4.3). Figure 4.4 and 4.5 show values for AlN-ER and MgO-ER respectively, which have lower values than SiO₂-ER or Al₂O₃-ER, but in general higher than neat epoxy. The shape parameter β is relatively low for some composites ($\beta < 5$). No correlation could be found between β and fillgrade, filler type or dispersion. Impurities and cavities were found in some specimens. These can lead to premature BD, subsequently increasing the standard deviation for one set of measurements. Therefore the low β reflects inconsistencies during the early stages of our experiments with the synthesis, rather than material properties. This interpretation is supported by the consistency of β for MgO-ER NC, as seen in Table 4.2. These were the last samples that were produced, thus the manufacturing process was optimized and better controlled.

For subsequent analysis groups of samples were identified, which broke down because of impurities due to manufacturing, rather than the intrinsic BD strength. For Al₂O₃-ER with 0.5 wt.% two populations of samples can be identified. One that leads to a shape parameter, which is consistent with samples for 2 and 5 wt.%. The other population was discarded, which leads to a Weibull-distribution as shown in Figure 4.6. Similar adjustments have been done for AlN-ER (Figure 4.7) and SiO₂ (Figure 4.8).

The influence of the fillgrade is described in the subsequent section.

4.5. Fillgrade

Fig. 4.9 shows the distribution of BD values for NC as a function of fillgrade for 63.2% failure probability of the samples. This overview shows the highest short term DC BD values at fillgrades of 2wt.% or less for all samples. It can be seen that the BD strength is the highest for low filler content and decreases with increasing amount of filler for NC. The average BD values of all tested NC for all fillgrades are higher than the values of the reference samples. Due to problems with synthesizing AlN-ER with 5 % per weight these results are missing.

4.5. Fillgrade

Table 4.1.: Weibull parameters for DC ramp BD test on various specimen with 90% confidence bounds.

Filler	Fillgrade	η in kV/mm	lower b.	upper b.	η/η_0	β	lower	upper
SiO ₂	0.5 wt. %	297	283	310	182 %	15.3	8.8	26.7
Al ₂ O ₃	0.5 wt. %	252	214	297	155 %	3.8	2.3	6.4
AlN	2 wt. %	226	199	258	139 %	5.1	3	8.4
Al ₂ O ₃ (micro)	5 wt. %	221	207	235	136 %	12.3	6.8	22.3
MgO	0.5 wt. %	214	192	239	132 %	6.7	4.4	10.3
unfilled	-	163	153	173	100 %	10.2	6.6	15.8

4.5. Fillgrade

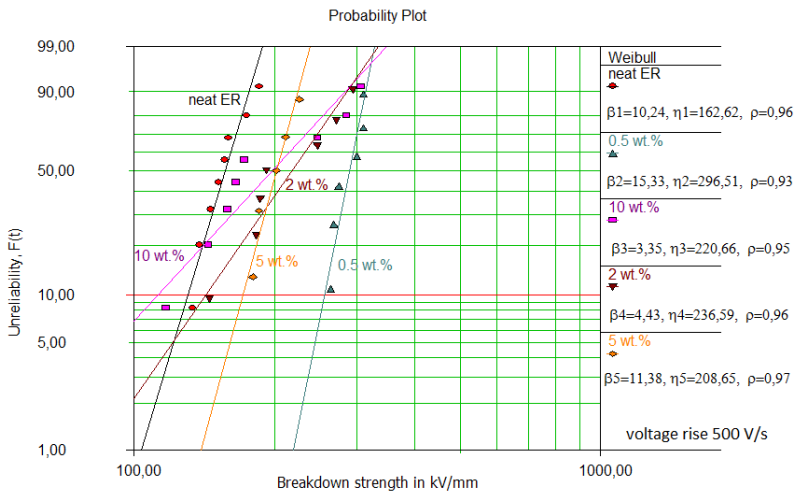


Figure 4.2.: Weibull plot for SiO₂-ER NC.

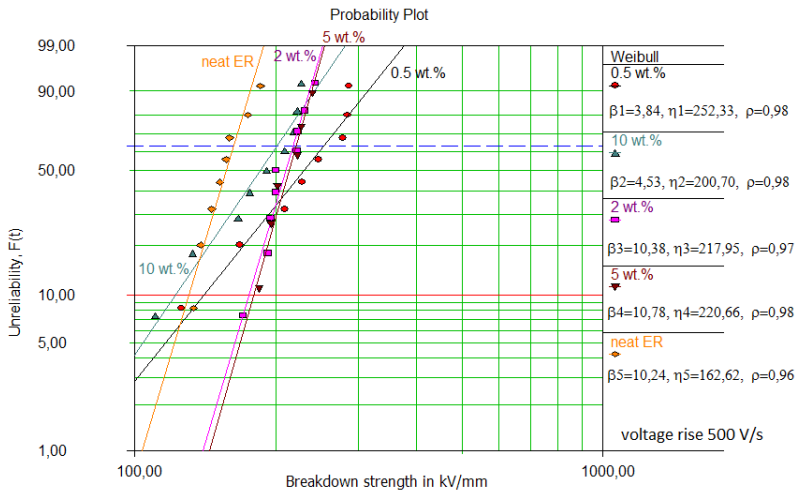


Figure 4.3.: Weibull plot for Al₂O₃-ER NC.

4.5. Fillgrade

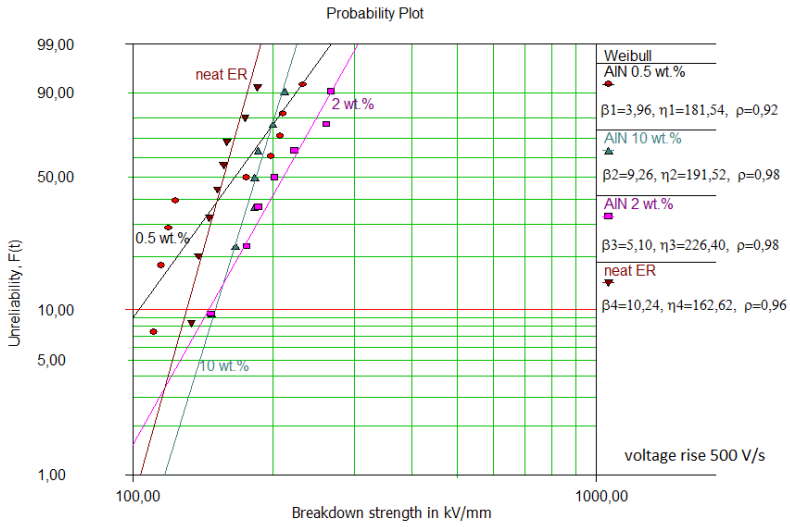


Figure 4.4.: Weibull plot for AlN-ER NC.

Table 4.2.: Scale and shape parameter for MgO-ER.

Filler	Fillgrade	η in kV/mm	β
MgO	0.5 wt.%	214	6.7
MgO	2 wt.%	168	6.4
MgO	5 wt.%	184	7.3

4.5. Fillgrade

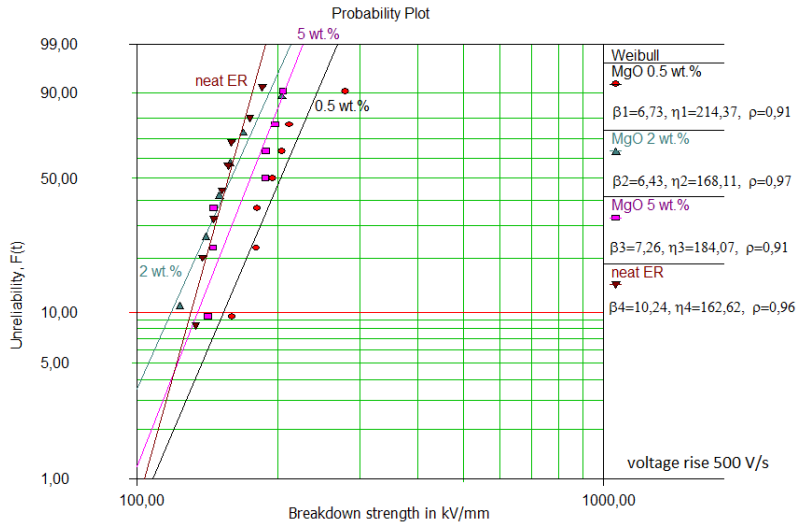


Figure 4.5.: Weibull plot for MgO-ER NC.

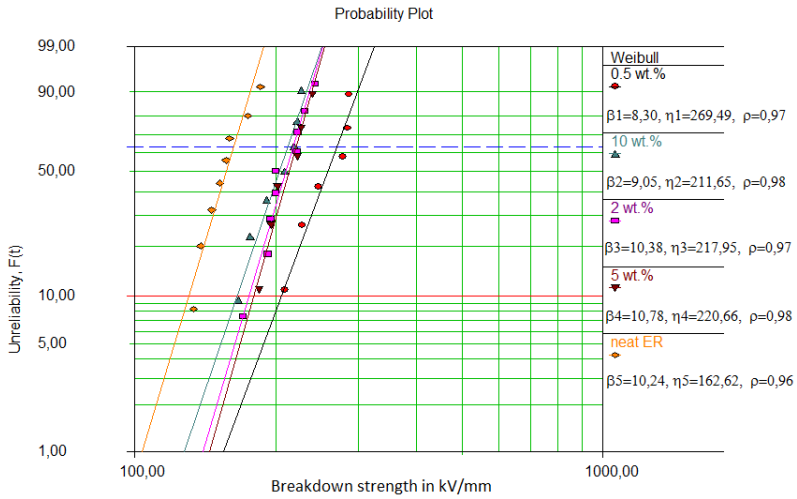


Figure 4.6.: Weibull plot for Al_2O_3 -ER NC with adjusted sample populations.

4.5. Fillgrade

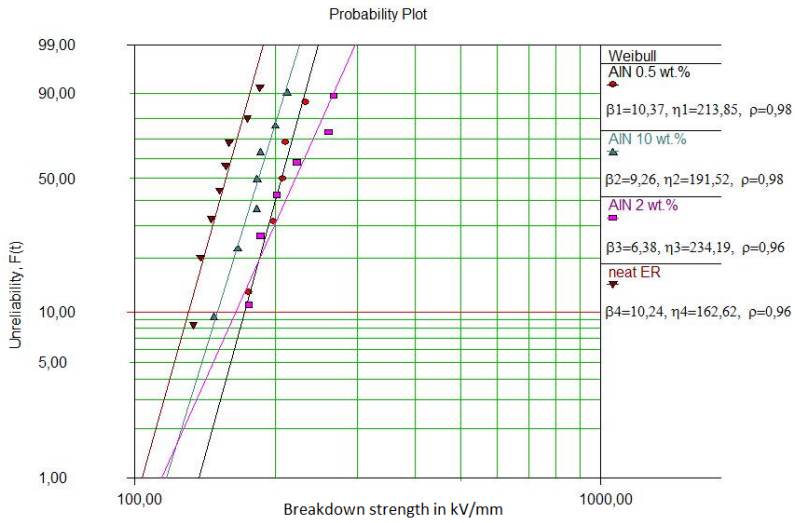


Figure 4.7.: Weibull plot for AIN-ER NC with adjusted sample populations.

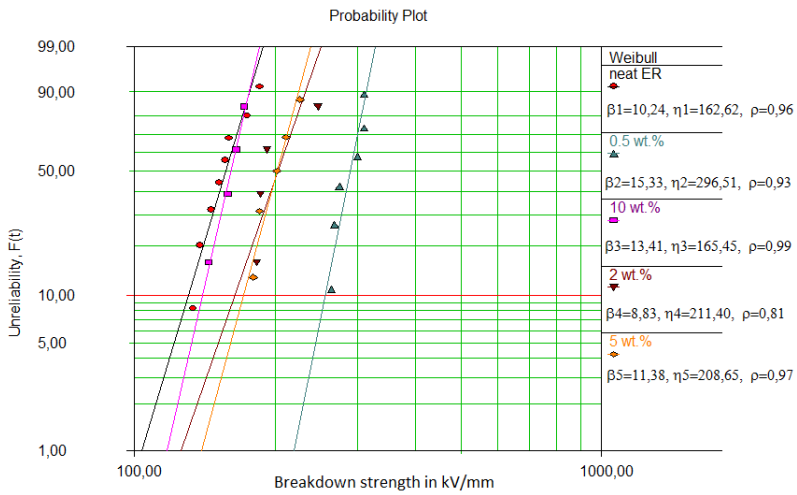


Figure 4.8.: Weibull plot for SiO₂-ER NC with adjusted sample populations.

4.6. Filler Size

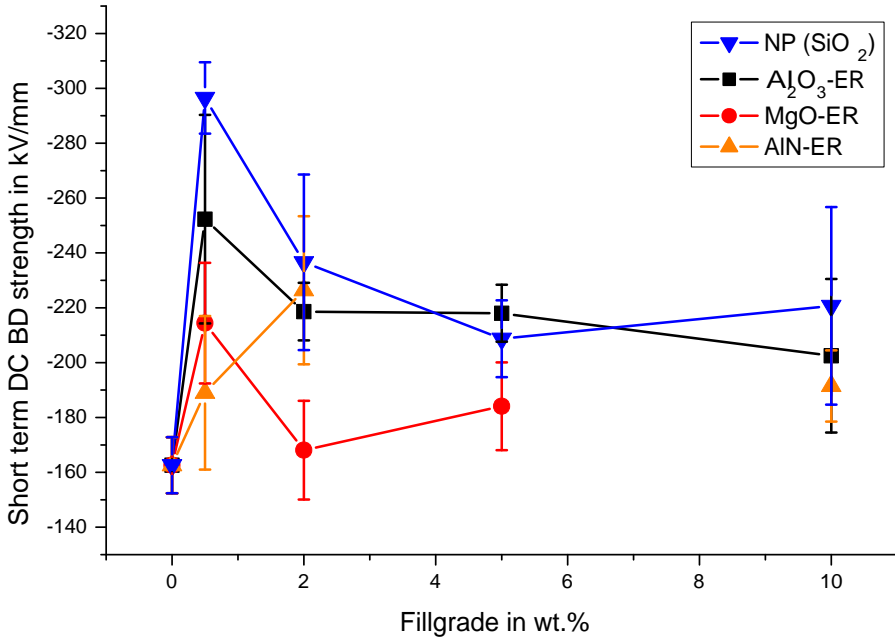


Figure 4.9.: Weibull scale parameter with confidence bounds for epoxy NC as function of fillgrade.

4.6. Filler Size

Figure 4.10 shows the distribution of short term DC BD values for BN-ER as a function of filler size. The horizontal line represents the unfilled base material. The Weibull scale parameters η in Table 4.3 show the voltage for 63.2% failure probability of the samples. The BD strength is the highest for a filler size of 70 nm. Here we observe an increase of the BD strength by more than 40% compared to the base resin. With increasing filler size the BD strength decreases, until it reaches a level of improvement, which is within the error margins of the measurement of the base resin, for samples with an average filler size of 5 μm .

It is apparent that the DC BD values follow a logarithmic relation.

4.6. Filler Size

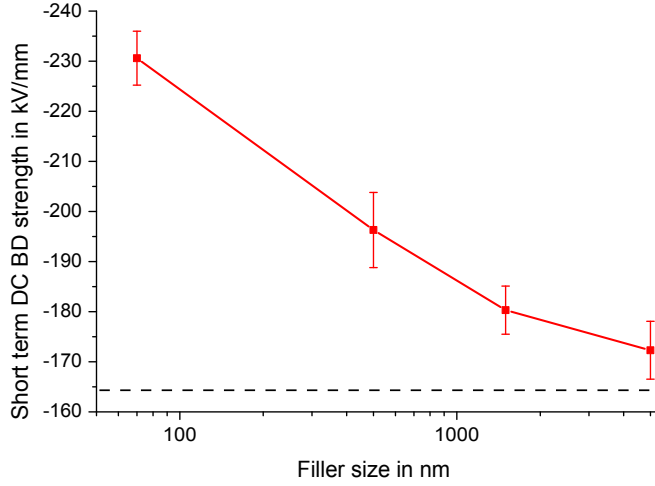


Figure 4.10.: Weibull scale parameter with confidence bounds for BN-epoxy samples with 10 wt.% as function of filler size.

Table 4.3.: Weibull parameters for DC ramp BD test on BN-ER specimen with 90% confidence bounds.

Filler	av. size	η in kV/mm	β	η/η_0
BN	70nm	231	5.4	141 %
BN	500nm	196	7.5	120 %
BN	1.5 μ m	180	4.8	110 %
BN	5 μ m	172	5.8	105 %
none	-	163	10.2	100 % (reference)

The increase of the BD strength is inversely proportional to the filler size. The effective total interface volume within the composites increases with decreasing filler size.

4.7. Summary

Two interesting observations dominate the DC breakdown behaviour of the investigated NC:

1. NC show the highest DC BD values for relatively low fillgrades
2. The DC BD values increase for decreasing average filler size

The DC BD characteristics seem inversely proportional to the fillgrade and filler size in polymeric NC, within certain limits. The highest DC BD values can be found at 2 and 0.5 wt.% for AlN-ER and the other NC respectively. Therefore it is reasonable to assume that the optimum filler content from a DC BD-perspective lies between these values, probably close to 0.5 wt.%, since fillgrades above 2 wt.% tend to lead to a deterioration of the BD strength. The shape parameter β is relatively low for some composites, but no correlation of β with the fillgrade, filler type or dispersion could be established. Variations of β therefore reflect impurities and cavities, that were found in some specimens, due to the unfamiliar production process.

From DS in Chapter 5 we will learn that that the presence of EPPS-modified nanoparticles leads to immobilization of layers around the particles, which can be interpreted as an increase of crystallinity within the material. This restructuring of the host material is an important factor for the changes in BD strength for nanofillers with low fillgrades (Chapter 3).

CHAPTER 5

DIELECTRIC RESPONSE

It's not that I'm so smart, it's just that I stay with problems longer.

-Albert Einstein

Dielectric spectroscopy (DS) is a powerful tool to investigate the dielectric response of insulating materials as a function of frequency. It is a technique which is sensitive to material changes on the molecular level, which is important for the investigation of NC. Similar to Chapter 4, this chapter will show the effect of nanoparticles on NCs. The complex permittivity of NC was evaluated as a function of frequency between 0.01 Hz and 10 MHz at different temperatures. The results have been evaluated in terms of influences of the filler material, namely:

1. Filler type
2. Fillgrade
3. Filler size

Temperature and humidity were controlled in the testing environment. Samples were dried and stored under nitrogen gas, while the measurement

setup allows to monitor the temperature with a sensitivity of 0.01 K.

5.1. Test setup

The measuring principle is based on the interaction of an external field with the electric dipole moments in the sample, which is often expressed by the complex permittivity ε^* (Equation 5.1) of the material.

$$\varepsilon^* = \varepsilon' - j\varepsilon'' \quad (5.1)$$

The real part of the complex permittivity is a measure of the amount of polarization. It is what we know as *relative permittivity*. The imaginary part is a measure of the losses involved in the polarization processes. The behaviour of the permittivity, as a function of frequency and temperature, is sensitive to material changes, caused by e.g. ageing processes. Modifications of the material due to the addition of different fillers can be investigated. The loss tangent $\tan(\delta)$ is directly related to the real and imaginary parts of the complex permittivity (Equation 5.2), where σ represents the conductivity.

$$\tan(\delta) = \frac{\omega\varepsilon'' + \sigma}{\omega\varepsilon'} \quad (5.2)$$

A voltage of variable frequency is applied to a sample and the magnitude and phase of the current flowing through the sample are measured. The equivalent circuit diagram is shown in Figure 5.1. More details about the DS setup and measurement can be found in Appendix B.1 on page 145.

5.2. Sample Preparation

Specimens were manufactured according to the synthesis exhibited in Chapter 2. They have typically been cured for 16 hours at 413 K and subsequently postcured at 413 K for 24 hours.

It has been shown by experiment that the ambient humidity can alter the results obtained from dielectric spectroscopy for both NC [95] and CFC/NMC [96]. To ensure that the tests are reproducible, it is therefore

5.3. Dielectric Response of Unfilled Epoxy

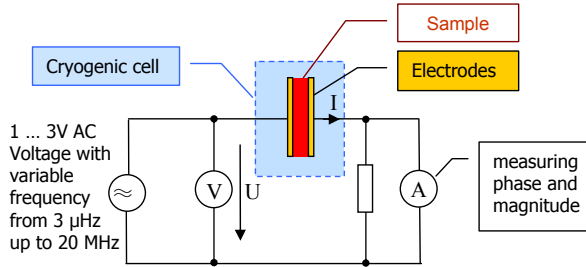


Figure 5.1.: Equivalent circuit diagram of the DS setup.

needed to keep humidity at a well defined level. For this purpose the samples were dried in an oven at 413 K for 48 hours. Afterwards they were stored in nitrogen gas (N_2) to keep them dry. The measurement itself was performed in a cryogenic cell under a nitrogen atmosphere.

It is important for the measurement accuracy that the sample thickness is not too large. The sample thickness for DS should be smaller than 1 mm and was typically 0.5 mm. Since the surfaces of both electrodes and samples are not perfectly even, it is recommended to metallize the specimen surfaces to improve measurement accuracy [97]. Al-electrodes have been applied on the specimen by means of physical vapor deposition. This Al film of less than $0.5 \mu\text{m}$ thickness ensures that the surface is on equal potential and well connected with the measurement setup.

5.3. Dielectric Response of Unfilled Epoxy

The dielectric spectrum of the unfilled epoxy is shown in Figures 5.2(a) and 5.2(b) as function of frequency, illustrating the real and imaginary part of the complex permittivity. It indicates a local maximum for frequencies below 10 Hz around 393 K, which we attribute to an α -relaxation process at the glass transition temperature. We also see a local maximum in ϵ'' , that moves to higher frequencies with increasing temperature. It can be seen at 1 kHz for 253 K and 100 kHz for 293 C. We attribute this peak

5.4. Impact of curing time and particle modification

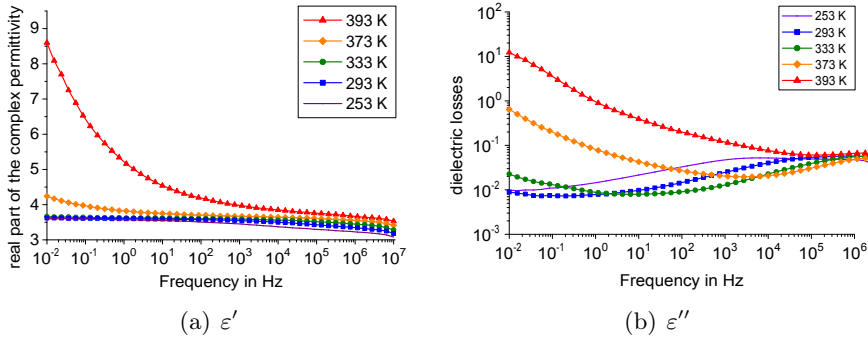


Figure 5.2.: Real (a) and imaginary part (b) of the complex permittivity of unmodified epoxy for different temperatures as a function of frequency.

to a β -relaxation process. The β relaxation is attributed to the mobility of side chains in the polymer. The shift of the β -relaxation peak can be easily seen in Figure 5.3, where the ϵ'' is shown for different frequencies as function of temperature. The peak shifts from 191 K at 10⁰ Hz to 286 K at 10⁵ Hz. The α -relaxation peak is located at 383 K, but is obscured by the DC conductivity, which increases greatly above T_g . The location of this α -peak was confirmed with DMTA (dynamic mechanical thermal analysis, see Appendix A.5). Relative permittivity for 393 K and 1.15 kHz¹ is 3.48.

5.4. Impact of curing time and particle modification

Figure 5.4(a) illustrates how the curing time can alter the relative permittivity of a MC. The samples are identical in terms of processing, host and filler materials. Figure 5.4(b) shows the impact of the surface modification. Neat ER and Al₂O₃-ER conventional filled composite (CFC) with an average particle diameter of 4 μ m and a fillgrade of 10 wt.% have been

¹The frequency of 1.15 kHz was chosen because at this frequency there is no influence of DC conductivity, Maxwell-Wagner polarization etc., which makes comparison easier.

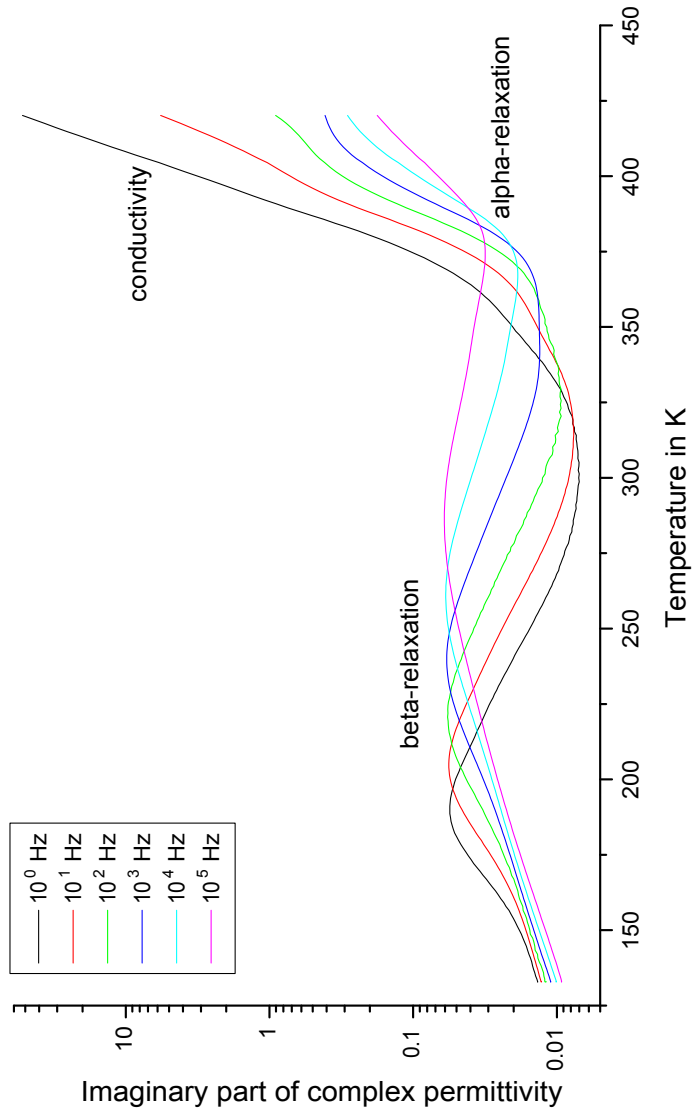


Figure 5.3.: Imaginary part of the complex permittivity of unfilled epoxy at different frequencies as function of temperature.

5.4. Impact of curing time and particle modification

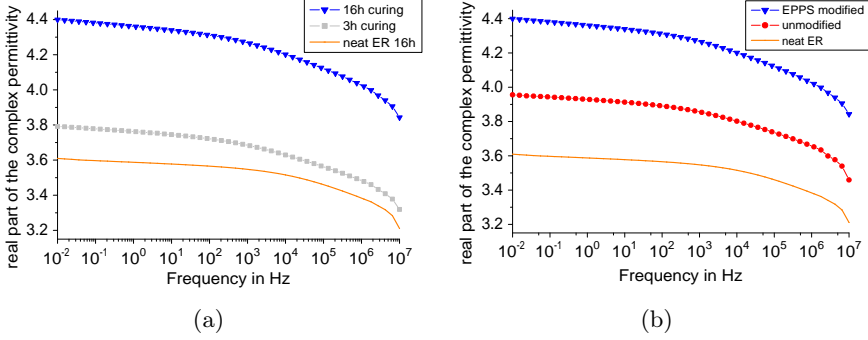


Figure 5.4.: Impact of the curing time (a) on the real part of the complex permittivity of conventional filled Al_2O_3 -ER with 10 wt.% fillgrade at 293 K as a function of frequency. The figure on the right (b) shows the impact of the particle modification on a Al_2O_3 -ER CFC with 10 wt.% fillgrade at 293 K.

produced: one batch of samples with and one without EPPS modification on the particle surfaces. Figure 5.4(a) shows ϵ' of samples that have been cured for 3 and 16 hours at 413 K respectively. All sample types have been subsequently postcured for 24 hours at 413 K. We can observe an increase of the relative permittivity in conventional filled composites with longer curing time, albeit there was no difference in the frequency dependence of ϵ' values of the unfilled epoxy. The measured values for ϵ' of conventional filled composites with modified and unmodified particles are almost identical for a curing time of 3 hours ($\epsilon'=3.7$ at 1.15 kHz). With a curing time of 16 hours the difference between conventional filled composites with modified ($\epsilon'=4.2$) and non-modified particles ($\epsilon'=3.9$) is well pronounced (Figure 5.4(b)).

One of the things many publications about NC share, are comparisons to MC. In most cases the chemistry involved in creating the samples with microscale filler is neglected. It has been shown that surface functionalization of nanoparticles is crucial for the properties of nanocomposites [98], but the influence of surface functionalization on micron sized filler is not taken into account. In light of the results shown in Figure 5.4, the com-

parisons between nano- and microscale filler, without detailed knowledge of chemical processes involved, have to be taken into consideration.

5.5. Filler Type

Figure 5.5 shows the impact of NP with a fillgrade of 2 wt.% on the ϵ' of the NC, as a function of frequency. Nanocomposites with 2 wt.% are shown, because at this fillgrade the changes due to the nanoparticles are the most pronounced. This behaviour is explained in Section 5.6, which discusses the influence of the fillgrade on NC.

The unfilled polymer shows higher values for ϵ' than the NC, as illustrated in Figure 5.5(a) for 293 K. This can be explained by the immobilization of the layer around the NP. For most of the frequency spectrum the reduction of ϵ' due to the NP seems independent from the frequency. For the imaginary part ϵ'' a peak at 10^5 Hz can be seen for neat ER and MgO-ER, which is absent in Al_2O_3 -ER (Figure 5.6(a)). MgO additionally leads to an increase of ϵ'' below 10^{-1} Hz, which can not be found in the other composites. Closer inspection of the peak at 10^5 Hz in Figure 5.7(a) reveals increased losses for MgO-ER, compared to neat ER, in this region.

At 353 K the ϵ' sees an even increase for all samples (Figure 5.5(b)). Below 10^{-1} Hz the offshoots from peaks due to T_g , DC conductivity and Maxwell-Wagner polarization start to show. The imaginary part (Figure 5.6(b)) shows similar behaviour for all specimens at 353 K.

Figure 5.9 shows the ϵ'' of Al_2O_3 -ER with 2 wt.% as function of temperature. The β -relaxation process is similar to neat epoxy, but at the peak is shifted to a slightly higher temperature. AlN-ER shows very similar behaviour to Al_2O_3 -ER. In MgO-ER the shift is more pronounced, which reflects in the Arrhenius plot (Figure 5.8). Composites with SiO_2 on the other hand saw a shift of the β -peak to lower temperatures compared to unfilled epoxy. From the Arrhenius plot the activation energy for unfilled epoxy could be determined as 2.79 eV. Activation energies of the side chains of NC with 2 wt.% have been compiled in Table 5.1 and differ only marginally.

5.5. Filler Type

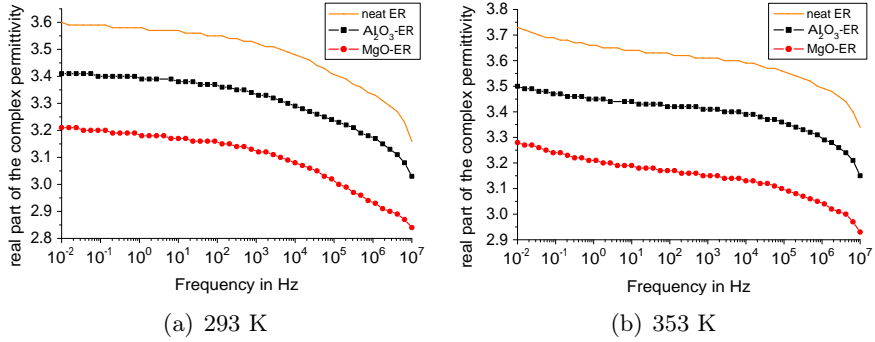


Figure 5.5.: Impact of the filler type on the real part of the complex permittivity of NC with 2 wt.%, for 292 K (a) and 353 K (b), compared to neat ER as a function of frequency.

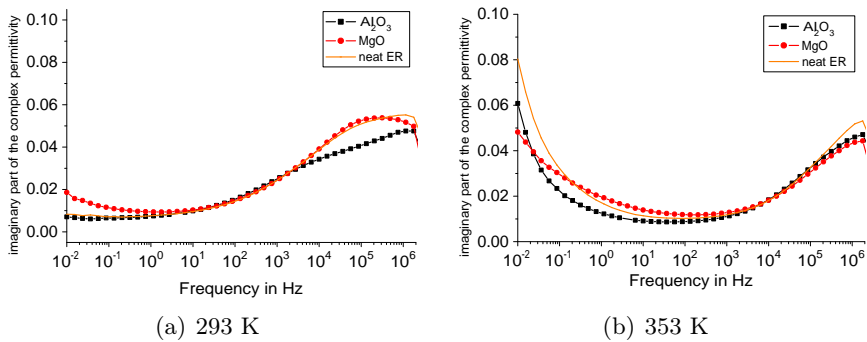


Figure 5.6.: Impact of the filler type on the imaginary part of the complex permittivity for 293 K (a) and 353 K (b), compared to neat ER as a function of frequency.

5.5. Filler Type

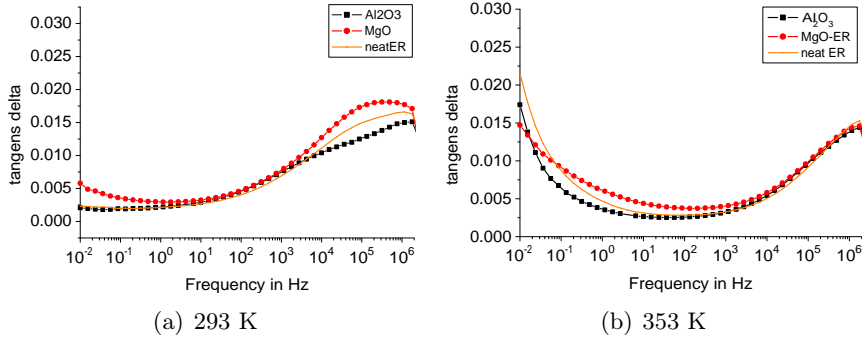


Figure 5.7.: Impact of the filler type on the $\tan(\delta)$ of the complex permittivity for 293 K (a) and 353 K (b), compared to neat ER as a function of frequency.

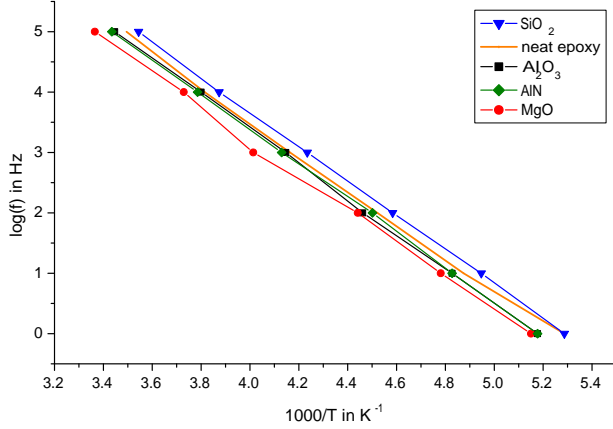


Figure 5.8.: Arrhenius plot for unfilled epoxy compared to NC with different filler types. Activation energies derived from this plot are given in Table 5.1.

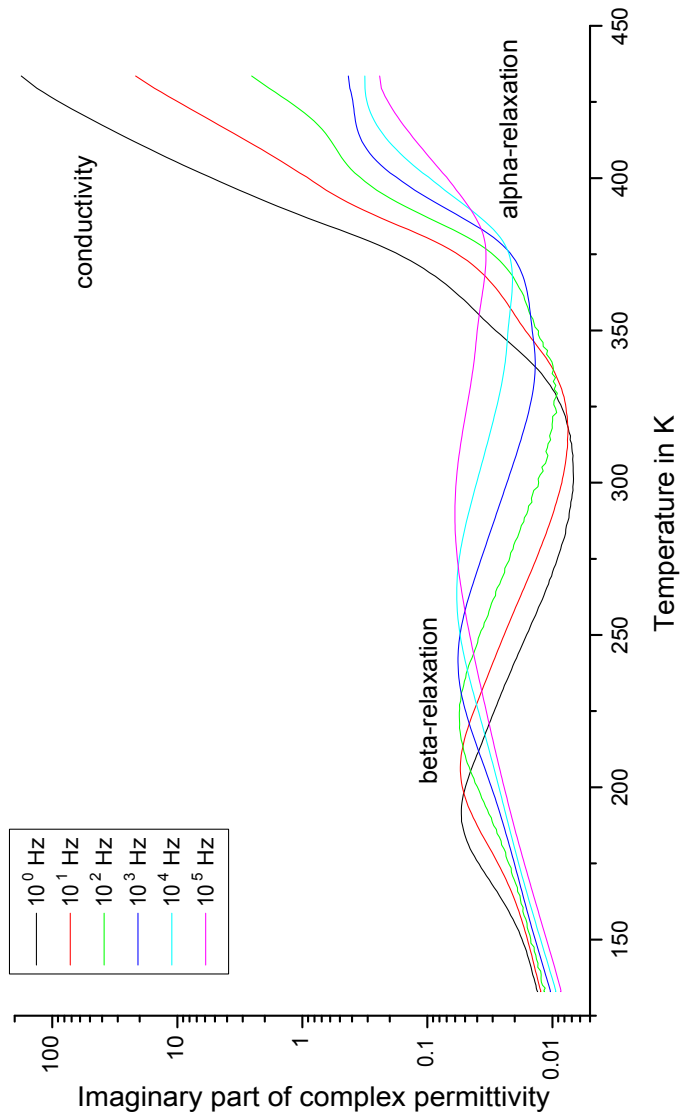


Figure 5.9.: Imaginary part of the complex permittivity of $\text{Al}_2\text{O}_3\text{-ER}$ with 2 wt.% at different frequencies as function of temperature.

5.6. Fillgrade

Table 5.1.: Activation energies derived from Arrhenius plot (Figure 5.8).

Filler type	Activation energy
none	2.79 eV
Al ₂ O ₃	2.9 eV
AlN	2.87 eV
MgO	2.79 eV
SiO ₂	2.85 eV

5.6. Fillgrade

Figure 5.10 shows the ϵ' for MgO-ER as a function of frequency for 293 K. It is apparent that ϵ' of most NC is below ϵ' of the unfilled polymer. This is mainly due to the immobilization of the polymer chains in the aligned layer around each particle. According to these measurements, the influence of nanoparticles on the bulk properties is the same for the whole frequency range. The imaginary part ϵ'' can be seen in Figure 5.11. The unfilled resin features a well pronounced peak at $4 \cdot 10^5$ Hz, while it resembles an even slope for the NC. Values for ϵ'' of NC are virtually identical above 10^1 Hz. Below this frequency ϵ'' shows an increase in specimens with higher fillgrade, while the unfilled resin shows a small decrease.

We observed that ϵ' is the lowest for a fillgrade of 2 wt.% for all investigated NC types, as shown in Figure 5.12. The value of ϵ' at 0.5 wt.% is the second lowest, followed by ϵ' at 5 wt.%. Thus the minimum lies probably at or close to 2 wt.%. The restructuring of the polymer due to the immobile polymer chains around EPPS modified nanoparticles is the most distinctive here. Above this local minimum the zones of the epoxy which are affected by EPPS and NP start to overlap. As the volume of filler material increases, the influence of the material properties of the particles on ϵ' of the bulk material also becomes more pronounced. They start to overshadow the reduction of the ϵ' , which is due to the rigid layers around the nanoparticles. Below the local minimum the amount of rigid aligned zones is lower, hence the smaller impact on the permittivity.

The relative permittivity of composites with Nanopox is higher than that of both the unfilled epoxy and the filler material. This can indicate two things. The particles grown during in-situ polymerization are not modified

5.6. Fillgrade

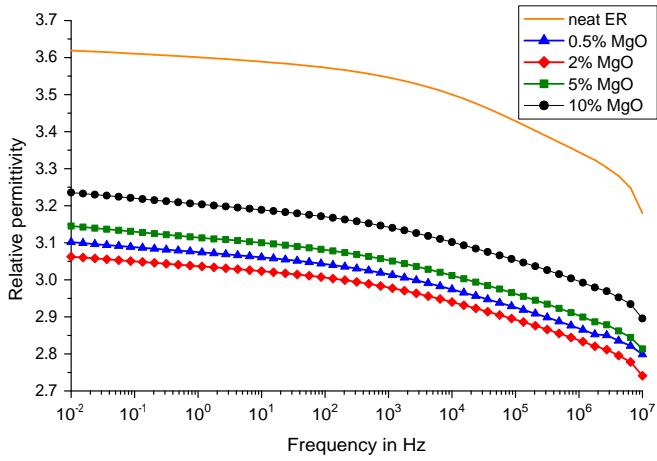


Figure 5.10.: Real part of the complex permittivity of MgO-ER nanocomposites at 293 K compared to neat ER as a function of frequency.

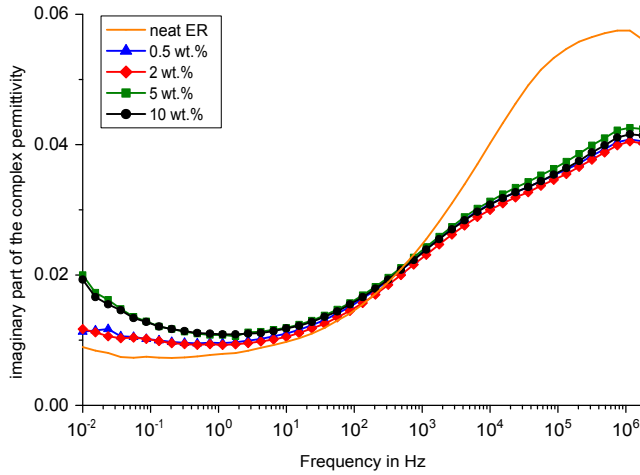


Figure 5.11.: Imaginary part of the complex permittivity of MgO-ER nanocomposites at 293 K compared to neat ER as a function of frequency.

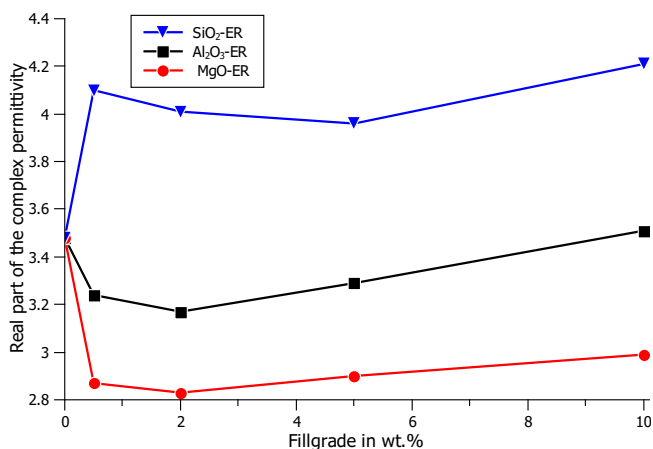


Figure 5.12.: Relative permittivity of Al₂O₃-ER, MgO-ER and SiO₂ NC for 1.15 kHz at 293 K as a function of fillgrade.

with EPPS or any other coupling agent. Therefore the interfacial region could differ greatly from the layered structures that are indicated for EPPS modified nanoparticles. The chains could align parallel instead of perpendicular to the particle surfaces for example. Another possibility is that the in-situ polymerization of nanoparticles also introduces other residues. These residues seem to be very mobile and increase the relative permittivity by approximately 25%. However, we observe a similar behaviour of the ϵ' as a function of fillgrade, since the samples with 2 wt.% show the lowest ϵ' values for Nanopox-based specimen.

Values for Al₂O₃-ER NC range between 3.2 and 3.5, being up to 9 % lower than the unfilled epoxy with 3.5. The addition of modified alumina fillers with an average diameter of 4 μm on the other hand, result in a permittivity increase of up to 19 % for 10 wt.% fillgrade. Specimens with MgO nanoparticles have the lowest values tested, between 2.8 and 3, which is a reduction by 15 to 19 %, compared to the neat ER.

The ϵ' for Al₂O₃ is between 9.5 and 10 depending on the structure [99]. The ϵ' of MgO is around 5. According to conventional mixture rules for

5.6. Fillgrade

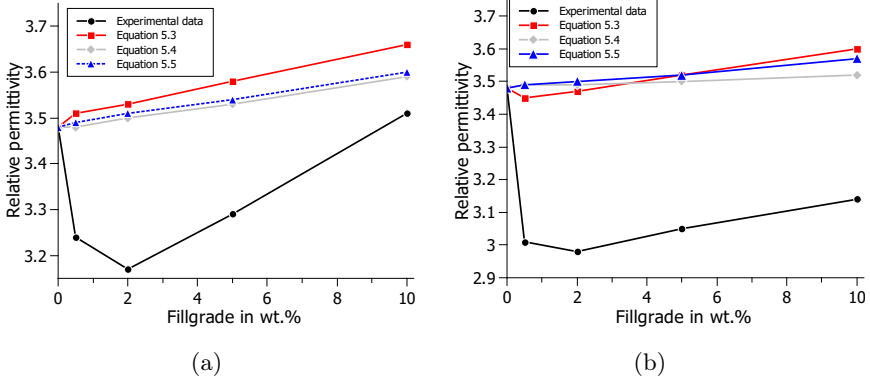


Figure 5.13.: Comparison of calculated and measured values for Al₂O₃-ER (a) and MgO-ER (b).

composites – like the logarithmic Looyenga formula (5.3), or semi-empiric models (5.4) and (5.5) [100, 101, 102] – the permittivity of the compound should be higher than the base material. In these formulas ε_c , ε_m and ε_f represent the relative permittivities of the composite, matrix and filler materials while ϕ is the volume fraction of the filler. These rules do not anticipate changes on the molecular level, thus they don't apply for very small filler content and small particles. For example, in specimens with 0.5 and 2wt.% Al₂O₃-ER the particles occupy only 0.16 and 0.66 % of the volume respectively.

$$\log \varepsilon_c = \phi \cdot \log \varepsilon_f + (1 - \phi) \cdot \log \varepsilon_m \quad (5.3)$$

$$\varepsilon_c = \frac{(1 - \phi) \cdot \varepsilon_m \cdot \left(\frac{2}{3} + \frac{\varepsilon_f}{3\varepsilon_m}\right) + \phi \cdot \varepsilon_f}{(1 - \phi) \cdot \left(\frac{2}{3} + \frac{\varepsilon_f}{3\varepsilon_m}\right) + \phi} \quad (5.4)$$

$$\varepsilon_c = \varepsilon_m + \frac{2 \cdot \phi \cdot \varepsilon_m \cdot \varepsilon_f}{2\varepsilon_m + (1 - \phi) \cdot \varepsilon_f} \quad (5.5)$$

The immobilization of the polymer layer is not considered by either effective medium or integral methods. This immobilization seems to be the

main factor determining the ε' of composites with surface functionalized particles below 10 wt.% fillgrade. Since the conventional approach for calculating the permittivity of mixtures does not consider this, it is easy to see why the values calculated with these equations differ from experimental data, as shown in Figure 5.13.

Experimentally obtained values of the relative permittivity from 2 to 10 wt.% increase in a linear fashion. For MgO-ER the slope appears to be similar to the values calculated with Equation 5.3, as shown in Figure 5.13(b), however with different y-intercept. Al₂O₃-ER on the other hand has no similarity to any of the calculated values (Figure 5.13(a)).

5.7. Filler Size

Figure 5.14 shows the comparison of CFC and NC with Al₂O₃-filler of 4 μm and 50 nm average diameter respectively. Microsized filler was used both as-received and with surface modification. It is apparent that permittivity values for samples with modified microparticles are higher than with unmodified. This is probably due to the better bonds between the filler and the host material. Opposed to NC we also see frequency dependent changes to the relative permittivity of CFC. Above 100 Hz the ε' of samples with unmodified microparticles is lower than in the neat epoxy. Above 10 kHz it is even lower than for samples with nanoscale filler. Specimens with 10 wt.% see an increase in permittivity compared to those with 5 wt.%. This is due to the high permittivity of the filler material, compared to the host material. At 1.15 kHz we see an increase of the permittivity by 9 % for Al₂O₃-ER with 10 wt.% unmodified filler, while the increase for specimen with the same amount of EPPS-modified microscale filler is almost double of that with 19 %. The dielectric loss spectrum shows no significant changes compared to the spectrum of neat ER.

Figure 5.15 shows the dielectric loss spectra for samples with 5 wt.% Al₂O₃ for 293 K. Samples with unmodified particles show the highest losses, seconded by values for EPPS-modified conventional filled composites, while NC with modified particles exhibit the lowest values. What sets both NC and CFC apart from neat ER is the slope starting at $5 \cdot 10^3$ Hz,

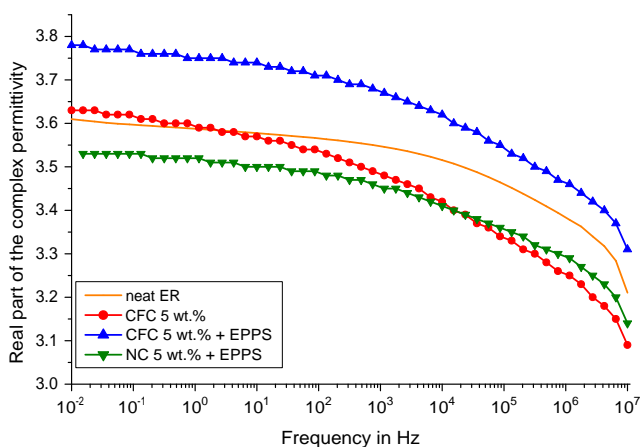


Figure 5.14.: Real part of the complex permittivity at 293 K for composites with 5wt.% Al_2O_3 , compared to neat ER as a function of frequency.

while neat ER has a distinct peak at 10^6 Hz. For frequencies below $5 \cdot 10^3$ Hz the spectra for NC and CFC are very similar to the neat epoxy, apart from minor differences in magnitude.

Figure 5.16 indicates a direct impact of the filler size on the dielectric properties of BN-ER composites. It shows an increase of the relative permittivity ϵ' with an increase of both the average filler size and temperature. Raising the temperature increases the kinetic energy, which leads to a movement of the particles on the molecular level. There is a similarity between neat ER and composites with BN filler of an average size of 70 nm. The values for ϵ' differ by less than 2 % for these two compounds, with the BN-ER nanocomposite usually having the lower values (Figure 5.16).

For the neat ER samples ϵ' has a value of 3.48 at 293 K and 1.15 kHz, while values for BN that can be found in literature are typically above 4. For calculations we used a value of 4.48 for BN [103]. The similarity of results for neat ER and BN-ER with 70 nm particles is probably due to an immobilization of polymer chains around the particles, which counter the increased mobility due to the filler material.

5.7. Filler Size

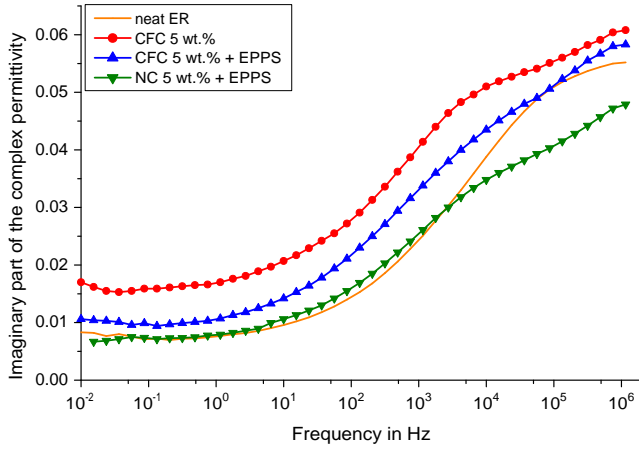


Figure 5.15.: Dielectric losses at 293 K for composites with 5wt.% Al_2O_3 compared to neat ER as a function of frequency.

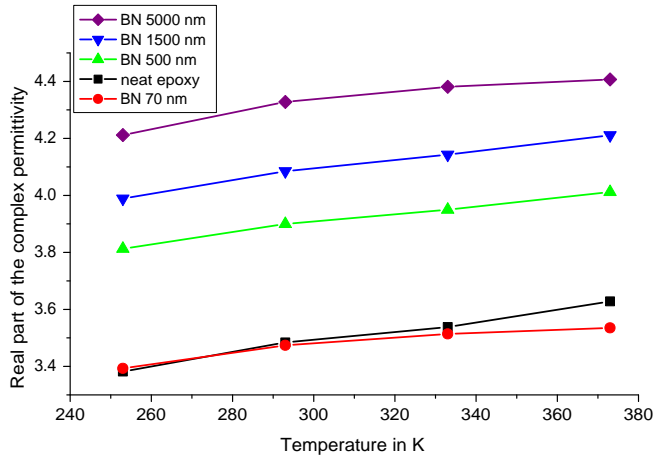


Figure 5.16.: Real part of the complex permittivity of BN-ER nanocomposites with a fillgrade of 10 wt.% at 1.15 kHz, compared to neat ER as a function of temperature.

5.8. Summary

Table 5.2.: Measured values for ϵ' of BN-ER NC at 1.15 kHz compared to values obtained by rules of mixture.

Fillersize in nm	Equation number	ϵ'
70	measurement	3.4
500	measurement	3.9
1500	measurement	4.1
5000	measurement	4.3
-	5.3	3.5
-	5.4	3.5
-	5.5	3.6

Mixture rules have been used to predict the relative permittivity of the composites, specifically (5.3), (5.4) and (5.5). The values calculated did not agree well with the measurement, as can be seen in Table 5.2.

The measured values for BN-ER composites correspond very well to a two parameter natural logarithmic function, like (5.6) below, at 1.15 kHz and 293 K, where d_a is the average diameter of the filler material. This function can be written more general in form (5.7), where parameters A and B are depending on material constants and other factors, e.g. the permittivity of the host and filler material, as well as the volume fraction of the filler.

$$\epsilon'_c = 2.64 + 0.1987 \ln(d_a) \tag{5.6}$$

$$\epsilon'_c = A(\text{var}) + B(\text{var}) \ln(d_a) \tag{5.7}$$

5.8. Summary

Due to the alignment of polymer chains on the particle surface we see an immobilization around the respective particles [104]. This reflects in a low relative permittivity ϵ' of this layer. For NC with low fillgrades we therefore see a reduction of the ϵ' of the composite, even if the ϵ' of the filler material is higher than the unfilled resin. At a certain fillgrade, which seems dependent on the ϵ' of the filler relative to the polymer and the average filler size, the ϵ' surpasses the value of the polymer. The size of

the filler plays an important role. Since the volume of interfaces increases for decreasing filler size at constant weight percentage, the move to smaller filler results in larger zones of immobilization. The larger the particles are, the larger the influence of the filler properties become compared to the changes to the polymer structure and the influence of the immobilized layers diminishes. This immobilization can be interpreted as formation of crystalline layers around the particles.

Differences of the imaginary part ε'' between neat ER and NC can mainly be seen at frequencies above 10^3 Hz. Below 1 Hz some NC show increased losses, but no significant changes. The ε'' does not change significantly for NC as a function of fillgrade.

The β -relaxation peak moves to higher temperature for nanocomposites, but the observed effects are minor. Exception are SiO₂ NC, in which the maximum of the β -relaxation shifts to lower temperatures. The activation energy of the β -relaxation for NC show only minor differences to unfilled epoxy, where the activation energy is 2.79 eV.

CHAPTER 6

SPACE CHARGES

The great tragedy of Science - the slaying of a beautiful hypothesis by an ugly fact.

-Thomas Henry Huxley

Space charge (SC) measurements provide information about the distribution of the electric field and provide markers for the ageing state of an insulation material [83]. It is still subject to debate if SC are cause, symptom, or both for ageing of insulating materials. Nonetheless, since an increase of the SC density either indicates or causes ageing, SC are considered a limiting factor for HVDC applications [105]. In this chapter the SC dynamics and SC profiles of NC are investigated. The space charge behaviour of NC during voltage application (poling) and after voltage application (depoling) is analyzed.

6.1. Measurement Principle

The pulsed electro acoustic (PEA) method was used for measuring the dynamic SC distribution in flat, solid insulators [106]. Details about the

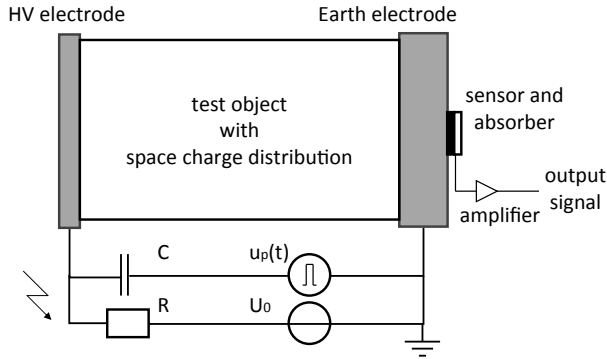


Figure 6.1.: Equivalent circuit diagram of the sample configuration and test setup for space charge measurements with the PEA method.

setup and the measurement technique can be found in Appendix B.2.

6.1.1. Measurement setup

The test setup is illustrated in Figure 6.1. An electric pulse $u_p(t)$ is applied to the sample. In case SC are present, this pulse induces a perturbation force on each charge. Due to this force the charges move slightly, consequently launching an acoustic wave proportional to the charge distribution in the sample. The acoustic wave can be detected and transformed into an electric signal by using a piezoelectric transducer. However, the detected signal does not represent the acoustic signal at the sensor, since the sensor-amplifier system acts as high pass filter. Deconvolution techniques are used to take this into account.

6.1.2. Measurement process

The measurement process can be divided in four stages: calibration, poling, depoling and signal processing. Poling, the application of an electric field to the sample, was typically applied for 1 hour. The data acquisition starts with the application of the poling voltage and is continuously until the

end of depoling. All samples reached a steady state within the poling time. Poling fields were applied of 10, 15 and 18 kV/mm. The voltage was subsequently switched off to allow the depoling process to start. Since polarization at electrode-dielectric interfaces is usually a dominating factor during poling, SC in the bulk of the material can best be seen during the depoling stage. This stage lasted up to two hours, after which all samples were charge free. An amplifier bolstered the signal from the piezoelectric transducer, which in turn could be acquired by an oscilloscope during the whole measurement process. The signal underwent processing with Matlab (for details see Appendix B.2).

6.2. Sample Preparation

Polymeric samples for SC measurement were cleaned with ethanol and dried afterwards. To ensure good connection between HV electrode and sample and to reduce reflections, a soft semi-conducting layer was applied between them. The semi-conducting layer also allows the measurement of charges at the HV electrode. Most of the measurement signal would otherwise disappear in the HV electrode and only a small part reflected back to the sensor. At the earth electrode silicon oil was used to improve the acoustic properties at this interface. Samples were 50 mm in diameter and ranged in thickness between 0.5 and 1 mm. The pulse width of the setup was 10 ns with an amplitude of 600 V for samples of less than 1 mm thickness. For thicker samples a pulse width of 20 ns was chosen with the same amplitude of 600 V. For electric field strengths close to 20 kV/mm, surface flashover could occur because the creepage length was relatively short. A rubber sheet was utilized to increase the creepage length (see Figure 6.2). This sheet has a hole in the centre, allowing contact of the HV electrode with the specimen. The sheet also reduces the field enhancement at the semi-conducting layer.

6.2.1. Spatial resolution

The spatial resolution s can be calculated as in Equation 6.1 with v_s being the sound velocity and ΔT the pulse width. For epoxy with a v_s of

6.3. Space Charge Parameters

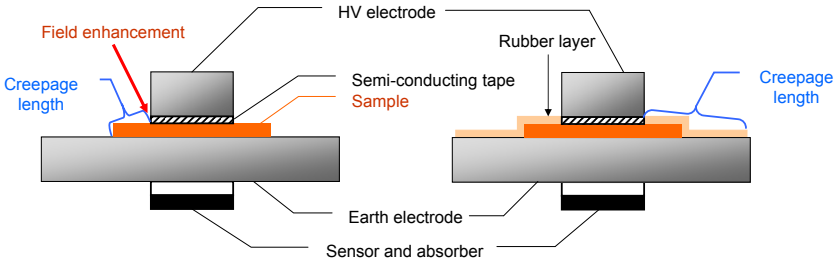


Figure 6.2.: Illustration of the increase of the creepage length by utilizing a rubber layer.

2650 m/s the spatial resolution can be calculated as $25 \mu\text{m}$ for a pulse width of 10 ns. For a pulse width of 20 ns s equals $53 \mu\text{m}$.

$$s = v_s \cdot \Delta T \quad (6.1)$$

6.3. Space Charge Parameters

During post-processing of the measurement data, the average amount of charges in the sample was determined. For this we integrated the absolute charge value over the sample thickness and divided by the sample thickness (see Appendix B.2 for details). The average charge value is the parameter on which we focus on during the stages of charge accumulation and depletion. From the change of the average charge over time during poling and depoling, the time constant until saturation and discharge could be derived.

In space charge profiles the charge at the earth electrode is usually dominant, due to its location close to the sensor. This is a parameter which is easy to quantify and compare. During poling the charges at the electrodes often overshadow charge in the bulk of the sample. Hence the location and magnitude of charges in the bulk can be determined best immediately after the poling voltage has been disconnected (voltage-off measurement).

6.3.1. Field enhancement factor

The field enhancement factor F_E indicates the deviation of the electrical field distribution from the uniform field distribution along a specimen. It can be calculated according to Equation 6.2, where E_{max} is the maximum field strength in the sample, E_{DC} is the applied DC voltage per mm. Without any space charges, the field enhancement factor equals zero. F_E is time dependent, since the maximum field strength in a sample changes during poling and depoling. More details can be found in Appendix B.2.

$$F_E = \frac{E_{max} - E_{DC}}{E_{DC}} \quad (6.2)$$

6.4. Space Charge Accumulation

Figure 6.3 shows the average amount of space charge in MgO-ER samples compared to neat ER as a function of time, for a poling field of 15 kV/mm. All MgO-samples had considerably lower space charge densities than the reference sample. After 1 hour of poling the amount of charges in the neat ER sample was three times higher than in any of the MgO-ER-composites. MgO exhibits faster charge dynamics than the unfilled epoxy. After less than 15 minutes MgO-ER samples reached their saturation point, while the neat ER sample was still accumulating charges. For Al₂O₃-ER NC we observe a different behaviour, as shown in Figure 6.4. Two of the NC show a charge growth that exceeds the growth in neat ER, while specimens with 2 wt.% show results similar to MgO-ER samples. Figure 6.5 shows the charge buildup in AlN-ER NC. For these specimens with both 0.5 and 2 wt.% show reduced space charge, while 5% samples show an increase.

The preparation of NC with the first batch of BN particles had some problems. Crimp et al. [107] showed that the stability of hexagonal BN in a suspension is dependent on the degree of oxidation of the particles. Layers of B₂O₃ on the surfaces of the BN-particles used for initial experiments prevented stable suspension formation. Essentially the B₂O₃ shell adds another electrical double layer to each particle, subsequently leading to an increased ζ -potential. BN particles with a high B₂O₃ content show a

6.4. Space Charge Accumulation

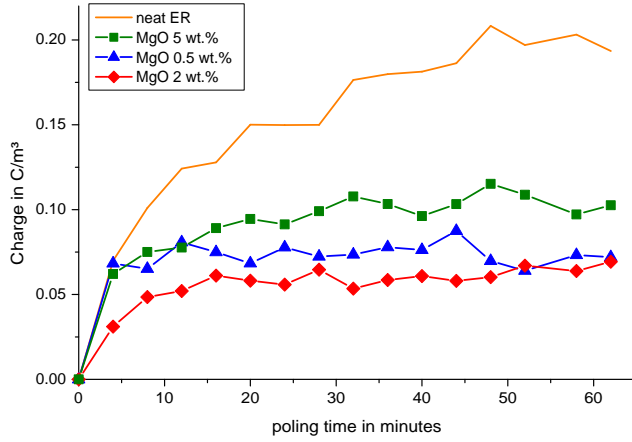


Figure 6.3.: Growth of average space charge for MgO-ER-composites compared to neat ER for 15 kV/mm poling field at 293 K (voltage-on measurement).

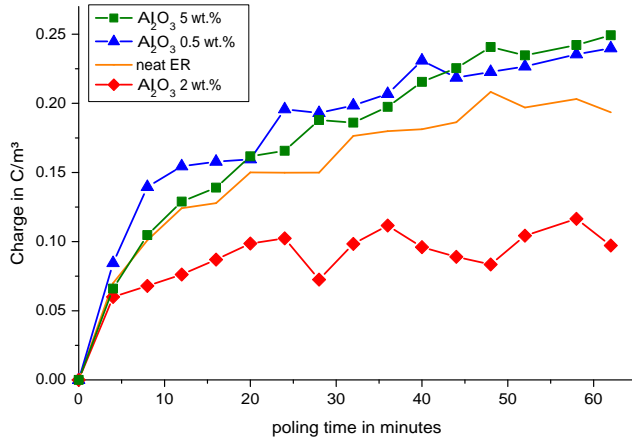


Figure 6.4.: Growth of average space charge for Al₂O₃-ER-composites compared to neat ER for 15 kV/mm poling field at 293 K (voltage-on measurement).

6.4. Space Charge Accumulation

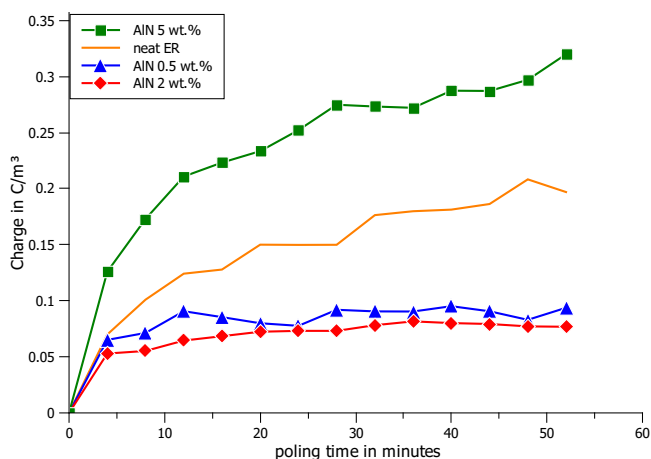


Figure 6.5.: Growth of average space charge for AlN-ER-composites compared to neat ER for 15 kV/mm poling field at 293 K (voltage-on measurement).

significant ζ potential of -60 to -80 mV from pH 6-10, thereby lowering the barrier to agglomeration. Even at pH 3 the value of ζ is still larger than -25 mV. Stable, dispersed suspensions have typically ζ potentials between -25.7 mV and +25.7 mV. At lower pH than 3 we observed monopolymerization of CY231, making it impossible to go below pH 3 during synthesis. Due to these limitations, the suspension of BN and epoxy was not satisfactory. This led to an increased amount of agglomerations, as verified by means of TEM. TEM analysis also showed that the amorphous BN nanoparticles (average particle diameter 20 nm) were surrounded by a crystalline B_2O_3 -layer of 3 to 5 nm thickness.

As seen in Figure 6.7, these BN-ER-composites share the fast charge dynamics of MgO-ER, but the amount of space charges is considerably higher. After 1 hour of charging the 0.5 wt.% BN-ER sample had double the amount of space charges that we observed in the reference sample, matters being worse with 2 wt.% BN-ER (Figure 6.6). Compared to the other samples, the 2 wt.% BN-ER-composite shows large amounts of space charges almost immediately after voltage application. For example, after

6.5. Space Charge Profiles

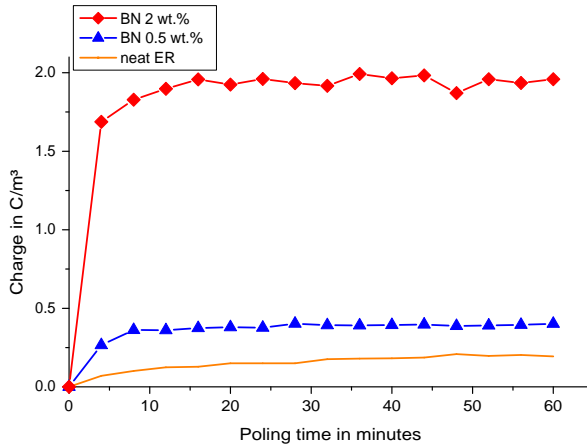


Figure 6.6.: Growth of average space charge for BN-ER-composites compared to neat ER for 15 kV/mm poling field at 293 K (voltage-on measurement).

1 hour of poling at 18 kV/mm, the amount of charges in 2wt.% BN-ER samples is 10 times higher than in neat ER.

The BN-ER samples investigated in Chapters 4 and 5 were synthesized with BN particles from a different supplier. Hence the results from BN-ER from this chapter are not correlated with results in Chapters 4 and 5.

6.5. Space Charge Profiles

6.5.1. Unmodified epoxy

Figure 6.8 shows the voltage-off space charge profile for unmodified epoxy after poling for one hour at room temperature. The x-axis represents the normalized thickness of the respective sample. The high voltage electrode is located on the left side, while the earth electrode is located on the right for all graphs. Some charge accumulation can be observed at the earth electrode, but no charge buildup in the bulk of the material. Hence the electrode charge is dominant for the space charge behaviour at

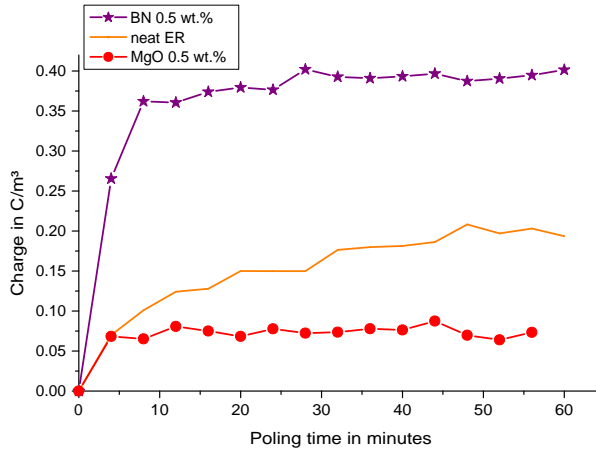


Figure 6.7.: Growth of average space charge for BN-ER-composites compared to neat ER for 15 kV/mm poling field at 293 K (voltage-on measurement).

room temperature. At elevated temperatures this changes, as we can see heterocharge building up in the bulk of the material (Figure 6.9). A direct comparison of the evolution of SC over time, along the thickness of the sample for a poling field of 18 kV/mm, can be seen in Figure 6.10. Figure 6.10(a) shows the evolution of charges over time at 293 K, while Figure 6.10(c) shows charge accumulation at 333 K. A buildup of a large amount of heterocharge can be seen in the bulk of the material at 333 K. Behaviour during depoling is illustrated in Figure 6.10(b) for 293 K and Figure 6.10(d) for 333 K. The heterocharge, which formed during poling at 333 K, takes two hours to be discharged.

6.5.2. MgO Nanocomposites

Figure 6.11 shows typical space charge profiles for MgO-ER samples. The amount of space charge is drastically reduced for MgO-ER-composites, compared to the neat epoxy. For higher temperatures we see the formation of homocharge in the bulk (Figure 6.12). These charges are smaller than in

6.5. Space Charge Profiles

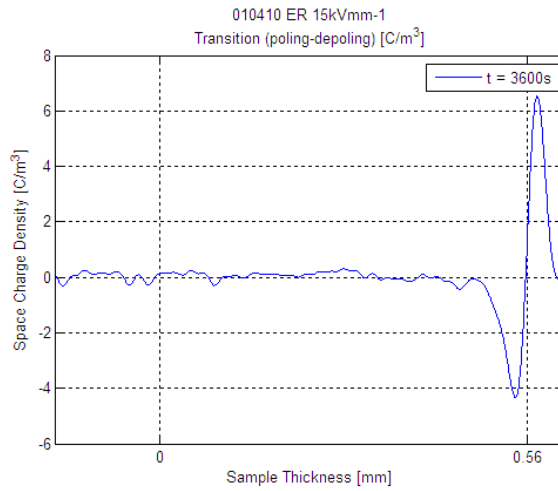


Figure 6.8.: Space charge profiles of unfilled epoxy for different poling field strengths after 1 hour of poling (voltage-off-profile) at 273 K.

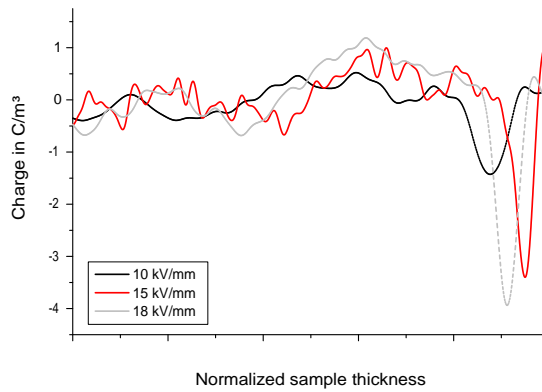


Figure 6.9.: Space charge profiles of unfilled epoxy for different poling field strengths after 1 hour of poling (voltage-off-profile) at 333 K.

6.5. Space Charge Profiles

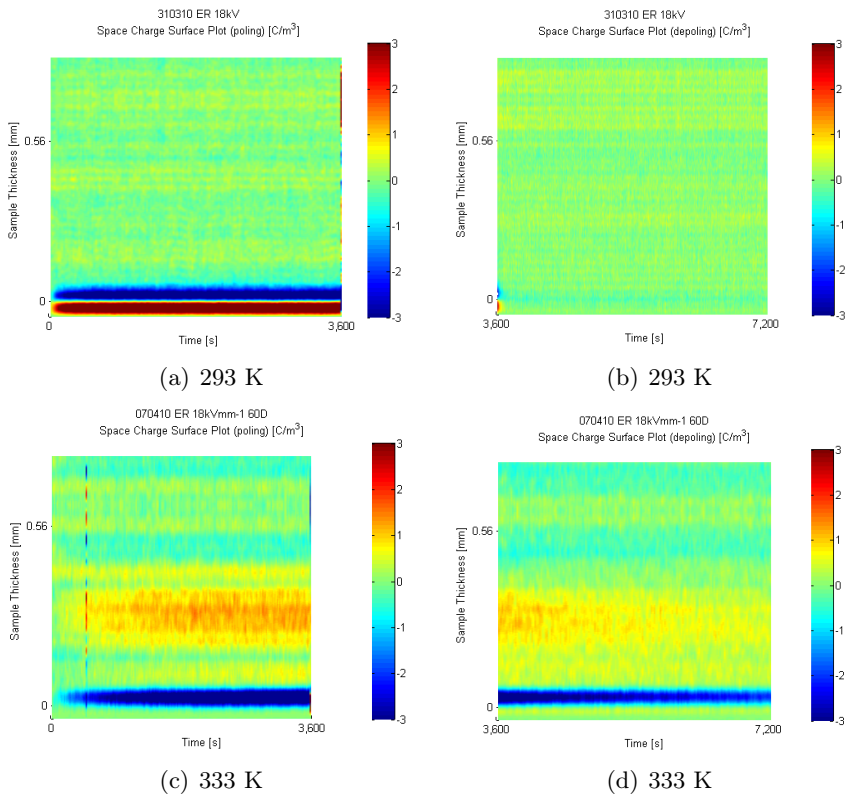


Figure 6.10.: Evolution of SC over time along the thickness of the sample, for unfilled epoxy for a poling field of 18 kV/mm: poling at 293 K (a) and depoling at 293 K (b); poling at 333 K (c) depoling at 333 K (d).

6.5. Space Charge Profiles

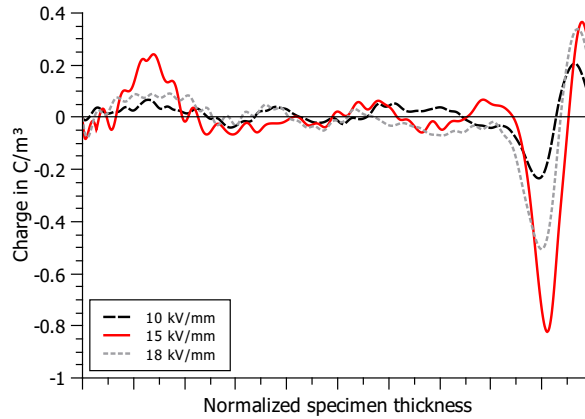


Figure 6.11.: Space charge profiles for MgO-ER with 5 wt.% fillgrade for different poling field strengths after 1 hour of poling (voltage-off-profile) at 293 K.

unfilled epoxy at the same temperature however. The evolution of SC over time along the thickness of MgO-ER samples with 5 wt.%, for a poling field of 18 kV/mm, can be seen in Figure 6.13(a) at 293 K and Figure 6.13(c) at 333 K. Comparison of Figures 6.10 and 6.13 shows three things: MgO-ER samples have an overall lower amount of SC than unfilled epoxy. At 333 K the difference is more pronounced than at 293 K. Secondly, the formation of heterocharge at the earth and HV electrode can be seen in Figure 6.13(c). The heterocharge can also be seen in the voltage-off profile (Figure 6.12). Thirdly the charge buildup at 333K is slower in MgO-ER, compared to unmodified epoxy, as evident in Figures 6.10(c) and 6.13(c). Corresponding plots for depoling are Figures 6.13(b) and 6.13(d). Here we observe a much faster charge mitigation at 333 K, compared to unfilled epoxy.

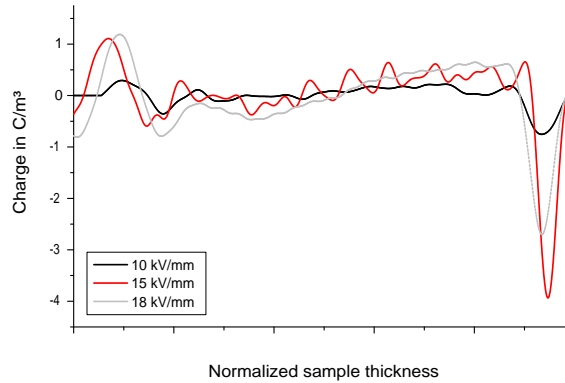


Figure 6.12.: Space charge profile for MgO-ER with 5 wt.% fillgrade for different poling field strengths after 1 hour of poling (voltage-off-profile) at 333 K.

6.5.3. AlN and Al₂O₃ Nanocomposites

After observing the differences in space charge accumulation for Al₂O₃- and AlN-ER samples with different fillgrades, the space charge profiles of these samples were investigated in more detail. Figures 6.14 and 6.15 show space charge profiles at different field strengths for AlN-ER composites with a fillgrade of 2 and 5 wt.% respectively. It is apparent that the charge accumulation at the electrodes is much larger in specimens with 5 wt.%. AlN-ER with 2 wt.% shows charge profiles similar to MgO-ER (Figure 6.11) in terms of magnitude. AlN with 0.5 wt.%, as well as Al₂O₃-ER with 2 wt.% show similar SC profiles as AlN with 2 wt.%. Alumina filled epoxy with 0.5 and 5 wt.% on the other hand has similar behaviour as AlN-ER with 5 wt.%. The fillgrade of the NP seems to have only a minor influence on the space charge intake.

6.5. Space Charge Profiles

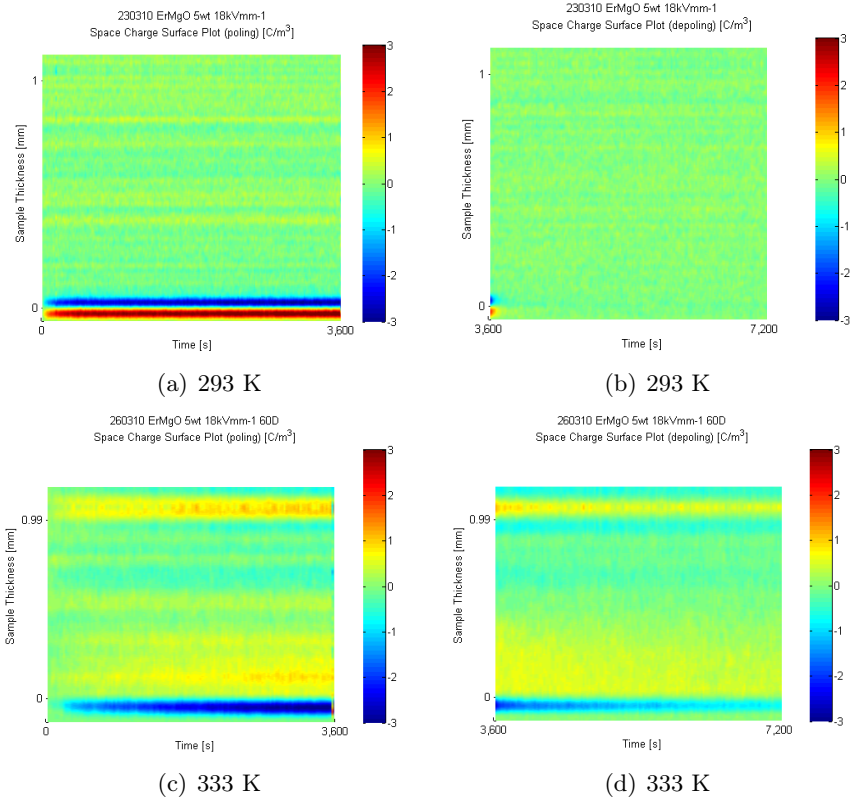


Figure 6.13.: Evolution of SC over time along the thickness of the sample, for MgO-ER with 5 wt.% for a poling field of 18 kV/mm: poling at 293 K (a) and depoling at 293 K (b); poling at 333 K (c) depoling at 333 K (d).

6.5. Space Charge Profiles

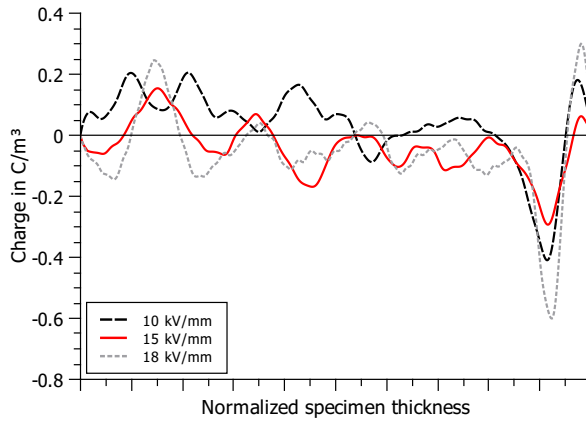


Figure 6.14.: Space charge profiles for AlN-ER with 2 wt.% fillgrade for different poling field strengths after 1 hour of poling at 293 K.

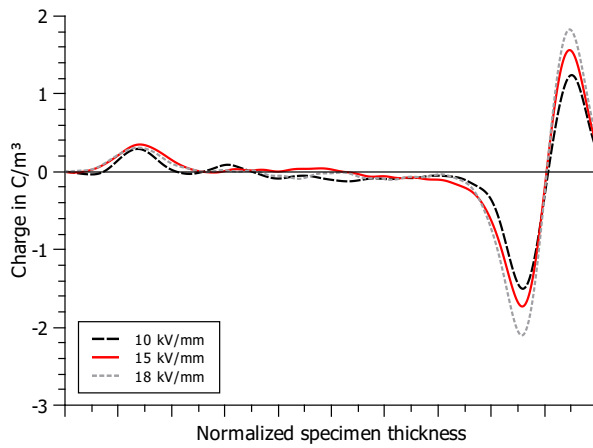


Figure 6.15.: Space charge profiles for AlN-ER with 5 wt.% fillgrade for different poling field strengths after 1 hour of poling at 293 K.

6.6. Charge Depletion During Depoling

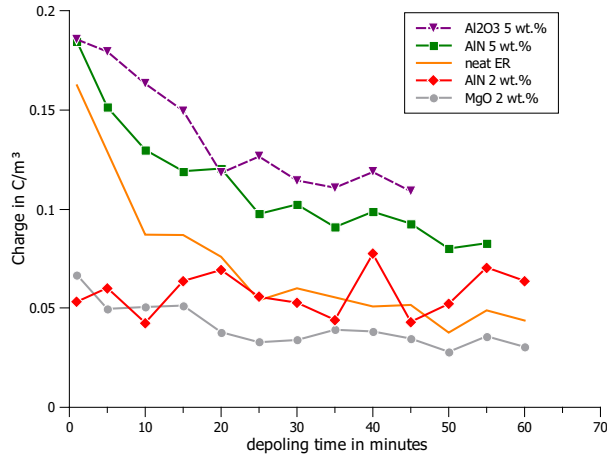


Figure 6.16.: Depletion of average space charge for different NC compared to neat ER for a poling field of 15 kV/mm at 293 K.

6.6. Charge Depletion During Depoling

Similar to the charging behaviour, we also see a fast depletion of space charges in NC. The average amount of space charge in various NCs compared to the reference can be seen in Figure 6.16. All MgO-ER-composites were charge free in less than 30 minutes, having very low space charge densities almost immediately. For other NC we observed a fast charge depletion for samples that had a low intake of charges to begin with, e.g. AlN with 2 wt.%. Samples with higher charge density, e.g. AlN-ER and Al₂O₃-ER with a fillgrade of 5 wt.% each, also showed slower charge dynamics than the unfilled base material.

BN-ER with 0.5 wt.% was charge free after 40 minutes, showing larger amounts of trapped charges than the reference sample. The BN-ER-composite with 2 wt.% showed the highest amount of space charges. After 1 hour of depoling with a poling field of 18 kV/mm, the charge was still 40 % higher than the peak value of the 2 % MgO-ER-sample during poling.

6.7. Electric Field

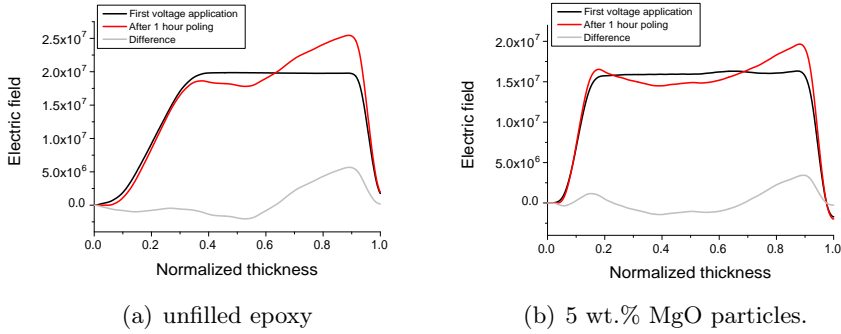


Figure 6.17.: Distribution of the electric field in unfilled epoxy (a) and MgO-ER with 5 wt.% (b) at 333 K.

6.7. Electric Field

Electric field plots have been created for unfilled epoxy and MgO-ER samples. Since the field enhancement is more distinct at higher field strengths, the following plots were obtained for poling fields of 18 kV/mm.

Figure 6.17 shows how the electric field distribution changes as result of a temperature increase to 333 K. Poling field strength was 18 kV/mm. It can be seen that the 5 wt.% MgO-filled sample (Figure 6.17(b)) has lower field enhancements than the unfilled epoxy (Figure 6.17(a)). The highest field enhancement can be found at the earth electrode, as a result of heterocharge at this electrode. Values for the field enhancement at the earth electrode can be found in Table 6.1. MgO-ER also shows heterocharge at the HV electrode and homocharge in the bulk. Unfilled epoxy on the other hand has homocharge at the HV electrode, leading to a field reduction.

6.8. Discussion

For AlN and Al₂O₃, the impact of the surface functionalized nanoparticles on the space charge behaviour unfolds in combination with TEM analysis. The correlation of TEM analysis and space charge measurement shows

6.9. Summary

Table 6.1.: Maximum field enhancement for unmodified epoxy and MgO-ER with 5 wt.% at different poling field strengths.

Filler type	10 kV/mm	15 kV/mm	18 kV/mm
unmodified at 293 K	12 %	8 %	16 %
at 333 K	25 %	36 %	58 %
MgO 5 wt.% at 293 K	20 %	20 %	15 %
at 333 K	22 %	26 %	33 %

that the quality of the particle dispersion has a considerable influence on the space charge behaviour of the nanocomposite. Samples which showed more agglomerates, also showed increased charge accumulation. This can be explained by the agglomerates of nanoparticles acting as charge traps. These charge traps could originate from various mechanisms. One possibility is self-trapping of electrons, which is suspected to occur in polymers. The field of a free electron can affect the molecular structure in the less rigid, amorphous regions of a polymer. A moving electron can cause a local potential drop. This potential drop can then attract an electron. The attracted electron is either the electron that established the drop, thus self-trapping, or an electron nearby [83]. Since agglomerates are zones where crystalline and amorphous regions interfere with each other and overlap, electrons find themselves restricted to travel through narrow amorphous corridors. Agglomerates could also lead to increased interfacial polarization and thus charge accumulation.

6.9. Summary

Nanocomposites with MgO-filler show a reduced intake of space charges during poling, compared to unmodified epoxy. At 333 K the field distribution changes considerably. Neat epoxy shows homocharge at the HV electrode and heterocharge in the centre and the earth electrode. With MgO NP on the other hand we observe heterocharge at both electrodes and homocharge in the centre of the sample. The maximum field enhancement at 333 K is 20 % lower in MgO-filled NC than in neat epoxy for a poling field of 18 kV/mm. The MgO nanocomposites also show slower

6.9. Summary

charge buildup at 333 K, in combination with faster charge dissipation during depoling. MgO filled NCs are charge free in less than half the time unfilled epoxy needs. NC with other fillers showed similar behaviour as MgO-filled NC for certain fillgrades.

In combination with TEM results it was concluded, that the particle distribution in NC has a major impact on the SC behaviour of the composite. NC with more agglomerations showed more charges in the bulk, due to charge trapping and interfacial polarization.

CHAPTER 7

INDUSTRIAL PROCESSING

What would life be if we had no courage to attempt anything?
-Vincent van Gogh

The introduction of nanotechnology to existing products faces similar problems that often arise with novel technologies. It is only in certain cases feasible to simply introduce a new technology to an existing product and expect an improvement. As an example: if the silica filled epoxy insulation of a cast resin transformer gets replaced by epoxy with nanoscale silica, the price for each transformer would increase drastically. This is due to the fact that the conventional size filler, which is used in large quantities, is cheaper than the base resin itself. Simply replacing microscale filler with nanoscale filler would correspond to a decrease in fillgrade. Therefore the cost would increase twofold: more epoxy is needed to replace the conventional silica, and nanoscale silica is more expensive than microscale silica. The improvement in terms of electrical, mechanical or chemical properties would not justify the steep price tag. Thus, the introduction of nanodielectrics makes most sense if the properties of the NC are considered already at the design stage. One cannot expect nanodielectrics to take the

industry by storm, since NC have to compete with materials which are known as proven technology. This is similar to the problems electric cars face now. They also have to compete with established technology which is considerably cheaper. But also similar to electric cars, NC do already have unique advantages. These advantages make NC interesting for products that reached the limit of what can be achieved by conventional means. At the time of writing industrial application of NC in power engineering is scarce, but e.g. HVDC cables with nanoscale MgO filler are being produced already [46]. For the near future the author expects the following stages of product development:

NMC (within 3 years) - the first stage will most likely see combinations of nano- and micro (or meso) scale filler, where the nanofiller is used to further improve the microcomposite. This has the advantage that it can be introduced relatively easy into an already existing manufacturing process, with only few adaptations.

Tailored materials (within 8 years) - overlapping with the first stage, the years after introduction of NMC will see NC for special applications, where the unique properties NC offer can help working around current limitations.

NC as standard (within 10 to 20 years) - this stage will be reached when nanomaterials get cheaper. Also, manufacturing sites need to be adapted to meet the safety regulations necessary for handling nanoparticles. We will see devices that are designed from scratch, using the possibilities of NC to full extent.

7.1. Upscaling

The procedure as described in Chapter 2 provides reproducible samples with a good dispersion of nanoparticles. But it is challenging to introduce this procedure into running industry processes, for two reasons:

1. The long time the preparation takes.

2. The complexity of the procedure.

Both make it difficult to introduce this process into industry processes, where large amounts of material have to be cast in a relatively short time-span. One way of coping with the problem would be to cut time at the steps that are the most time-consuming. Some ideas to shorten the time needed for the procedure:

- use of a solvent with lower boiling point
- disconnect particle preparation from the rest of the procedure
- preparation of a masterbatch
- use of in-situ particle preparation, like the sol-gel method

7.1.1. Different solvent

One way of improvement would be the use of a solvent with lower boiling point. A list of candidates has been compiled in Table 7.1. Acetone and methanol look promising at first. Acetone has the lowest boiling point of the candidates. The problem is that preliminary experiments that should lead to a good dispersion of nanoparticles in acetone failed. None of the dispersion methods at our disposal (see Appendix A.2.2) could provide a sustainable suspension of dispersed nanoparticles in an acetone solvent. Methanol has a lower boiling point than ethanol and seems to dissolve the agglomerates well. However, methanol is more toxic than ethanol, 10 ml can cause permanent blindness and 30 ml are potentially fatal [108]. Also methanol is too aggressive to use it in the laser diffraction setup (Appendix A.2). Therefore we could not quantify the quality of the particle dispersion. Water and toluene have a higher boiling point than ethanol and are therefore not useful for speeding up this process step. However, they are useful for an alternative particle preparation process, illustrated in Section 7.1.2.

Table 7.1.: Examples for solvents that can be used.

Substance	chemical formula	boiling point in K
Acetone	C_3H_6O	329.68
Ethanol	C_2H_6O	351.55
Methanol	CH_3OH	337.85
Toluene	$C_6H_5CH_3$	383.75
Water	H_2O	373.124

7.1.2. Seperate particle preparation

One way of reducing time for the sample preparation process would be to detach the particle preparation from the rest of the procedure. In this case a larger amount of particles would be functionalized at once, dried, and could be easily stored for further use. The outline of the process can be seen in Figure 7.1. In Figure 7.1(a) the particles are dispersed in a suitable solvent, e.g. water or toluene (Table 7.1). Then a coupling agent is added and the solution gets hydrolized in Figure 7.1(b). Surface functionalized particles become hydrophobic. This leads to clusters of surface functionalized particles, as illustrated in Figure 7.1(c).

The solvent, unreacted silane and particles without functionalization can be filtered out, by using a filter with corresponding grain size. This leaves the agglomeration of functionalized particles in the filter (Figure 7.1(d)). Due to the functionalization it should be possible to disperse the particles easily in a polymer, when mixed with high shear methods. Particles prepared with this method can be stored for longer time and in larger quantities. Problems might occur with any agglomerations prior to hydrolysis. They would be functionalized as a cluster and therefore are very difficult to disperse in the polymer. That would lead to increased agglomerations in the final product. But the main problem is that dry, surface modified nanoparticles need to be evaluated in terms of nanotoxicity (see Appendix C). It will be necessary to provide special storage rooms, suitable for nanotoxic materials.

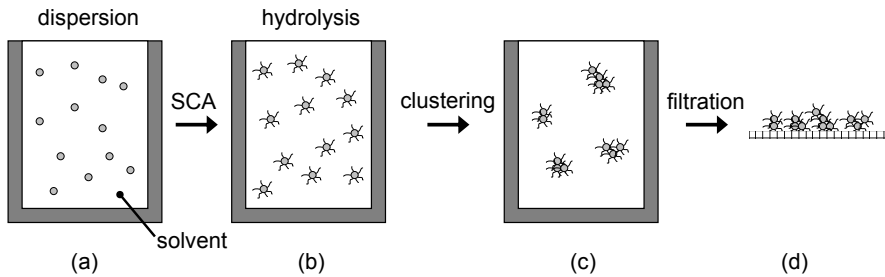


Figure 7.1.: Alternative particle preparation: (a) dispersion of particles in a solvent, e.g. water or toluene; (b) surface functionalization by adding silane; (c) agglomerations of functionalized, hydrophobic particles; (d) filtration

7.1.3. Masterbatch

Alternatively a masterbatch of resin with surface functionalized particles can be created, as illustrated in Figure 7.2. A masterbatch is the concentrated mixture of additives into a carrier polymer during a heating process, which is subsequently cooled down and cut into granular shape. This works best with a base resin which is solid at room temperature. Bisphenol-A resin of the type CY231 would require refrigerated storage units for example. Otherwise the liquid mixture could start to polymerize during storage.

To obtain a polymer with the desired fillgrade, a constituent of the masterbatch needs to be heated up and diluted with neat epoxy. Subsequently it can be mixed with a curing agent, cast and cured like a generic thermoset. There is the risk of introducing impurities during granulation however. This is only a minor issue, compared to troubles that can arise with other methods.

7.1.4. In-situ synthesis

Chapter 2 explains the procedure of ex-situ polymerization. An alternative to this is in-situ polymerization, synthesis of the particles inside the polymer. One example for in-situ polymerization is the sol-gel method uti-

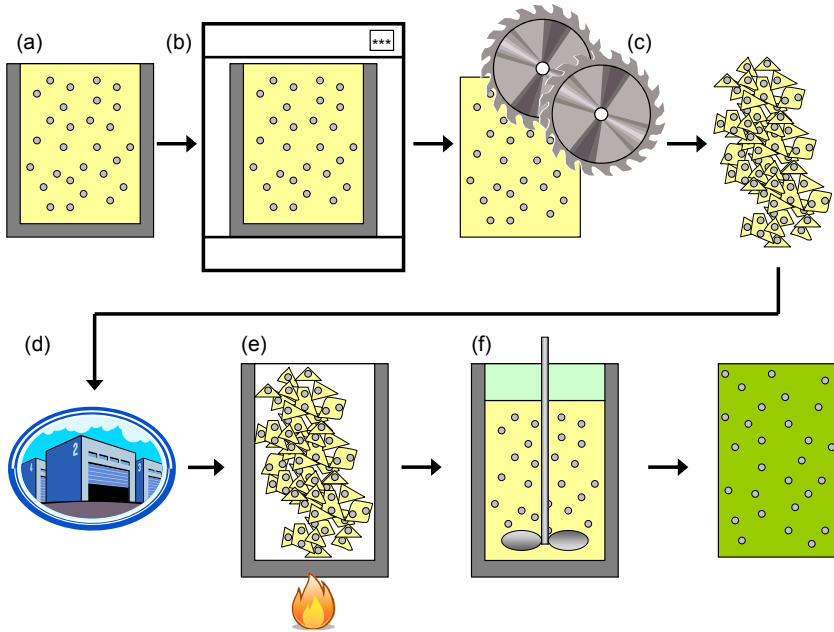


Figure 7.2.: A concentrated mixture of NP in a carrier polymer (a) is cooled down (b) and cut into granular shape (c), which enables long term storage (d). After storage the masterbatch can be used by heating up (e) and diluting with the respective monomer and a constituent amount of curing agent while mixing (f), before casting and curing.

lized by the company NanoresinsTM to create Nanopox[®], the base for the SiO₂-filled NC analyzed in Chapters 4 and 5. Various methods for various materials are known, e.g. montmorillonite (MMT) in PE [109] or barium titanate in epoxy [110].

The problem with this method is that by-products of the synthesis remain in the system. We attribute the increased relative permittivity we measured in Chapter 5 to this. Regardless of how the particles are synthesized, some by-product of the reaction will remain in the final product. Rigorous testing has to show if these by-products impair the dielectric properties. The reduction of treeing resistance witnessed in certain in-situ synthesized composites might be the direct result of such by-products [111].

7.1.5. Dispersion in final products

Industry standards, of which ISO 9000 is the most prominent example, require that the quality of industrial products remains constant throughout production cycles. The introduction of nanoparticles, which by their very nature are elusive to measuring systems, raises the question of how to validate consistent quality. Factors that need to be taken care of include dielectric properties, the average particle size and dispersion. The average particle size should be determined by the supplier, while particle dispersion is rather difficult to quantify. It requires SEM or TEM techniques, which are rather costly and time consuming. However, if all critical factors during particle preparation and mixing are invariable, the particle dispersion has shown to be consistent (Appendix A). Therefore an in-depth investigation with TEM or SEM to validate the quality of particle distribution is only necessary at the beginning of a new process. It only needs to be repeated if there is an indication for changes of the material structure. A good indication for this is the measurement of the relative permittivity, since it has been proven to be susceptible to material changes due to the introduction of nanoparticles (Chapter 5). Therefore regular tests of the permittivity of the material can be used for quality monitoring. Thermogravimetric analysis can be used to monitor the particle concentration and filler weight percentage, making it a valuable complementary monitoring tool (Appendix A.3).

7.2. Possibilities for the near future

7.2.1. Nano-micro composites

NMC are likely candidates of nanodielectrics to be the first to see their widespread use within high voltage and power engineering. Research interest focuses so far on NMC (also called NMMC) based on epoxy with nano- and microscale silicon dioxide [112, 32] or titanium dioxide [55].

One example for in-situ synthesized nanoscale SiO₂ in an epoxy matrix, that can be used in conjunction with microscale fillers is Nanopox®. It is already mentioned in Chapters 2, 4 and 5. It shows increased DC BD strength (see Chapter 4) but has also been shown to be more susceptible to electrical treeing than unfilled epoxy [111].

7.2.2. Field-structured nanocomposites

Aligning of nanoparticles by exploiting the electrorheological effect during curing can lead to anisotropic electroceramic-polymer composites [113]. The frequency-dependent electrorheological effect was discovered in 1949 by Winslow [114]: the application of an electric field leads to a redistribution of particles in a polymer. Depending on the alignment in the direction or perpendicular to the applied field, the composites are called either z-aligned or x-z-aligned.

It has been shown that structuring can enhance the BD strength in polymers along one axis [115]. Thus field-nanostructuring can be used to enhance the BD strength in known weak spots. The relative permittivity can also be altered in one direction, which may provide a platform for materials with higher energy storage density [116].

7.2.3. Nanofluids

The majority of research on nanomaterials in high voltage and power engineering focuses on solid insulation. Not many people are aware of the possibilities nanoparticles can offer in liquid insulation materials. It was already mentioned that transformer-oil based nanoliquids have experimentally shown to have higher positive voltage breakdown levels than conven-

tional transformer oil [59]. Nanoliquids provide interesting new ground for sustainable solutions as well. Ester based insulation liquids have been considered for electrical insulation for decades, but shortcomings compared to conventional transformer oil still prevents widespread application [117]. With the use of nanoparticles it is possible to create alternative insulation fluids, with properties that combine the advantages of ester liquids with those of conventional transformer oil.

CHAPTER 8

CONCLUSIONS

Believe those who are seeking the truth. Doubt those who find it.

-André Gide

An often asked question is, what makes nanocomposites work differently than the insulation material we use today? The short answer to this question is: their surface. As we calculated very small, nanoscale particles possess a much larger relative surface area than conventional, micro-sized particles. For nanocomposites it is vital to utilize this increased surface area by means of surface modification, which makes the nanoscale filler material compatible with the surrounding medium. We have shown that the surface modification by a silane coupling agent leads to an alteration of the surrounding medium. It turns out that this alteration is negligible for micro-scale filler material at low fillgrades, but is significant for nanoscale particles. We have shown that for average particle sizes of less than 25 nm only a small % of filler material is needed to achieve a widespread rearrangement of the host material.

In the course of this research, a manufacturing process for creating

nanocomposites with various filler types was devised. Aluminium oxide, aluminium nitride, magnesium oxide and boron nitride nanoparticles underwent surface modification with a silane coupling agent, before they were introduced into an epoxy resin system. An even distribution of nanoparticles is essential for the composite to be considered a nanomaterial. Various techniques, like transmission electron microscopy and laser diffraction, were utilized to investigate the particle dispersion, thus the quality of the nanocomposite, at every step of the process.

It has been shown how nanoparticles can alter the way the molecular chains of the surrounding polymer are aligned. According to intermolecular forces, these chains form layers that surround the individual nanoparticles. A model has been formulated to describe the morphology of nanocomposites, called *polymer chain alignment model*, or PCAM. Nanocomposites are partitioned into four parts in this model:

Particles - with surface modification

Aligned layer - a rigid inner layer, in which molecular chains are perpendicular to the particle surface due to intermolecular forces

Affected layer - a second layer, which represents the transition between the rigid inner layer and the amorphous host material

Host material - polymer unaffected by the filler material

The PCAM allowed to calculate the distance of a particle to its nearest neighbour in an idealized nanocomposite. The calculated values were compared to data from transmission electron microscopy. Agreement between model and measurement is good for specimens with an even distribution of particles and narrow particle size distribution. With more particle agglomerations and higher variation of the average particle size the deviations between model and measurement increase.

Short term DC breakdown tests have been performed to assess the dielectric strength of nanocomposites. Two observations dominate the DC breakdown behaviour of the investigated materials. The first is that the nanocomposites show their highest breakdown values at the lowest fillgrade (or second lowest fillgrade in case of aluminium nitride particles). Increase

of the fillgrade above 2 % by weight leads to a decrease of the breakdown values. The second observation is that the breakdown values increase for decreasing filler size in case of boron nitride filler material.

The relative permittivity of the manufactured nanocomposites, with fillgrades at and below 10 % by weight, is generally lower than either of the involved materials. This is a direct result of the low permittivity aligned layer around surface modified nanoparticles. The rigid layer has reduced mobility, thus reducing the permittivity of the bulk material due to the large amount of aligned layers within the nanocomposite. The minimum permittivity could usually be measured at a fillgrade of 2 % by weight. Further increase of the fillgrade would increase the permittivity again, since the higher permittivity of the filler material becomes more dominant. The particle size is important for this effect, since the surface area and therefore the volume of the rigid layers increase with decreasing particle size.

Space charge behaviour, which is important for the design and operation of high voltage DC equipment, was investigated with the pulsed electroacoustic method. It has been observed, that the filler dispersion has an impact on the space charge dynamics. In nanocomposites with an even dispersion the space charge density is reduced, compared to the unfilled polymer. However, as agglomerations increase, a higher charge intake is the consequence. The only exception are magnesium oxide nanocomposites, which show reduced space charges regardless of the dispersion quality. This is explained by the agglomerates acting as charge traps. Large agglomerates can also lead to increased interfacial polarization.

The PCAM suggests that the distribution of nanoparticles is important for the dielectric properties. Increased particle agglomeration can lead to field enhancements and act as charge traps. It also predicts the real part of the complex permittivity to be influenced by the rigid aligned layers, which reduce the bulk permittivity. This has been confirmed by the measurements mentioned above.

Finally an outlook was given on the possibilities of introducing nanodielectrics into industrial processes in the near future. These possibilities include polymer based nano-micro-composites, anisotropic electroceramic polymer composites and nanofluids. The latter can be based on either conventional transformer oil or ester based insulation liquids. Nano-

micro-composites are likely candidates to be the first nanodielectrics in widespread use in electrical engineering, because they have the potential to combine advantages of nanomaterials with those of well known materials with microscale filler.

CHAPTER 9

RECOMMENDATIONS

I may not have gone where I intended to go, but I think I have ended up where I intended to be.

-Douglas Adams

The BD tests that have been conducted as part of this thesis are short term values. For practical applications the long term and ageing behaviours are of vital importance. Therefore a series of ageing tests would be an appropriate continuation of this work.

Tests on samples with BN filler showed a logarithmic correlation between relative permittivity and filler size. In order to determine how the parameters A and B of this function are affected by other particle properties, more measurements are needed with different filler materials of various particle size with an aspect ratio close to 1.

Epoxy solely filled with nanoparticles is too expensive for a lot of industrial applications. NMC with microsized silica filler in combination with a nanoscale filler is a feasible way of introducing NC into the manufacturing stage. Thus an evaluation of the dielectric properties of NMC is an interesting prospect. Due to their impact on the space charge behaviour, MgO

nanoparticles would be a suitable candidate for the nanophase of NMC.

Particles are so far randomly distributed and spherical or almost spherical. In order to achieve the long term goal of tailored nanomaterials, two things would be important: an investigation of the impact of the filler aspect ratio and of the alignment of particles on the dielectric properties.

APPENDIX A

SPECIMEN CHARACTERIZATION

Creating NC is a complex task, as elaborated in Chapter 2. Sophisticated characterization techniques are needed, to validate that the investigated specimens are indeed NC. The morphology of the particles was analyzed by means of X-ray diffraction. Laser diffraction was used for determining if ethanol is an adequate solvent for the NP we intended to use. It was also used to investigate which mixing method works best for dispersing the particles in a solvent. Thermogravimetric analysis was used to investigate the surface functionalization and the particle concentration in different parts of the sample. Electron microscopy was used to determine the particle distribution and average particle size.

A.1. X-ray Diffraction

The morphology of the particles was investigated with X-ray diffraction (XRD). The intensity I of an X-ray beam gets reduced as it passes through a material. The decrease is proportional to the distance traversed by the beam x , as shown in Equation A.1, where μ represents the linear absorption coefficient. Integration of Equation A.1 gives Equation A.2, where I_0

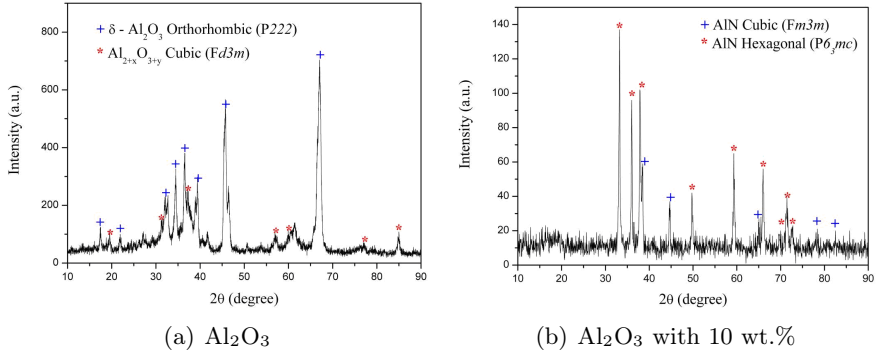


Figure A.1.: XRD spectra of Al₂O₃ A.1(a) and AlN A.1(b) particles.

is the intensity of the incident beam and I_x the intensity after the distance x within the material. This Equation is often written in form of A.3, where ρ is the density of the material and μ/ρ the mass absorption coefficient. XRD patterns of as-received powders were obtained at ambient temperature using a Bruker-AXS D8 advance diffractometer. The 2θ ranges of the data were from 10° to 90° with an increment of 0.02° . Examples are shown in Figures A.1(a) and A.1(b) for Al₂O₃ and AlN respectively. The spectra obtained with XRD can be compared to reference spectra to identify the lattice structure. By means of XRD we identified the crystal lattice structure of all particle types we used, as compiled in Table 2.1 on page 17.

$$-\frac{dI}{I} = \mu dx \quad (\text{A.1})$$

$$I_x = I_0 \cdot e^{-\mu x} \quad (\text{A.2})$$

$$I_x = I_0 \cdot e^{-\rho \frac{\mu}{\rho} x} \quad (\text{A.3})$$

A.2. Laser Diffraction

Laser Diffraction (LAD) is a widely applied particle sizing technique. It uses angular light scattering to determine the particle size distribution. LAD has a broad measuring range and a high resolution (particle diameter range 0.04 - 2000 μm). Dry samples have to be dispersed in water, ethanol, cyclohexane or air. The result from the laser diffraction comes in form of a size distribution and has to be calculated via different mathematical models from the raw measurement data. It is intended for characterization of spherical or almost spherical particles. Therefore measurement on non-spherical particles leads to larger error margins. The instrument we used is the Coulter LS 230.

A.2.1. Sample preparation

For each measurement 0.2 g of Al_2O_3 particles were dispersed in 10 g of ethanol or demineralized water. The particles in water were mixed by hand for some seconds and an anionic dispersant (sodium-diphosphate ($\text{Na}_4\text{P}_2\text{O}_7$)) was added to reduce the surface tension of the particles, thus keeping the solution stable. In ethanol the particles were dispersed in various ways:

- Ultrasonic bath for 30, 60 and 120 minutes
- Ultrasonic probe for 5 minutes
- Ultrathurrax for 8 minutes
- Mixing by hand

A.2.2. Results

Figure A.2 shows the particle distribution of Al_2O_3 in water compared to ethanol without mixing. About 95 % (wt.) of the particles are smaller than 350 nm in water, with an average particle size of 141 nm. In ethanol only 5 % (wt.) of the agglomerates are smaller than 1 micron, while 95 % are larger. Most agglomerates of particles are approximately 15 μm . Therefore

it is needed to disperse the particles by mechanical means. Figure A.3 shows the particle dispersion in ethanol for different methods of dispersion.

Surprisingly, the ultrasonic bath shows to be the best method for particle dispersion, as can be seen in Figure A.3. After 30 minutes in the ultrasonic bath about 90 % (wt.) of the particles are below 350 nm, with an average size of 141 nm, similar to the results of water. After 60 minutes almost all agglomerates are well dispersed, as can be seen in figure A.4.

The ultrasonic probe is the dispersing method with the highest energy density in this series of measurement. Drawback of this method is that the full power of the probe can only be applied for a relatively short time. When applied longer than 10 minutes, the suspension started to boil. The size distribution is worse than with the ultrasonic bath: only 30 % of the particles were below 0.6 μm . Interesting are the two peaks above 0.6 μm , which indicate that the ultrasonic probe does not simply dissolve the particles, but also encourages agglomerations of specific sizes. Use of the ultraturrax high shear mixer results in a distribution which is marginally better than without mixing, but inferior to the ultrasonic probe. Only 15 % (wt.) of the agglomerates are below 1 micron in size.

Additional tests have been made on Al_2O_3 treated with EPPS, in order to see if the ethanol- Al_2O_3 -suspension is stable and can be stored for longer periods of time. As shown in Figure A.5, the particles showed a good dispersion in ethanol after 5 days, for both treated and untreated Al_2O_3 . Since there was no reagglomeration in either sample, we can assume that the suspension is stable. And even if there would be some agglomeration after months of storage, this problem can be easily solved by ultrasonic treatment.

A.2.3. Summary

Analyzing the size distribution by means of laser diffraction showed that water with sodium-diphosphate would be the best solvent for nanoscale Al_2O_3 . However, due to the higher boiling point it is not the best candidate for the synthesis method described in Chapter 2. If the process temperature is too high during the stage of the solvent evaporation, monopolymerization of the resin can occur. Ethanol is preferred due to its lower boiling

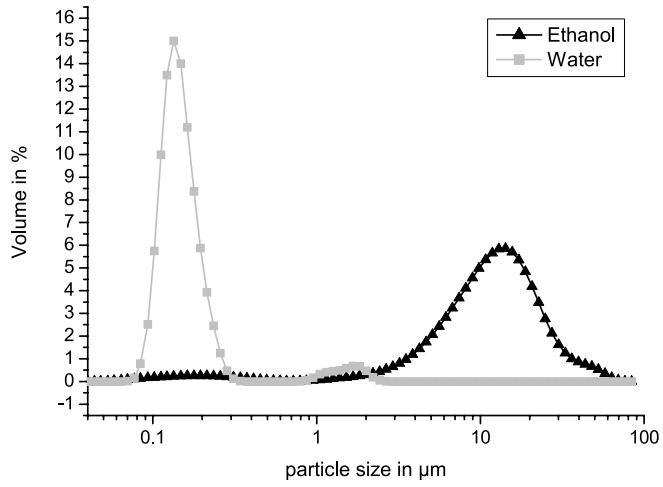


Figure A.2.: Comparison of the Al_2O_3 dispersion in water and ethanol.

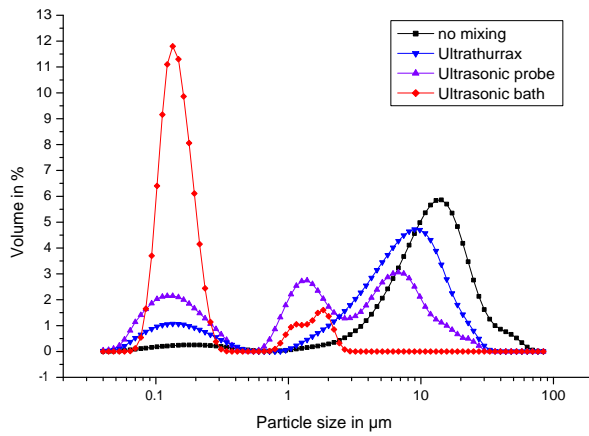


Figure A.3.: Influence of the mixing method Al_2O_3 in ethanol.

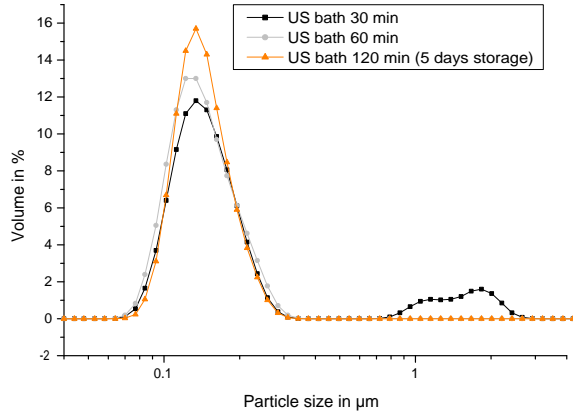


Figure A.4.: Influence of the application time of the ultrasonic bath on the Al_2O_3 dispersion in ethanol.

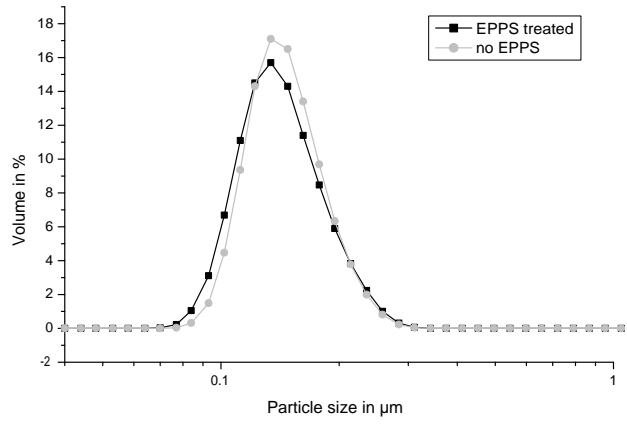


Figure A.5.: Influence of the silane treatment on the Al_2O_3 dispersion in ethanol after 5 days of storage.

point, but needs a suitable dispersion method, since most particles form agglomerates of approximately 15 μm . The best method for dispersion is the use of an ultrasonic bath for sufficient time, typically 60 minutes. Ultrasonic probe and high shear mixing proved to be inefficient methods for breaking up agglomerations of NP. With the probe we also witnessed that the solution started to boil after approximately 10 minutes, which prevents long mixing times.

After five days of storage no significant re-agglomeration could be measured, which showcases the stability of the Al_2O_3 -ethanol-suspension. LAD results after five days were identical to those taken directly after dispersing the particles.

A.3. Thermogravimetric Analysis

A.3.1. Validation of the surface functionalization

With laser diffraction it was not possible to determine if the silane treatment was successful, since EPPS is too small compared to the Al_2O_3 -particles. The additional layer on the particle surfaces is not visible due to the measurement inaccuracy. Surface treatments did also not cause any observable difference in TEM micrographs. Therefore we utilized TGA for validation of the surface functionalization.

The thermal degradation behaviour of EPPS for treated and untreated nanoalumina particles was characterized. The idea was to see if EPPS is present at the surface of the alumina particles. Measurement was done in both air and nitrogen gas (N_2) atmosphere, with a heating rate of 10 K/min. Figure A.6 shows the effect of the SCA treatment on the degradation behaviour of alumina nanoparticles in air, Figure A.7 in a N_2 atmosphere.

Aluminum oxide is a very dense and stable material. There is no weight change up to 470 K. The SCA attached to the particle surface has an organic chain, which degrades at elevated temperatures. This leads to a weight loss, which could be observed at treated particles: modified alumina particles have a much higher weight loss than untreated ones. TGA analysis therefore indicates that the silane coupling agent was successfully

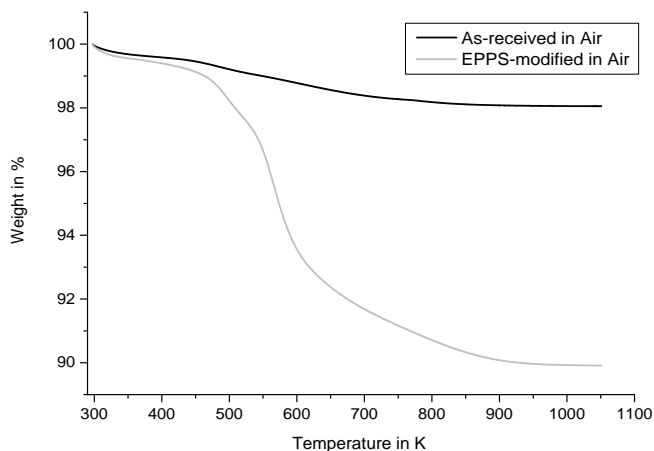


Figure A.6.: TGA analysis on Al_2O_3 samples with and without surface functionalization. It shows a much higher weight loss for treated particles, indicating successful surface functionalization.

grafted on the alumina nanoparticles surface.

Another indication for the presence of EPPS on the surface of nanoalumina can be seen in the graphs that depict the existence of individual elements inside the composite. In Figure A.12(a) on page 140 it can be seen that Si, the basis of our coupling agent, is present and dispersed throughout the material. These results were obtained using SEM analysis with EDS (see Section A.4.2).

A.3.2. Particle concentration profile

In early experiments there were problems with sedimentation of particles and particle agglomerations on the bottom of the samples due to gravitational settling. To investigate if sedimentation is a problem with the synthesis method, a cylindrical sample was cast. Three parts were cut out from the top, bottom and centre of the sample. These specimen underwent thermogravimetric analysis (TGA) with a TGA 7 Thermogravimetric An-

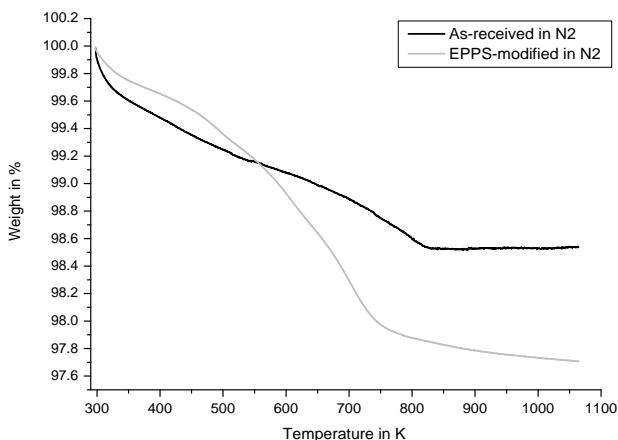


Figure A.7.: TGA analysis on Al_2O_3 samples with and without surface functionalization. It shows a much higher weight loss for treated particles, indicating successful surface functionalization.

alyzer by Perkin Elmer. In the course of the TGA analysis the organic part of the sample is incinerated. The weight of the remaining inorganic particles can be determined. In case of gravitational settling of the nanoparticles on the bottom, we should observe the majority of alumina there and only a small amount on the top of the sample. But as shown in Figure A.8, results for the three parts of the sample did not differ significantly.

A.4. Electron Microscopy

Normal visual light has a wavelength of 4000 Angstroms (\AA). Therefore, investigating an object smaller than $0.4 \mu\text{m}$ is not possible with conventional optical microscopy. The typical wavelength of an electron beam is about 1\AA .

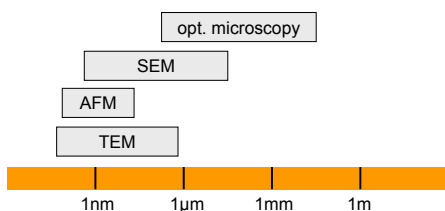


Figure A.9.: Overview of usability of different types of microscopy.

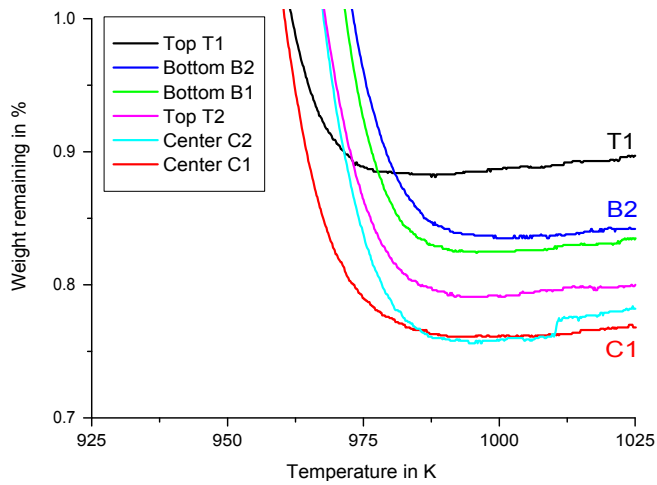


Figure A.8.: TGA analysis on Al_2O_3 -epoxy sample with 0.5% per weight. It shows that the amount of particles in top, centre and bottom of the sample does not change significantly, hence the sedimentation encountered in the composite is negligible.

When the light source is changed into an electron gun, the wavelength becomes 100.000 times smaller. Therefore the smallest detectable object is much smaller compared to an optical microscope, as illustrated in Figure A.9. We utilized transmission electron microscopy (TEM) and scanning electron microscopy (SEM) for characterizing our NC.

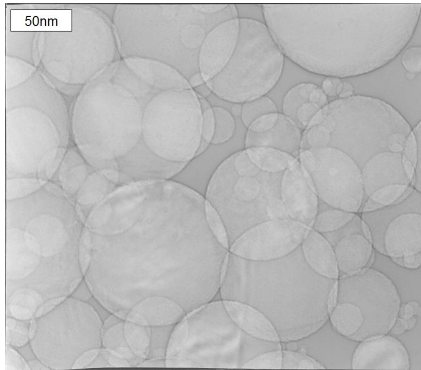
A.4.1. TEM Analysis of NC

Particles

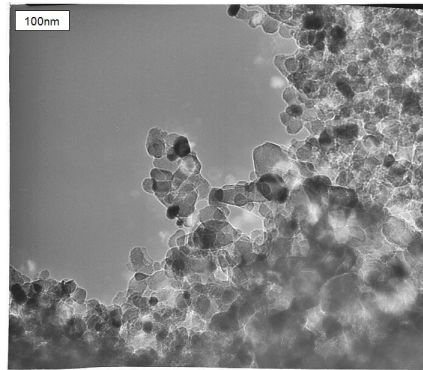
TEM allows us to view at the individual particles in an ethanol suspension, as shown in Figure A.10. Obtained particle properties are compiled in Table A.1. The micrograph of Al_2O_3 (figure A.10(a)) shows the shape of the crystalline particles being spherical. An average diameter of 25 nm could be calculated with particle sizes ranging from 10 to 200 nm. MgO particles show a very narrow size distribution with an average of 22 nm (figure A.10(b)). The crystalline particles have spherical, egg and truncated cubic shapes. AlN particles are also crystalline, with spherical, hexagonal and cubic structures as shown in figure A.10(c). An average diameter of 60 nm was calculated, with a better size distribution than Al_2O_3 . BN particles are amorphous with spherical and truncated cubic shapes. They have particle sizes between 4 and 32 nm with 20 nm on average. BN particles of the first batch exhibited a layered crystalline shell (8-10 layers) of 2.5-3 nm thickness (Figure A.10(d)), which corresponds to boron oxide (B_2O_3). These BN particles caused severe difficulties when trying to disperse them in a solvent. Later batches of BN were crystalline and hexagonal, with an average diameter of 70 nm. These particles were easier to disperse and did not exhibit a thick B_2O_3 shell.

Nanocomposites

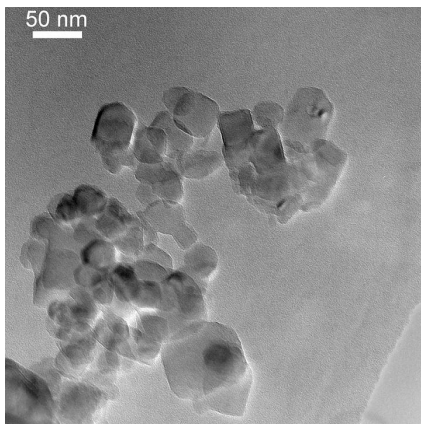
For TEM micrographs of NC, thin films of 20 to 40 nm thickness were cut out from the bulk material of the respective specimen by means of a diamond saw.



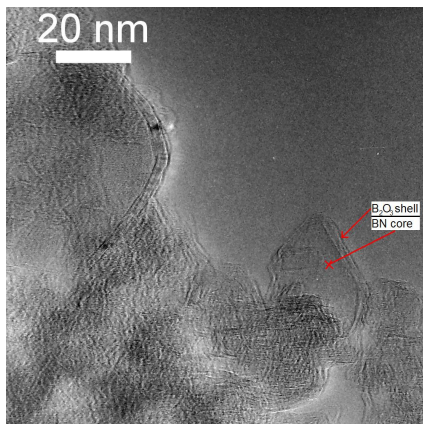
(a) Al₂O₃ particles.



(b) MgO particles.



(c) AlN particles.

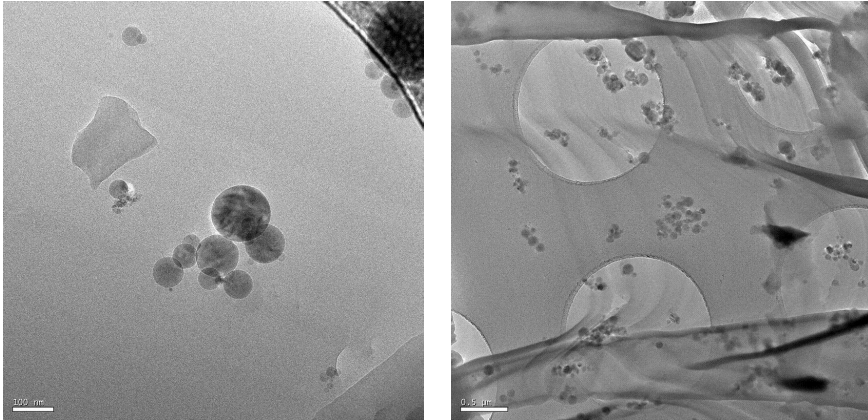


(d) BN particles.

Figure A.10.: TEM micrograph of various nanoparticles: Al₂O₃ A.10(a), MgO A.10(b), AlN A.10(c) and BN A.10(d).

Table A.1.: Particle properties as indicated by TEM analysis

Type	Average diameter	Shape	Structure
AlN	60 nm	spherical, hexagonal, cubic	crystalline
Al ₂ O ₃	25 nm	spherical	crystalline
BN (B ₂ O ₃)	20 nm	spherical, truncated cubes	amorphous
BN	70 nm	hexagonal	crystalline
BN	500 nm	platelets	crystalline
BN	1.5 μ m	spherical	crystalline
BN	5 μ m	spherical	crystalline
MgO	22 nm	spheres, eggs, truncated cubes	crystalline
SiO ₂	20 nm	spheres	crystalline



(a) TEM micrograph of 2 wt.% Al₂O₃ particles in an epoxy film. (b) TEM micrograph of 5 wt.% Al₂O₃ particles in an epoxy film.

Figure A.11.: TEM micrograph of Al₂O₃-ER NC.

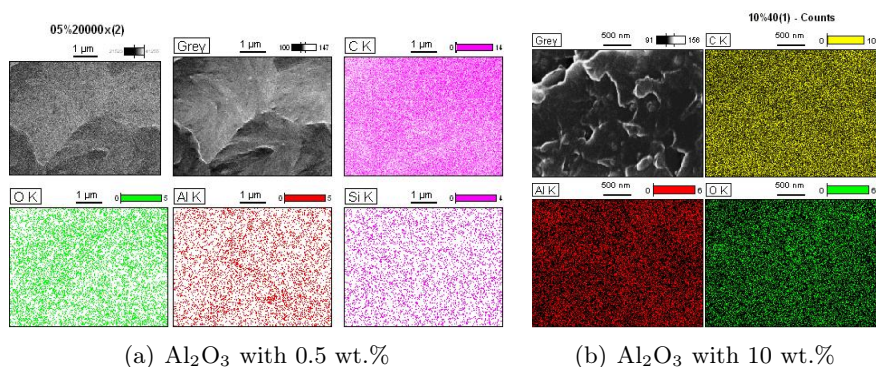


Figure A.12.: SEM micrographs of Al₂O₃-ER with 0.5% A.12(a) and 10% A.12(b) per weight with 20.000 times magnification. Quantitative analysis of the components of our sample shows Al well dispersed in the epoxy.

In Figure 2.6 (page 26) an Al₂O₃-ER composite with a fillgrade of 2 wt.% can be seen. It shows that small clusters of particles are evenly dispersed throughout the material. Given that the dispersion is similar in all three dimensions, we can assume from the TEM results that samples with 2 wt.% Al₂O₃ have good dispersion of nanoparticles. Figure A.11(a) shows a close-up of an agglomerate. The large circles that can be seen in the micrographs are from a carbon mesh of the sample holder in the background and not part of the specimen.

Figures 2.7 (page 27) and A.11(b) (page 139) show the dispersion of Al₂O₃ for 5 wt.%. There are some larger agglomerates compared to 2 wt.%, but the overall distribution of particles is good, since most particles and agglomerates are below 100 nm.

A.4.2. Quantitative Analysis of NC with SEM

When a specimen surface is irradiated by an electron beam, interaction between the electron beam and the atoms composing the specimen produce various kind of information. The electrons generated by the electron gun are accelerated and irradiate the sample. The electron has a kinetic

energy proportional to the accelerating voltage. The kinetic energy dissipating within the sample generates characteristic X-ray-signals from the specimen. These characteristic X-ray generated by irradiating the specimen can be analyzed twofold:

qualitative analysis where the elements that constitute the specimen are identified

quantitative analysis a calculation of their weight concentrations

We used SEM to make a quantitative analysis of our specimen, to investigate if the samples have the desired weight percentage of nanofiller and their distribution. This analysis indicates good dispersion of nano-alumina for surface functionalized particles, as can be seen in figure A.12. Comparing Figures A.12(a) and A.12(b), for 0.5 and 10 wt.% respectively, it is apparent that the density of Al_2O_3 Al-atoms (and therefore Al_2O_3 particles) is increasing with the fillgrade. Also we noticed that the quality of the dispersion is fluctuating with the fillgrade. Samples with 2 wt.% show the best dispersion, while 0.5 % and 10 % show the worst. Relatively large clusters and agglomerates can be found in samples with 0.5 wt. The reason for this is that with larger filler content the mixing gets more effective, since there are more particles who shear along each other. Therefore the particles get spread out more evenly than in samples with low filler content, where only very few particles are involved. With fillgrades of 5 wt.% and higher on the other hand, there might be too many nanoparticles in the system, which leads to a state where agglomerates are difficult to avoid. Figure A.12(a) also shows that Si is dispersed evenly throughout our NC. Si is the basis of our coupling agent and indicates that the surface modification with EPPS was successful.

A.4.3. Summary

Investigation with TEM and SEM revealed the particle dispersion, average particle size and what elements are present in our NC. The quality of the particle dispersion varied in our NC, depending on the fillgrade:

- Particle dispersion is the best in samples with 2 wt.%

- Particle dispersion in samples with 0.5 wt.% is not ideal, due to the fact that there are not enough particles to shear among each other during mixing
- The quality of dispersion degrades for higher fillgrades, due to the fact that there are too many particles and agglomerations are difficult to be avoided

Average particle sizes have been identified for Al₂O₃ (25 nm), AlN (60 nm), BN (20 nm first batch, 70 nm second batch), MgO (22 nm) and SiO₂ (20 nm). Apart from the first batch of BN all particles were crystalline.

Quantitative analysis with SEM confirms TGA measurements about surface modification. An even dispersion of Si, basis of the coupling agent used, could be found in each NC.

A.5. Dynamic Mechanical Thermal Analysis

Due to DC conductivity above the glass transition temperature T_g , it is difficult to determine the location of the α -relaxation with dielectric spectroscopy. To verify the location of the α -relaxation and T_g , dynamic mechanical and thermal analysis (DMTA) in form of a three-point bending test was utilized. The dynamic Young's modulus E^* was measured at 1 Hz for temperatures between 300 and 460 K, with a rate of rise of 2 K per minute. Figure A.13 shows the dynamic loss modulus E'' for unfilled epoxy (Equation A.4). The maximum of E'' , hence the T_g , lies between 380 and 390 K, depending on curing time and temperature.

$$E^* = E' + j \cdot E'' \quad (\text{A.4})$$

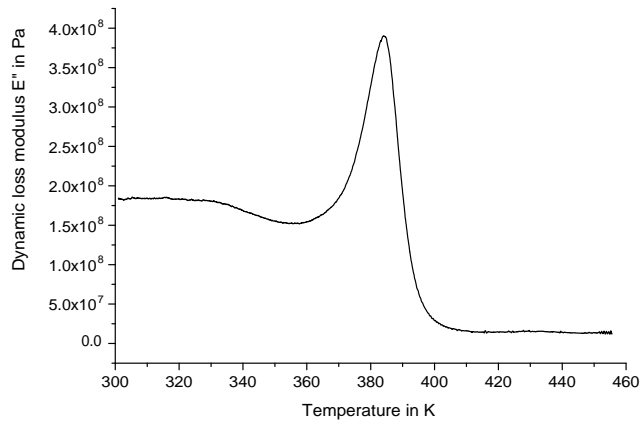


Figure A.13.: Dynamic loss modulus E'' for unfilled epoxy (18 hours curing at 413 K) acquired with DMTA at 1 Hz.

APPENDIX B

EXPERIMENTAL SETUP

B.1. Dielectric Spectroscopy

Broadband dielectric spectroscopy (DS) is a powerful tool to investigate the dielectric response of insulating materials as a function of frequency.

B.1.1. Measurement principle

The measuring principle bases on the interaction of an external field with the electric dipole moment of the sample, which is often expressed by permittivity. Simply said a voltage of variable frequency is applied to a sample and the magnitude and phase of the current flowing through the sample are measured.

B.1.2. Measurement setup

At Delft University of Technology we use a fully automated measurement cell from Novocontrol, which allows us to measure the dielectric properties (i.e. conductivity, permittivity or $\tan(\delta)$) continuously as a function of frequency and temperature. The equivalent circuit diagram can be seen in

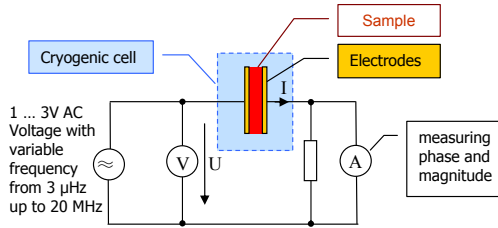


Figure B.1.: Equivalent circuit diagram of the DS setup.

Figure B.1. The sample lies within a cryogenic cell, which can be heated up to 673 K and cooled down to 113 K with 0.01 K temperature stability.

Usually we are interested in the complex permittivity ϵ^* (see equation B.1) of the material, which relates to a material's ability to transmit or permit the electric field.

$$\epsilon^* = \epsilon' - j\epsilon'' \quad (\text{B.1})$$

The real part of the complex permittivity is what we know as *relative permittivity*, it is a measure of the amount of polarization. The imaginary part is a measure of the losses involved in the polarization processes. The behaviour of the permittivity as a function of frequency and temperature is sensitive to material changes, such as caused by ageing processes or by the addition of fillers. The complex permittivity is related to the dielectric loss factor ($\tan(\delta)$), according to Equation 5.2 on page 72.

The polarization spectrum

Even though the DS generally yields complex dielectric relaxation spectra, the data analysis and discussion of the dielectric properties is often based on the dielectric loss spectra ϵ'' . This has two reasons:

- Dielectric dispersion curves show often more details and make visual evaluation easier. Every time ϵ' varies rapidly - at the resonance frequency - a peak can be seen in the ϵ'' curve for example.

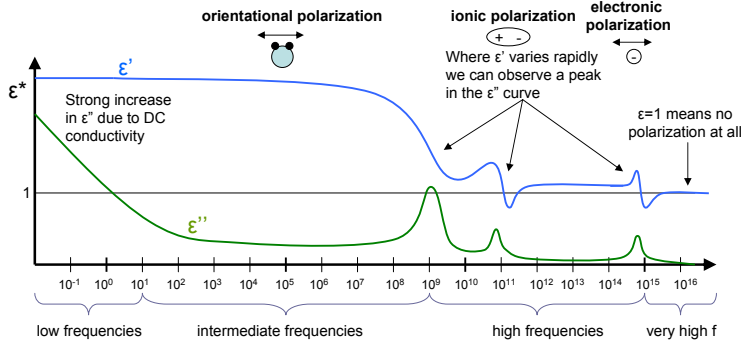


Figure B.2.: The polarisation spectrum with orientational, ionic and electronic polarisation mechanism.

- Real and imaginary part of ε are interrelated by the Kramers-Kronig relations (Equation B.2), hence the two spectra are fully equivalent in terms of information about relaxation processes.

$$\varepsilon''(\omega_0) = \frac{\sigma_{dc}}{\varepsilon_0 \omega_0} + \frac{2}{\pi} \int_0^{\infty} \varepsilon'(\omega) \frac{\omega_0}{\omega^2 - \omega_0^2} d\omega \quad (\text{B.2})$$

The frequency dependent polarization spectrum of a dielectric is the superposition of all active polarization mechanisms (see figure B.2):

- For very high (i.e. optical) frequencies even electrons cannot keep up with the changing field, the result is a relative permittivity equal to 1 with no measurable losses.
- At high frequencies (IR, UV) electronic and ionic polarization shows up. In most applications we stay well below these frequencies.
- At intermediate frequencies (1 Hz to 100 MHz) orientational polarization is dominating. In this frequency range, molecules, parts of molecules or molecular chains orient in the changing electrical field. In this region changes in the material composition can be seen, for example because of the introduction of filler materials.

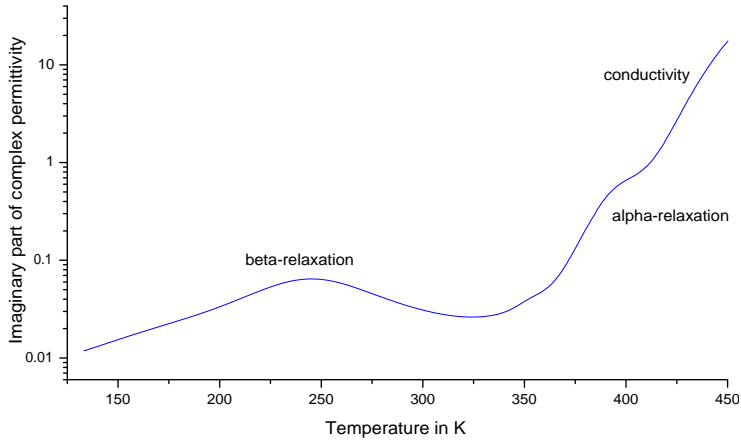


Figure B.3.: The polarisation spectrum as function of temperature with DC conductivity, α - and β -relaxation.

- At low frequencies two additional mechanisms become visible:
 1. Interfacial polarization - the polarization of interfaces between materials, with a relaxation time in the range of seconds to hours.
 2. DC conductivity - which gives rise to ohmic losses, that show up in a linear reciprocal relation between ε'' and the frequency. This is especially visible at higher temperature, when the conductivity strongly increases.

The polarization spectrum can also be investigated as function of temperature. This is useful for identification of α - and β -relaxation peaks, as shown in Figure B.3. However, the α -relaxation can be overshadowed by the DC conductivity and is especially at lower frequencies difficult to determine.

B.1.3. Sample Preparation

It is recommended to deposit electrodes (e.g. Al, Ag or Au) on the sample surface for an improved interface between measurement setup and sample. This improves the measurement accuracy, since the surfaces of both electrodes and samples are not perfectly even and the electrode makes sure the specimen surface is on equal potential [97].

B.2. Space Charge Measurement

For high voltage DC applications, the consideration of space charge (SC) phenomena is of crucial importance. Accumulation of charges in an insulation system changes the field distribution from Laplacian (Equation B.3) to Poissonian (Equation B.4). This results in local field enhancements, which can subsequently result in a dielectric breakdown. In case of polarity reversal this effect is of utmost importance, since the field generated by the space charges adds up to the applied field [83].

$$\frac{dE(x)}{dx} = 0 \quad (\text{B.3})$$

$$\frac{dE(x)}{dx} = \frac{\rho(x)}{\varepsilon_0\varepsilon_r} \quad (\text{B.4})$$

Space charge measurements provide the electric field distribution inside the insulating material. They can also give an indication of the ageing state of the insulation. If the space charge distribution ρ is known, the electrical field can be calculated using Equation B.4.

Reasons for SC are manifold. The conductivity σ of most materials depends on the temperature and the electric field. Thus a temperature gradient results in SC accumulation, consequently influencing the electric field distribution. Crystalline and amorphous regions of the same material have different conductivities and permittivities. Since an insulation material is never perfectly homogeneous, these inhomogeneities can lead to a distortion of the electric field. SC also accumulates at interfaces,

both insulator-insulator and insulator-electrode interfaces. In general everything that leads to a distortion of the electric field because of a change in conductivity also leads to SC. Therefore SC will accumulate in insulation stressed with HVDC voltage, which will contribute to the electric field, since there are always conditions that lead to conductivity changes in practice.

In case of insulator-electrode interfaces the terms homocharge and heterocharge are commonly used (see Figure B.6). Description of these types of charge can be found on page 156.

B.2.1. Measurement principle

Early SC measurement consisted of cutting an insulating material in slices and measuring the charge on each slice. But this destructive method is outdated for a long time, modern SC measurement setups are generally less destructive for the specimens. Commonly used methods can be divided in three groups according to their excitation method:

Electric electron beam method (EBM), pulsed electro acoustic method (PEA)

Pressure laser induced pressure propagation (LIPP), piezoelectric induced pressure wave propagation (PIPWP), pressure wave propagation (PWP)

Temperature laser intensity modulation (LIM), thermal pulse method (TPM), thermal step method (TSM)

Methods using acoustic waves were favoured over those exploiting thermal waves, since the need for numerical signal processing to retrieve the SC distribution is much higher for the latter. PEA was eventually favoured over laser induced acoustic methods since the reproducibility is higher. Laser induced methods use the electrode material as laser target, consuming it in the process. Another advantage of PEA is that the electrical activation circuit is decoupled from the measuring circuit. Thus a sample breakdown does not necessarily damage the measurement setup.

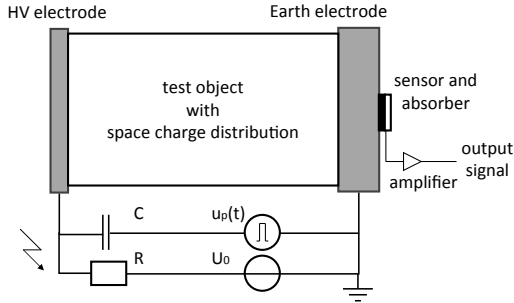


Figure B.4.: Equivalent circuit diagram of the sample configuration and test setup for space charge measurements with the PEA method.

B.2.2. PEA Setup

In this work, the pulsed electro acoustic (PEA) method was used for measuring the dynamic space charge distribution in flat, solid insulators [118, 105]. An equivalent circuit diagram is shown in Figure B.4, properties are compiled in Table B.1, elaborate description can be found in [106]. An external electric pulse $u_p(t)$ is applied to the sample. In case SC are present, this pulse induces a perturbation force on each charge. Due to this force the charges move slightly, consequently launching an acoustic wave, which is proportional to the charge distribution in the sample. The acoustic wave can then be detected and subsequently transformed into an electric signal by means of a piezoelectric transducer.

The piezoelectric sensor usually consists of polyvinylidene fluoride (PVDF) or lithium niobate (LiNbO_3). An acoustic termination is required to avoid reflections of the acoustic waves. A material with the same acoustic properties as the sensor is used for this purpose in combination with a material which is able to dampen (absorb) the acoustic waves. The pulse can be superimposed to an applied DC voltage U_0 . In this case a decoupling capacitor C and a resistor R have to be placed in series to the pulse and DC source respectively, as indicated in Figure B.4. Typical pulse values used in this thesis are 600 V for the amplitude with a pulse width of 20 ns.

However, the detected signal does not represent the acoustic signal at

Table B.1.: Properties of the PEA setups used in this work.

Insulation material	Epoxy
HV electrode diameter in mm	14.5
Maximum voltage in kV	20
Pulse source	Discharge cable generator
Switching element	Solid-state switch
Rise time in ns	4
Pulse width in ns	10 or 20
Spacial resolution for epoxy	25 μm or 53 μm
Sensor	PVDF- β foil (9 μm)
Amplifier	Two 23dB Amp each
Temperature range	290 K to 343 K

the sensor, since the sensor-amplifier system acts as high pass filter. Deconvolution techniques are used in this work to take this into account.

Sample preparation

Diameter of the samples used was 50 mm. Starting with 13 kV we witnessed that the relatively low surface resistivity of some samples lead to surface flashovers. Flashover could be prevented by increasing the creepage length. This was done by using a rubber sheet with larger diameter. This sheet was covering the sample plus large parts of the sample holder, with the exception of the area below the HV electrode, which was connected to the sample via a semiconductive layer. The latter also acts as acoustic dampening.

Measurement procedure

The measurement process can be divided in four stages:

- Calibration
- Poling
- Depoling
- Signal processing

Calibration and the actual measurement are sometimes done on different samples. This is only necessary for samples with a high SC intake and shall ensure that no charge package leftover from the calibration process can distort the measurement data. This was not necessary in our case.

Poling is the application of the electric field on the sample. The voltage was applied for typically 1 hour, or until a steady state was reached, and the SC profile was saved. The voltage is subsequently switched off and the depoling process starts. Since interfacial polarization is usually a dominating factor during poling, SC in the bulk of the material can best be seen during the depoling stage. This stage lasts until all SC have disappeared, with most samples tested being free of SC after approximately 1 hour.

The electrical signal received from the measurement setup is not a precise representation of the SC profile. Three effects have to be taken into consideration [106]:

1. The RC filter (see Figure B.4) distorting the pressure signal
2. The conversion via PVDF foil is frequency dependent
3. Any charge with a width smaller than the spatial resolution s (Equation 6.1 on page 94) is still measured as a charge packet with a width of s

These effects combined are called the system response H . Post processing with MATLAB was done to correct the measured signal, the program did the following:

- Subtraction of the noise
- Deconvolution
- Correction of the attenuation
- Two integration steps to calculate the electric field and potential distribution

B.2.3. Evaluation of Space Charge Evolution

After signal processing the obtained SC profiles need to be analyzed. Various evaluation parameters can help doing so and are outlined below. A more detailed description of the evaluation parameters can be found in [119] and [106].

Field Enhancement factor F_E and location of the maximum field x_{F_E}

Jeroense introduced the field enhancement factor F_E as in equation B.5, where E_{max} is the maximum field strength in the sample, U is the external DC voltage and d the sample thickness [106]. Since SC phenomena are time dependant, F_E is a function of time. In this thesis we usually look at the static field enhancement factor, where the SC have reached their steady state. This represents the worst case scenario for the insulating material.

$$F_E = \frac{E_{max} - \frac{U_{DC}}{d}}{\frac{U_{DC}}{d}} \quad (\text{B.5})$$

For an application not only the magnitude of the field enhancement is important, but also it's location x_{F_E} . In solid materials it is generally favoured to see the maximum field enhancement in the bulk of the material instead of the interfaces.

Space Charge Profile

In a homogeneous sample space charges form at the interface at first, due to the injection and extraction of charges. In time the charges spread out into the bulk of the insulating material. The shape depends on the type of charge: usually homo- or heterocharge (see below). Figure B.5 shows a typical space charge profile that can be retrieved after 1 hour of poling.

Average Space Charge

Apart from identifying isolated charge packages, the average amount of space charges Q_{av} can be calculated. In order to calculate this value, the absolute charge value over the sample thickness v has to be integrated first.

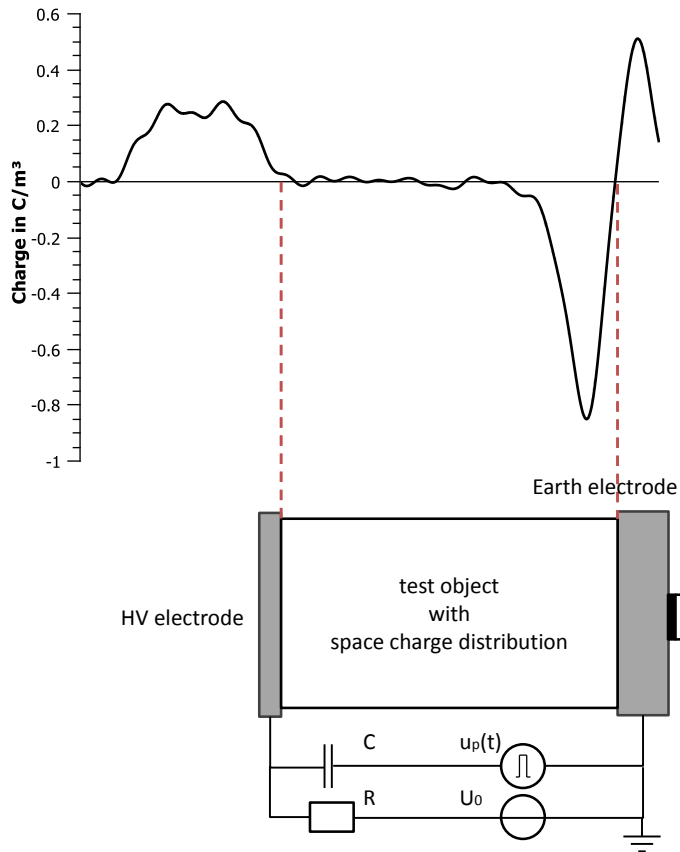


Figure B.5.: Typical space charge profile of neat epoxy. The Y-axis shows the amount of space charge, the X-axis represents the location of the charge. On the left border of the graph the interface between high voltage electrode and sample can be seen. On the right side is the interface between ground electrode and sample. In this case we have heterocharge at the ground electrode.

Subsequently this value is divided by the sample thickness (Equation B.6). Q_{av} is the parameter on which we focus on during the stages of charge accumulation and depletion.

$$Q_{av} = \frac{\int_0^v |Q(x)| dx}{v} \quad (\text{B.6})$$

Type of Charge

Beside the magnitude and location of SC, it is also important to know the polarity of the charge during application of the voltage, compared to the adjacent electrode:

Homocharge is the accumulation of SC near an electrode of the same polarity (Figure B.6(a)). This situation is common when charges are injected faster at the interface than that they are transported through the bulk of the insulation. Homocharge increases the stress in the insulating material, while reducing the stress for the interface.

Heterocharge is SC accumulation near an electrode with the opposite polarity (Figure B.6(b)). This occurs only if the bulk material transports the charge faster than it can be extracted at the interface. Heterocharge increases the stress at the interface, while reducing the stress for the insulation material. Thus heterocharge is more critical for an insulation system than homocharge.

Additionally to the aforementioned charges, lumped charges were witnessed in polymeric insulation for fields higher than 100 kV/mm [41]. Due to limitations of our test setups, field strengths of this magnitude are out of the scope of this thesis.

Description of Space Charge Dynamics

SC dynamics are governed by three processes: injection, transportation and recombination. The time dependency of the SC distribution is usually divided in two sections in terms of analysis: Formation of SC during poling

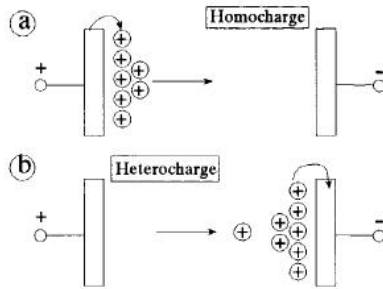


Figure B.6.: Illustration of the accumulation of (a) homocharge and (b) heterocharge.

and decay of SC during depoling. Since most insulation systems have different time constants for formation and decay, this is a valid classification and utilized in this work.

APPENDIX C

HEALTH AND SAFETY ISSUES

The processes that apply for ultrafine particles may be applicable for nanoparticles as well, with the exception of nanoparticles which surface has been coated to prevent agglomeration. There are three modes described for particles in [61]:

Large particles > 2000 nm are described as being in coarse mode and are subject to gravitational settling.

Small particles < 80 nm these particles are in agglomeration-mode and therefore short lived, because they agglomerate to larger particles very fast and form a mixture of large and intermediate particles.

Intermediate particles > 80 nm and < 2000 nm are described as being in accumulation mode and can remain suspended in air for days to weeks. They can be removed from air via dry or wet deposition. The term accumulation mode reflects that particles of this size can accumulate in living cells over weeks, months or even years.

Therefore the biggest threat comes rather from intermediate than small particles. Since these particles can stay for weeks in air, and since bacteria and living cells are able to take up this nanosized particles, the basis

for bioaccumulation in the food chain is given. Major targets where these particles usually accumulate are lungs, bones and the brain. Studies investigating the toxicity of carbon nanotubes showed that, once they reach the lungs, they are much more toxic than carbon black and can be more toxic than quartz. This is considered a serious occupational health hazard in chronic inhalation exposures [120, 121]. Toxicity of TiO_2 on the other hand has not been found to be dependent on particle size or surface area [122, 123]. Studies have demonstrated that nanotoxicity is extremely complex and depends on a multitude of factors like material, size, shape, charge, area or reactivity. It seems that the aspect ratio of the particles has significant effect on the toxicity. CNT have shown the same pathogenicity on mice as asbestos fibers, presumably due to their needle-like shape [124]. CNT should therefore be considered toxic to humans and strict industrial hygiene measures should be taken to limit exposure of humans to CNT [125].

As soon as nanoparticles are mixed into a given host material, they are bonded to the material on a molecular level and pose low to no threat. Dangerous is the time between breaking the agglomerates and introducing the surface-treated particles into a host material. During this time according safety measures are necessary [126]. It has been shown that wet cutting of NC with CNT does not lead to airborne nanoparticles emissions above background level, but that dry cutting generates significant quantities of nanoscale and fine particles [127]. Interestingly, the study found no evidence of CNTs, either individual or in bundles, in microscopy of the collected samples for either wet or dry cutting.

APPENDIX D

ZETA POTENTIAL

The ζ potential can be calculated by determining the electrophoretic mobility and then applying the Henry equation. Given a number of particles inside a solution, the development of a net charge at the particle surfaces affects the distribution of ions in the surrounding interfacial region, thus increasing the concentration of counter ions close to the surface, forming an electric double layer according to Helmholtz (description see section 3.3.1 on page 33) around each particle. This double layer consists of the:

Stern layer the inner region where ions are strongly bound and the

Outer layer a diffuse region where ions have a higher mobility.

When a particle is moving due to e.g. gravitational settlement, the ions within the boundaries of this double layer travel with the particle. Any ions beyond the boundary do not move with the particle. This border is called the surface of hydrodynamic shear or slipping plane. The electric potential at the slipping plane is called ζ potential (see Figure D.1). The ζ potential gives an indication of the stability of a colloidal system¹.

¹colloidal system: a system where one of the three states of matter (gas, liquid, solid) is finely dispersed in one of the others.

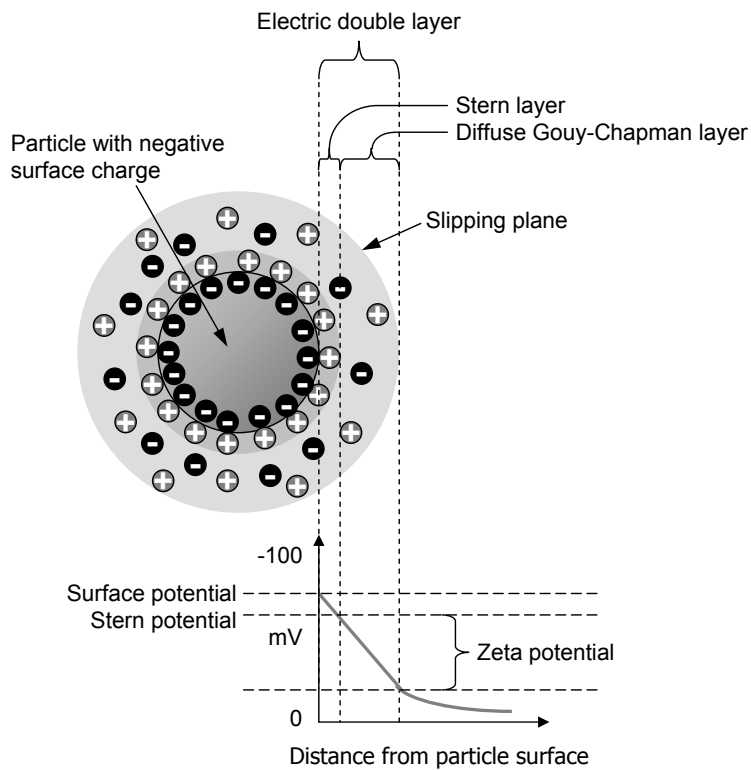


Figure D.1.: Illustration of surface potential, Stern potential, ζ potential and the electrical double layer around a particle.

Table D.1.: pH values for a zeta potential close to the isoelectric point of the used particles.

particle	pH value needed
Al ₂ O ₃	4
AlN	4
MgO	3
BN	2

The general dividing line between stable and unstable suspensions is at either +30 or -30 mV. Particles with a ζ potential more positive than +30 mV, or more negative than -30 mV, are considered stable. The ζ potential of 0 mV is called isoelectric point, the point where the solution is the least stable. The pH is an important factor for the ζ potential. A ζ potential value without a quoted pH is virtually meaningless. The particles we use are stable at pH 7. In order to break up the agglomerates more easily, the pH had to be adjusted. Table D.1 shows the pH values for reaching the isoelectric point for the nanoparticles the synthesis was applied to in the course of this work.

LIST OF SYMBOLS AND ABBREVIATIONS

Abbreviation	Description
AC	Alternating current
AlN	Aluminum nitride
Al ₂ O ₃	Aluminum oxide
AlO(OH)	Aluminum oxide hydroxide (Diaspore)
BCC	Body-centered cubic (unit cell)
BD	Dielectric breakdown
BN	Boron nitride
CFC	Conventional filled composite
(MW)CNT	(Multi-walled) Carbon nanotube
DC	Direct current
DS	Dielectric spectroscopy
EPPS	3-(2,3-epoxypropoxy)propyltrimethoxysilane
H	System response of the PEA setup
LAD	Laser diffraction
LiNbO ₃	Lithium niobate

Abbreviation	Description
MC	Mesocomposite
MgO	Magnesium oxide
MMT	Montmorillonite
NC	Nanocomposite
NMC	Nano-micro-composite
NP	Nanoparticle
NSC	Nano-meso-composite
PA	Polyamide
PC	Polycarbonate
PCAM	Polymer chain alignment model
PE	Polyethylene
PEA	Pulsed electro-acoustic method
PMMA	Polymethyl methacrylate
PNC	Polymer nanocomposite
PTFE	Polytetrafluorethylene
PVC	Polyvinyl chloride
PVDF	Polyvinylidene fluoride
SC	Space charge
SCA	Silane coupling agent
SEM	Scanning electron microscope
STM	Scanning tunneling microscope
TEM	Transmission electron microscope
TGA	Thermogravimetric analysis

Symbol	Unit	Description
a	nm	Length of body-centered cubic unit cell
$A_{m,el}$	m^2	Area of the measuring electrode
b	nm	Interparticle distance
d	nm	Average particle diameter
E	kV/mm	Breakdown field strength
F(x)	%	Failure probability of x
I_α	various	Intensity of α
J_{SS}	$A \cdot m^{-2}$	Steady-state value of the current density
Q_{av}	C/m^3	Average amount of space charge
$\tan(\delta)$	-	Loss tangent
T_g	K	Glass transition temperature
v_s	m/s	Sound velocity
α	various	Material property (Intensity model)
β	-	Weibull shape parameter
ϵ_0	$C^2 \cdot s^2 \cdot kg^{-1} \cdot m^{-3}$	Permittivity of vacuum
ϵ^*	-	Complex permittivity
ϵ'	-	Real part of ϵ^*
ϵ''	-	Imaginary part of ϵ^*
ϵ_r	-	Relative permittivity
η	various	Weibull scale parameter
ω	Hz	Angular frequency
σ	$S \cdot m^{-1}$	Conductivity

LIST OF FIGURES

1.1.	Illustration of how the ratio of the filler material to the interfacial area changes with the size of the filler.	3
1.2.	Life cycle perspective risk assessment. Images: Suat Eman and Federico Stevanin / FreeDigitalPhotos.net	8
2.1.	Illustration of the polymer backbone of PE, consisting of a chain of carbon atoms.	12
2.2.	Chemical structure of the epoxide ring (a), the diepoxide structure (b) and bisphenol-A (c).	14
2.3.	Chemical structure of 3-(2,3-epoxypropoxy)propyltrimethoxysilane (EPPS).	18
2.4.	Hydrolysis, reaction of EPPS with H ₂ O to form free OH-groups for bonding with the nanoparticles.	19
2.5.	Schematic of one nanoparticle and the EPPS layer grafted on it.	21
2.6.	TEM micrograph of 2 wt.% Al ₂ O ₃ particles in an epoxy film. The bright circles larger than 1 μm are part of the sample holder in the background.	26

2.7.	TEM micrograph of 5 wt.% Al_2O_3 particles in an epoxy film. The bright circles larger than $1 \mu\text{m}$ are part of the sample holder.	27
3.1.	Illustration of surface potential, Stern potential, ζ potential and the electrical double layer around a particle.	35
3.2.	The interface ab between two phases A and B defined by the intensity I_α of a chosen property α as it changes in passage across it [73].	35
3.3.	Interfacial intensities: electron concentration at a metal vacuum interface (a), oxygen concentration at silicon-air boundary (b) and electric field at metal-n-type semiconductor interface (c) [73].	36
3.4.	Illustration of the multi-core model [64].	37
3.5.	Interphase content according to the Interphase Volume Model for silicone rubber with SiO_2 nanoparticles and interphase thickness i for average diameter d of (a) 20 nm, (b) 30 nm and (c) 40 nm [75].	39
3.6.	Illustration of the reaction of a particle surface area of 1 nm^2 with a EPPS molecule.	41
3.7.	Illustration of the interpenetrating polymer network at the interface between particle and host, with (a) being the mineral surface, (b) the covalently bonded interface and (c) the polymer network altered by the surface modification.	42
3.8.	(a) Particle without surface modification and thus only weak interaction with the host; (b) Particle with layer of surface modification, resulting layer of aligned polymer chains, further affecting the surrounding area thus restructuring the polymer.	42
3.9.	Body-centered cubic unit cell.	43
3.10.	Illustration of the interparticle distance b , body and space diagonal of a body-centered cubic unit cell.	45
3.11.	Interparticle distance b as function of fillgrade in wt.% for different filler materials.	47

3.12. Illustration how crystallinity can change from particle to surrounding polymer. The particle itself can be crystalline or amorphous.	48
3.13. Volume percentages of host material, particles, aligned and affected layers for one BCC unit cell, calculated for various nanoparticles: Al ₂ O ₃ 3.13(a), MgO 3.13(b), AlN 3.13(c) and SiO ₂ 3.13(d). For this calculation a thickness of the aligned inner layer t_i of 5 nm was chosen, while the thickness of the outer layer t_o is 10 nm.	49
3.14. Illustration how nanoparticles can contribute to conduction.	52
3.15. Illustration how nanoparticles can contribute to conduction shown at two different particles: on the left MgO with bandgap of 7.8 eV and TiO ₂ on the right with 3.2 eV bandgap and larger distance to the vacuum level.	53
3.16. Illustration how agglomerations of nanoparticles can lead to field enhancements, compared to a NC without agglomerations.	56
3.17. Illustration how nanoparticles can hinder electrical treeing, compared to larger particles.	57
4.1. Electrode configuration for BD tests.	60
4.2. Weibull plot for SiO ₂ -ER NC.	64
4.3. Weibull plot for Al ₂ O ₃ -ER NC.	64
4.4. Weibull plot for AlN-ER NC.	65
4.5. Weibull plot for MgO-ER NC.	66
4.6. Weibull plot for Al ₂ O ₃ -ER NC with adjusted sample populations.	66
4.7. Weibull plot for AlN-ER NC with adjusted sample populations.	67
4.8. Weibull plot for SiO ₂ -ER NC with adjusted sample populations.	67
4.9. Weibull scale parameter with confidence bounds for epoxy NC as function of fillgrade.	68
4.10. Weibull scale parameter with confidence bounds for BN-epoxy samples with 10 wt.% as function of filler size.	69

5.1.	Equivalent circuit diagram of the DS setup.	73
5.2.	Real (a) and imaginary part (b) of the complex permittivity of unmodified epoxy for different temperatures as a function of frequency.	74
5.3.	Imaginary part of the complex permittivity of unfilled epoxy at different frequencies as function of temperature.	75
5.4.	Impact of the curing time (a) on the real part of the complex permittivity of conventional filled Al ₂ O ₃ -ER with 10 wt.% fillgrade at 293 K as a function of frequency. The figure on the right (b) shows the impact of the particle modification on a Al ₂ O ₃ -ER CFC with 10 wt.% fillgrade at 293 K.	76
5.5.	Impact of the filler type on the real part of the complex permittivity of NC with 2 wt.%, for 292 K (a) and 353 K (b), compared to neat ER as a function of frequency.	78
5.6.	Impact of the filler type on the imaginary part of the complex permittivity for 293 K (a) and 353 K (b), compared to neat ER as a function of frequency.	78
5.7.	Impact of the filler type on the tan(δ) of the complex permittivity for 293 K (a) and 353 K (b), compared to neat ER as a function of frequency.	79
5.8.	Arrhenius plot for unfilled epoxy compared to NC with different filler types. Activation energies derived from this plot are given in Table 5.1.	79
5.9.	Imaginary part of the complex permittivity of Al ₂ O ₃ -ER with 2 wt.% at different frequencies as function of temperature.	80
5.10.	Real part of the complex permittivity of MgO-ER nanocomposites at 293 K compared to neat ER as a function of frequency.	82
5.11.	Imaginary part of the complex permittivity of MgO-ER nanocomposites at 293 K compared to neat ER as a function of frequency.	82
5.12.	Relative permittivity of Al ₂ O ₃ -ER, MgO-ER and SiO ₂ NC for 1.15 kHz at 293 K as a function of fillgrade.	83

5.13. Comparison of calculated and measured values for Al ₂ O ₃ -ER (a) and MgO-ER (b).	84
5.14. Real part of the complex permittivity at 293 K for composites with 5wt.% Al ₂ O ₃ , compared to neat ER as a function of frequency.	86
5.15. Dielectric losses at 293 K for composites with 5wt.% Al ₂ O ₃ compared to neat ER as a function of frequency.	87
5.16. Real part of the complex permittivity of BN-ER nanocomposites with a fillgrade of 10 wt.% at 1.15 kHz, compared to neat ER as a function of temperature.	87
6.1. Equivalent circuit diagram of the sample configuration and test setup for space charge measurements with the PEA method.	92
6.2. Illustration of the increase of the creepage length by utilizing a rubber layer.	94
6.3. Growth of average space charge for MgO-ER-composites compared to neat ER for 15 kV/mm poling field at 293 K (voltage-on measurement).	96
6.4. Growth of average space charge for Al ₂ O ₃ -ER-composites compared to neat ER for 15 kV/mm poling field at 293 K (voltage-on measurement).	96
6.5. Growth of average space charge for AlN-ER-composites compared to neat ER for 15 kV/mm poling field at 293 K (voltage-on measurement).	97
6.6. Growth of average space charge for BN-ER-composites compared to neat ER for 15 kV/mm poling field at 293 K (voltage-on measurement).	98
6.7. Growth of average space charge for BN-ER-composites compared to neat ER for 15 kV/mm poling field at 293 K (voltage-on measurement).	99
6.8. Space charge profiles of unfilled epoxy for different poling field strengths after 1 hour of poling (voltage-off-profile) at 273 K.	100

6.9. Space charge profiles of unfilled epoxy for different poling field strengths after 1 hour of poling (voltage-off-profile) at 333 K.	100
6.10. Evolution of SC over time along the thickness of the sample, for unfilled epoxy for a poling field of 18 kV/mm: poling at 293 K (a) and depoling at 293 K (b); poling at 333 K (c) depoling at 333 K (d).	101
6.11. Space charge profiles for MgO-ER with 5 wt.% fillgrade for different poling field strengths after 1 hour of poling (voltage-off-profile) at 293 K.	102
6.12. Space charge profile for MgO-ER with 5 wt.% fillgrade for different poling field strengths after 1 hour of poling (voltage-off-profile) at 333 K.	103
6.13. Evolution of SC over time along the thickness of the sample, for MgO-ER with 5 wt.% for a poling field of 18 kV/mm: poling at 293 K (a) and depoling at 293 K (b); poling at 333 K (c) depoling at 333 K (d).	104
6.14. Space charge profiles for AlN-ER with 2 wt.% fillgrade for different poling field strengths after 1 hour of poling at 293 K.	105
6.15. Space charge profiles for AlN-ER with 5 wt.% fillgrade for different poling field strengths after 1 hour of poling at 293 K.	105
6.16. Depletion of average space charge for different NC compared to neat ER for a poling field of 15 kV/mm at 293 K.	106
6.17. Distribution of the electric field in unfilled epoxy (a) and MgO-ER with 5 wt.% (b) at 333 K.	107
7.1. Alternative particle preparation: (a) dispersion of particles in a solvent, e.g. water or toluene; (b) surface functionalization by adding silane; (c) agglomerations of functionalized, hydrophobic particles; (d) filtration	115

7.2. A concentrated mixture of NP in a carrier polymer (a) is cooled down (b) and cut into granular shape (c), which enables long term storage (d). After storage the masterbatch can be used by heating up (e) and diluting with the respective monomer and a constituent amount of curing agent while mixing (f), before casting and curing.	116
A.1. XRD spectra of Al ₂ O ₃ A.1(a) and AlN A.1(b) particles. . .	128
A.2. Comparison of the Al ₂ O ₃ dispersion in water and ethanol. .	131
A.3. Influence of the mixing method Al ₂ O ₃ in ethanol.	131
A.4. Influence of the application time of the ultrasonic bath on the Al ₂ O ₃ dispersion in ethanol.	132
A.5. Influence of the silane treatment on the Al ₂ O ₃ dispersion in ethanol after 5 days of storage.	132
A.6. TGA analysis on Al ₂ O ₃ samples with and without surface functionalization. It shows a much higher weight loss for treated particles, indicating successful surface functionalization.	134
A.7. TGA analysis on Al ₂ O ₃ samples with and without surface functionalization. It shows a much higher weight loss for treated particles, indicating successful surface functionalization.	135
A.9. Overview of usability of different types of microscopy.	135
A.8. TGA analysis on Al ₂ O ₃ -epoxy sample with 0.5% per weight. It shows that the amount of particles in top, centre and bottom of the sample does not change significantly, hence the sedimentation encountered in the composite is negligible.	136
A.10. TEM micrograph of various nanoparticles: Al ₂ O ₃ A.10(a), MgO A.10(b), AlN A.10(c) and BN A.10(d).	138
A.11. TEM micrograph of Al ₂ O ₃ -ER NC.	139
A.12. SEM micrographs of Al ₂ O ₃ -ER with 0.5% A.12(a) and 10% A.12(b) per weight with 20.000 times magnification. Quantitative analysis of the components of our sample shows Al well dispersed in the epoxy.	140

A.13. Dynamic loss modulus E'' for unfilled epoxy (18 hours curing at 413 K) acquired with DMTA at 1 Hz.	143
B.1. Equivalent circuit diagram of the DS setup.	146
B.2. The polarisation spectrum with orientational, ionic and electronic polarisation mechanism.	147
B.3. The polarisation spectrum as function of temperature with DC conductivity, α - and β -relaxation.	148
B.4. Equivalent circuit diagram of the sample configuration and test setup for space charge measurements with the PEA method.	151
B.5. Typical space charge profile of neat epoxy. The Y-axis shows the amount of space charge, the X-axis represents the location of the charge. On the left border of the graph the interface between high voltage electrode and sample can be seen. On the right side is the interface between ground electrode and sample. In this case we have heterocharge at the ground electrode.	155
B.6. Illustration of the accumulation of (a) homocharge and (b) heterocharge.	157
D.1. Illustration of surface potential, Stern potential, ζ potential and the electrical double layer around a particle.	162

LIST OF TABLES

1.1. Examples of small-scale structures and events, taken from [5]	4
2.1. List of filler material used, properties derived from TEM and XRD measurement.	17
3.1. Common bonds in polymers, their bonding distance and energy [69].	32
3.2. Theoretical length a of a BCC unit cell for different NC and average distance between particles b	46
3.3. Band gaps and vacuum levels of particles from literature [84, 85, 86].	52
3.4. Electrical properties of particles from literature.	54
4.1. Weibull parameters for DC ramp BD test on various specimens with 90% confidence bounds.	63
4.2. Scale and shape parameter for MgO-ER.	65
4.3. Weibull parameters for DC ramp BD test on BN-ER specimens with 90% confidence bounds.	69
5.1. Activation energies derived from Arrhenius plot (Figure 5.8). 81	

5.2.	Measured values for ϵ' of BN-ER NC at 1.15 kHz compared to values obtained by rules of mixture.	88
6.1.	Maximum field enhancement for unmodified epoxy and MgO-ER with 5 wt.% at different poling field strengths.	108
7.1.	Examples for solvents that can be used.	114
A.1.	Particle properties as indicated by TEM analysis	139
B.1.	Properties of the PEA setups used in this work.	152
D.1.	pH values for a zeta potential close to the isoelectric point of the used particles.	163

BIBLIOGRAPHY

- [1] M. Reibold, R. Paufler, A.A. Levin, W. Kochmann, N. Pätzke, and D.C. Meyer. Discovery of nanotubes in ancient damascus steel. *Springer Proceedings in Physics; Physics and Engineering of New Materials*, 127:305–310, 2009.
- [2] R.P. Feynman. There’s plenty of room at the bottom. Lecture at an American Physical Society meeting at Caltech, December 1959.
- [3] N. Taniguchi. On the basic concept of ‘nano-technology’. In *Int. Conference Proceedings Engineering Tokyo*, page ??, 1974.
- [4] R. Roy and S. Komarneni. Nanophase and nanocomposite materials. In *Materials Research Society*, page 241, 1984.
- [5] M.F. Fréchet, M.L. Trudeau, H.D. Alamdari, and S. Boily. Introductory remarks on nanodielectrics. *IEEE Transactions on Dielectrics and Electrical Insulation*, 11:808–818, 2004.
- [6] G. Binnig and H. Rohrer. Scanning tunneling microscopy. *IBM Journal of Research and Development*, 30, 1986.
- [7] M. Monthieux and V.L. Kuznetsov. Who should be given the credit for the discovery of carbon nanotubes? *Carbon*, 44:1621–1623, 2006.

- [8] M. Bockrath, D.H. Cobden, P.L. McEuen, N.G. Chopra, A. Zettl, A. Thess, and R.E. Smalley. Single-electron transport in ropes of carbon nanotubes. *Science*, 275:1922–1925, 1997.
- [9] S.J. Tans, M.H. Devoret, H. Dai, A. Thess, R.E. Smalley, L.J. Geerligs, and C. Dekker. Individual single-wall carbon nanotubes as quantum wires. *Nature*, 387:474–477, 1997.
- [10] S. Steen, S.J. McNab, L. Sekaric, I. Babic, J. Patel, J. Bucchignano, M. Rooks, D.M. Fried, A.W. Topop, J.R. Brancaccio, R. Yu, J.M. Hergenrother, J.P. Doyle, R. Nunes, R.G. Viswanathan, S. Purushothaman, and M.B. Rothwell. Hybrid lithography: The marriage between optical and e-beam lithography. a method to study process integration and device performance for advanced device nodes. *Microelectronic Engineering*, 83:754–761, 2006.
- [11] Sigma Aldrich. Fumed silica product information (cas 112945-52-5). available online.
- [12] A. Okada, Y. Fukushima, M. Kawasumi, S. Inagaki, A. Usuki, S. Sugiyama, T. Kurauchi, and O. Kamigaito. Composite material and process for manufacturing same, 1988.
- [13] R.K. Gupta, E. Kennel, and K.-J. Kim. *Polymer Nanocomposites Handbook*. CRC Press, 2010.
- [14] K.E. Drexler. *Engines of Creation - The Coming Era of Nanotechnology*. Anchor Books, 1986.
- [15] M. Crichton. *Prey*. HarperCollins, 2002.
- [16] R.C. Cooper. Stargate sg1. TV series, February 2000. Nemesis, Season 3, Episode 22.
- [17] Nevelidine/Taylor. Gamer. movie, September 2009.
- [18] W. Spector. Deus ex. video game, June 2000.

- [19] E.A.G. Hamers, M.N. van der Donker, B. Stannowski, R. Schlattmann, and G.J. Jongerden. Helianthos: Roll-to-roll deposition of flexible solar cell modules. *Plasma Processes and Polymers*, 4:275–281, 2007.
- [20] R. Bartl, R. Schlattmann, B. Stannowski, A. Gordijn, M.N. van den Donker, F. Finger, and B. Rech. Tco development for thin film silicon solar cells. In *Proceedings of the 21st European Photovoltaic Solar Energy Conference*, 2006.
- [21] J.G. Hwang, F. O’Sullivan, M. Zahn, O. Hjortstam, L.A.A. Pettersson, and R. Liu. Modeling of streamer propagation in transformer oil-based nanofluids. In *Annual Report Conference on Electrical Insulation and Dielectric Phenomena*, pages 361–366, 2008.
- [22] J.G. Hwang, M. Zahn, F.M. O’Sullivan, L.A.A. Pettersson, O. Hjortstam, and R. Liu. Electron scavenging by conductive nanoparticles in oil insulated power transformers. In *Electrostatics Joint Conference Proceedings*, pages 1–12, 2009.
- [23] T.J. Lewis. Nanometric dielectrics. *IEEE Transactions on Dielectrics and Electrical Insulation*, 1:821–825, 1994.
- [24] L.A. Dissado and J.C. Fothergill. Dielectrics and nanotechnology. *IEEE Transactions on Dielectrics and Electrical Insulation*, 11:737–738, 2004.
- [25] M.F. Frechette, A. Vijn, L. Utracki, M.L. Trudeau, A. Sami, C. Laurent, P.H.F. Morshuis, T. Andritsch, R. Kochetov, A. Vaughan, E. David, J. Castellon, D. Fabiani, S. Gubanski, J. Kindersberger, C. Reed, A. Krivda, J. Fothergill, S. Dodd, F. Guastavino, and H. Alamdari. Nanodielectrics - a universal panacea for solving all electrical insulation problems? In *10th IEEE International Conference on Solid Dielectrics, Potsdam, Germany*, 2010.
- [26] M. Kozako, N. Fuse, K. Shibata, N. Hirai, Y. Ohki, T. Okamoto, and T. Tanaka. Surface change of polyamide nanocomposites caused

- by partial discharges. In *Annual Report Conference on Electrical Insulation and Dielectric Phenomena*, 2003.
- [27] M. Kozako, S. Kuge, T. Imai, T. Ozaki, T. Shimizu, and T. Tanaka. Surface erosion due to partial discharges on several kinds of epoxy nanocomposites. In *Annual Report Conference on Electrical Insulation and Dielectric Phenomena*, pages 162–165, 2005.
- [28] P.O. Henk, T.W. Kortsen, and T. Kvarts. Increasing the electrical discharge endurance of acid anhydride cured dgeba epoxy resin by dispersion of nanoparticle silica. *High Perform. Polym.*, 11:281–296, 1999.
- [29] T. Tanaka, T. Yazawa, Y. Ohki, M. Ochi, M. Harada, and T. Imai. Frequency accelerated partial discharge resistance of epoxy/clay nanocomposite prepared by newly developed prganic modification and solubilization methods. In *International Conference on Solid Dielectrics, Winchester, UK*, pages 337–340, 2007.
- [30] T. Tanaka, Y. Matsuo, and K. Uchida. Partial discharge endurance of epoxy / sic nanocomposite. In *Annual Report Conference on Electrical Insulation and Dielectric Phenomena*, pages 13–16, 2008.
- [31] H.Z. Ding and B.R. Varlow. Effect of nano-fillers on electrical treeing in epoxy resin subjected to ac voltage. In *Annual Report Conference on Electrical Insulation and Dielectric Phenomena*, 2004.
- [32] T. Imai, F. Sawa, T. Ozaki, T. Shimizu, R. Kido, M. Kozako, and T. Tanaka. Influence of temperature on mechanical and insulation properties of epoxy-layered silicate nanocomposite. *IEEE Transactions on Dielectrics and Electrical Insulation*, 13:445–452, 2006.
- [33] L. Hui, R. Smith, J.K. Nelson, and L.S. Schadler. Electrochemical treeing in xlpe/silica nanocomposites. In *Annual Report Conference on Electrical Insulation and Dielectric Phenomena*, 2009.

- [34] S. Rätzke and J. Kindersberger. Werkstoffe mit nanofüllstoffen für freiluftisolierungen? In *ETG-Fachtagung "Grenzflächen in elektrischen Isoliersystemen" vom 8. bis 9. März in Hanau*, 2005.
- [35] S. Rätzke and J. Kindersberger. Erosion behaviour of nano filled silicone elastomers. In *Proceedings of the XIVth International Symposium on High Voltage Engineering, Tsinghua University, Beijing, China*, 2005.
- [36] G.C. Montanari, D. Fabiani, F. Palmieri, D. Kaempfer, R. Thomann, and R. Müllhaupt. Modification of electrical properties and performance of eva and pp insulation through nanostructure by organophilic silicates. *IEEE Transactions on Dielectrics and Electrical Insulation*, 11:754–762, 2004.
- [37] F. Guastavino, A. Dardano, A. Ratto, E. Torello, P. Tiemblo, M. Joyos, and J.M. Gómez-Elvira. Electrical characterization of polymer-layered silicate nanocomposites. In *Annual Report Conference on Electrical Insulation and Dielectric Phenomena*, pages 175–178, 2005.
- [38] S.S. Bamji, M. Abou-Dakka, and A.T. Bulinski. Dielectric properties of polypropylene containing nano-particles. In *Annual Report Conference on Electrical Insulation and Dielectric Phenomena*, pages 166–170, 2005.
- [39] E. Tuncer, I. Sauers, D.R. James, A.R. Ellis, M.P. Paranthaman, T. Aytug, S. Sathyamurthy, K.L. More, J. Li, and A. Goyal. Electrical properties of epoxy resin based nano-composites. *Nanotechnology*, 18, 2007.
- [40] C.D. Green and A.S. Vaughan. Polyethylene / montmorillonite nanocomposites: Effect of masterbatch composition and maleic anhydride on ac electrical breakdown performance. In *International Conference on Solid Dielectrics, Winchester, UK*, pages 364–367, 2007.

- [41] Y. Murata, Y. Murakami, M. Nemoto, Y. Sekiguchi, Y. Inoue, M. Kanaoka, N. Hozumi, and M. Nagao. Effects of nano-sized mgo-filler on electrical phenomena under dc voltage application in ldpe. In *Annual Report Conference on Electrical Insulation and Dielectric Phenomena*, pages 158–161, 2005.
- [42] S. Okuzumi, Y. Murakami, and M. Nagao. Dc breakdown strength and conduction current of mgo/ldpe composite influenced by filler size. In *Annual Report Conference on Electrical Insulation and Dielectric Phenomena*, pages 722–725, 2008.
- [43] D. Fabiani, G.C. Montanari, A. Dardano, G. Guastavino, L. Testa, and M. Sangermano. Space charge dynamics in nanostructured epoxy resin. In *Annual Report Conference on Electrical Insulation and Dielectric Phenomena*, pages 710–713, 2008.
- [44] N. Fuse, T. Tanaka, and Y. Ohki. Evaluation of dielectric properties in polypropylene/clay nanocomposites. In *Annual Report Conference on Electrical Insulation and Dielectric Phenomena*, 2009.
- [45] J. Yoshida, T. Maezawa, Y. Tanaka, T. Takada, H. Miyake, Y. Sekiguchi, Y. Murata, and C. Reddy. Space charge accumulation and breakdown in ldpe and lepe/mgo nano composites under high dc stress at various temperatures. In *Annual Report Conference on Electrical Insulation and Dielectric Phenomena*, 2009.
- [46] J-Power Systems. Jp2007103247, 2007.
- [47] A. Motori, F. Patuelli, A. Saccani, G.C. Montanari, and R. Müllhaupt. Improving thermal endurance properties of polypropylene by nanostructuring. In *Annual Report Conference on Electrical Insulation and Dielectric Phenomena*, pages 195–198, 2005.
- [48] Y. Miyazaki, T. Nishiyama, H. Takahashi, J. Katagiri, and Y. Takezawa. Development of highly thermoconductive epoxy composites. In *Annual Report Conference on Electrical Insulation and Dielectric Phenomena*, 2009.

- [49] R. Kochetov, T. Andritsch, U. Lafont, P.H.F. Morshuis, and J.J. Smit. Thermal conductivity of nano-filled epoxy systems. In *Annual Report Conference on Electrical Insulation and Dielectric Phenomena*, 2009.
- [50] J.W. Gilman, C.L. Jackson, A.B. Morgan, R. Harris Jr., E. Manias, E.P. Giannelis, M. Wuthenow, D. Hilton, and S.H. Philips. Flammability properties of polymer-layered silicate nanocomposites. polypropylene and polystyrene nanocomposites. *Chem. Mater.*, 12:1866–1873, 2000.
- [51] L. Qiu, R. Xie, P. Ding, and B. Qu. Preparation and characterisation of mg(oh)₂ nanoparticles and flame-retardant property of its nanocomposites with eva. *Composite Structures*, 62:391–395, 2003.
- [52] M. Okoshi and H. Nishizawa. Flame retardency of nanocomposites. *Fire and Materials*, 28:423–429, 2004.
- [53] T. Imai, F. Sawa, T. Ozaki, Y. Inoue, T. Shimizu, and T. Tanaka. Roles of fillers on properties of nano-tio₂ and micro-sio₂ filler mixed composites. In *International Conference on Solid Dielectrics, Winchester, UK*, pages 407–410, 2007.
- [54] M. Hyuga, N. Tagami, T. Tanaka, Y. Ohki, T. Imai, M. Harada, and M. Ochi. Improvement in high-temperature dielectric properties of epoxy resin by abundant addition of micro-silica. In *Annual Report Conference on Electrical Insulation and Dielectric Phenomena*, 2009.
- [55] T. Imai, F. Sawa, T. Ozaki, T. Shimizu, R. Kido, M. Kozako, and T. Tanaka. Effects of nano- and micro-filler mixture on electrical insulation properties of epoxy based composites. *IEEE Transactions on Dielectrics and Electrical Insulation*, 13:319–326, 2006.
- [56] T. Tanaka, D. Ueno, T. Iizuka, Y. Ohki, Y. Sekiguchi, and Y. Murata. Tree initiation and growth in ldpe/mgo nanocomposites and roles of nano fillers. In *Annual Report Conference on Electrical Insulation and Dielectric Phenomena*, page 4, 2009.

- [57] T.J. Lewis. A model for nano-composite polymer dielectrics under electrical stress. In *International Conference on Solid Dielectrics, Winchester, UK*, pages 11–14, 2007.
- [58] M. Roy, J.K. Nelson, L.S. Schadler, C. Zou, and J.C. Fothergill. The influence of physical and chemical linkage on the properties of nanocomposites. In *Annual Report Conference on Electrical Insulation and Dielectric Phenomena*, 2005.
- [59] J.G. Hwang, M. Zahn, F.M. O’Sullivan, L.A.A. Pettersson, Olof Hjortstam, and R. Liu. Electron scavenging by conductive nanoparticles in oil insulated power transformers. In *Electrostatics Joint Conference*, 2009.
- [60] P. Aksamit and D. Zmarzly. Dielectric properties of fullerene-doped insulation liquids. In *Annual Report Conference on Electrical Insulation and Dielectric Phenomena*, 2009.
- [61] U.S. Environmental Protection Agency (EPA). Nanotechnology white paper.
- [62] T. Maezawa, J. Taima, Y. Hayase, Y. Tanaka, and T. Takada. Space charge formation in ldpe/mgo nano-composite under high electric field at high temperature. In *Annual Report Conference on Electrical Insulation and Dielectric Phenomena*, pages 271–274, 2007.
- [63] P. Bowen, J.G. Highfield, A. Mocellin, and T.A. Ring. Degradation of aluminum nitride powder in aqueous environment. *Journal of the American Ceramics Society*, 73(3):724–728, 1990.
- [64] T. Tanaka. Dielectric nanocomposites with insulating properties. *IEEE Transactions on Dielectrics and Electrical Insulation*, 12:914–928, 2005.
- [65] G. Banhegy. Comparison of electrical mixture rules for composites. *Colloid & Polymer Science*, 264:1030–1050, 1986.

- [66] B. Sareni, L. Krähenbühl, and A. Beroual. Effective dielectric constant of random composite materials. *Journal of Applied Physics*, 81:2375–2383, 1997.
- [67] T. Andritsch, R. Kochetov, P.H.F. Morshuis, and J.J. Smit. Comparison of the dielectric response of alumina-epoxy composites with nano- and conventional sized filler. In *Proceedings of the 16th international symposium on high voltage engineering*, page 31, 2009.
- [68] J. Clayden, N. Greeves, S. Warren, and P. Wothers. *Organic Chemistry*. Oxford Press, 2001.
- [69] H. Dominghaus. *Die Kunststoffe und ihre Eigenschaften*. Springer Verlag, 2005.
- [70] E. Urbaczewski-Espuche, J. Galy, J.-F. Gerard, J.-P. Pascault, and H. Sautereau. Influence of chain flexibility and crosslink density on mechanical properties of epoxy/amine networks. *Polymeric Engineering and Science*, 31:1572–1580, 1991.
- [71] S. Nilsson, T. Hjertberg, and A. Smedberg. The effect of crosslinking on electrical properties in ldpe. In *Proceedings of the 21st Nordic Insulation Symposium*, pages 229–232, 2009.
- [72] T.J. Lewis. Interfaces are the dominant feature of dielectrics at the nanometric level. *IEEE Transactions on Dielectrics and Electrical Insulation*, 11:739–753, 2004.
- [73] T.J. Lewis. Interfaces - nanometric dielectrics. *Journal of Physics D - Applied Physics*, 38:202–212, 2005.
- [74] T. Tanaka, M. Kozako, N. Fuse, and Y. Ohki. Proposal of a multi-core model for polymer nanocomposite dielectrics. *IEEE Transactions on Dielectrics and Electrical Insulation*, 12:669–681, 2005.
- [75] S. Rätzke and J. Kindersberger. Resistance to high voltage arcing and the resistance to tracking and erosion for silicone/sio2 nanocomposites. In *16th International Symposium on High Voltage Engineering*, 2009.

- [76] S. Rätzke. *Zur Wirkungsweise von nanoskaligen Füllstoffpartikeln in polymeren Isolierwerkstoffen der Hochspannungstechnik*. PhD thesis, TU Munich, 2009.
- [77] S. Rätzke and J. Kindersberger. Role of interphase on the resistance to high-voltage arcing, on tracking and erosion of silicone/sio2 nanocomposites. *IEEE Transactions on Dielectrics and Electrical Insulation*, 17:607–614, 2010.
- [78] J.-K. Kim and Y.-W. Mai. *Engineered Interfaces in Fiber Reinforced Composites*. Elsevier, 1998.
- [79] T.J. Ahmed. *Hybrid Composite Structures: Multifunctionality through Metal Fibres*. PhD thesis, Delft University of Technology, 2009.
- [80] T. Andritsch, R. Kochetov, Y.T. Gebrekiros, U. Lafont, P.H.F. Morshuis, and J.J. Smit. Synthesis and dielectric properties of epoxy based nanocomposites. In *Annual Report Conference on Electrical Insulation and Dielectric Phenomena*, 2009.
- [81] Yuli K. Godovsky. *Thermophysical properties of polymers*. Springer-Verlag Berlin, New York, 1992.
- [82] R. Bartnkias and R. M. Eichhorn, editors. *Engineering Dielectrics volume 2A - electrical properties of solid insulation materials: molecular structure and electrical behavior*. American society for testing and materials, 1983.
- [83] F.H. Kreuger. *Industrial High DC Voltage*. Delft University Press, 1995.
- [84] R.H. French. Electronic band structure of al₂o₃, with comparison to alon and aln. *Journal of the American Ceramics Society*, 73:447–489, 1990.
- [85] S. A. Canney, V.A. Sashin, M.J. Ford, and A.S. Kheifets. Electronic band structure of magnesium and magnesium oxide: experiment and theory. *J. Phys: Condens. Matter*, 11:7507–7522, 1999.

- [86] J. Pascual, J. Camassel, and H. Mathieu. Resolved quadrupolar transition TiO_2 . *Phys. Rev. Letter.*, 39:1490–1493, 1977.
- [87] M. Akatsuka and Y. Takezawa. Study of high thermal conductive epoxy resins containing controlled high-order structures. *Journal of Applied Polymer Science*, 89:2464–2467, 2003.
- [88] Vantico GmbH. Giessharzsysteme araldit cy 231 – härter hy 925, July 2000.
- [89] S. Rätzke, Y. Ohki, T. Imai, J. Kindersberger, and T. Tanaka. Enhanced performance of tree initiation v-t characteristics of epoxy/clay nanocomposite in comparison with neat epoxy resin. In *Annual Report Conference on Electrical Insulation and Dielectric Phenomena*, 2008.
- [90] E.F. Cuddihy. A concept for the intrinsic dielectric strength of electrical insulation materials. *IEEE Transactions on Electrical Insulation*, EI-22:573–589, 1987.
- [91] Electrical strength of insulating materials - test methods - part 1: tests at power frequencies, 1998.
- [92] Electrical strength of insulating materials - test methods - part 2: additional requirements for tests using direct voltage, 2001.
- [93] I.L. Hosier, A.S. Vaughan, and S.G. Swingler. The effects of measuring technique and sample preparation on the breakdown strength of polyethylene. *Dielectrics and Electrical Insulation, IEEE Transactions on*, 9:353–361, 2002.
- [94] G. Yilmaz and O. Kalenderli. The effect of thickness and area on the electric strength of thin dielectric films. In *Conference Record of the 1996 IEEE International Symposium on Electrical Insulation 1996*, 1996.
- [95] C. Zou, M. Fu, J.C. Fothergill, and S.W. Rowe. The influence of water on dielectric behavior of silica-filled epoxy nano-composites and

- percolation phenomenon. In *Annual Report Conference on Electrical Insulation and Dielectric Phenomena*, pages 372–375, 2007.
- [96] T. Andritsch, A. Lunding, P.H.F. Morshuis, H. Negle, and J.J. Smit. Permittivity in epoxy based syntactic foam nanocomposites. In *Annual Report Conference on Electrical Insulation and Dielectric Phenomena*, 2008.
- [97] G. Schaumburg. On the accuracy of dielectric measurements. *Dielectric Newsletter*, 8:5–10, 1997.
- [98] M. Roy, J.K. Nelson, L.S. Schadler, C. Zou, and J.C. Fothergill. The influence on physical and chemical linkage on the properties of nanocomposites. In *Annual Report Conference on Electrical Insulation and Dielectric Phenomena*, 2005.
- [99] N. McN. Alford, J. Breeze, and X. Aupi. Dielectric loss of oxide single crystals and polycrystalline analogues from 10 to 320 k. *Journal of the European Ceramic Society*, 21:2605–2611, 2001.
- [100] J.K. Nelson and J.C. Fothergill. Internal charge behaviour of nanocomposites. *Nanotechnology*, 15:585–595, 2004.
- [101] J.I. Hong, P. Winberg, L.S. Schadler, and R.W. Siegel. Dielectric properties of zinc oxide / low density polyethylene nanocomposites. *Materials Letters*, 59:474–476, 2005.
- [102] S-H. Xie, B-K. Zhu, J-B. Lo, X-Z. Wei, and Z-K Xu. Preparation and properties of polyimide / aluminum nitride composites. *Polymer testing*, 23:797–804, 2004.
- [103] Zhi-Ling Hou, Mao-Sheng Cao, Jie Yuan, Xiao-Yong Fang, and Xiao-Ling Shi. High-temperature conductance loss dominated defect level in h-bn: Experiments and first principles calculations. *Journal of Applied Physics*, 105:076103, 2009.
- [104] S.N. Bhattacharya, M.R. Kamal, and R.K. Gupta. *Polymeric Nanocomposites - Theory and Practice*. Hanser, 2008.

- [105] R. Bodega. *Space Charge Accumulation in polymeric High Voltage DC Cable Systems*. PhD thesis, Delft University of Technology, 2006.
- [106] M.J.P. Jeroense. *Charges and Discharges in HVDC Cables - in particular in mass-impregnated HVDC cables*. PhD thesis, Delft University of Technology, 1997.
- [107] M.J. Crimp, D.A. Oppermann, and K. Krehbiel. Suspension properties of hexagonal bn powders: effect of ph and oxygen content. *Journal of Materials Science*, 34:2621–2625, 1999.
- [108] A. Vale. Methanol. *Medicine*, 35(12):633–634, December 2007.
- [109] D. Lee, H. Kim, K. Yoon, K.E. Min, K.H. Seo, and S.K. Noh. Polyethylene/mmt nanocomposites prepared by in situ polymerization using supported catalyst systems. *Science and Technology of Advanced Materials*, 6:457–462, 2005.
- [110] E. Tuncer, G. Polizos, I. Sauers, D.R. James, A.R. Ellis, and K.L. More. Electrical properties of a polymeric nanocomposite with in-situ synthesized nanoparticles. In *Annual Report Conference on Electrical Insulation and Dielectric Phenomena*, 2009.
- [111] T. Iizuka, K. Uchida, and T. Tanaka. Different voltage endurance characteristics of epoxy/silica nanocomposites prepared by two kinds of dispersion methods. In *Annual Report Conference on Electrical Insulation and Dielectric Phenomena*, 2007.
- [112] M.F. Frechette, H.D. Martinez, A. Krivda, L.E. Smith, D. Zegarac, P.H.F. Morshuis, T. Andritsch, and R. Kochetov. Dielectric frequency response of epoxy-based composites with various silica filler sizes. In *International Conference on Solid Dielectrics, Potsdam, Germany*, 2010.
- [113] C.A. Randall, D.V. Miller, J.H. Adair, and A.S. Bhalla. Processing of electroceramic-polymer composites using the electrorheological effect. *Journal Materials Research Society*, 8(4):899–904, 1993.

- [114] M.W. Winslow. *Journal of Applied Physics*, 20:1137, 1949.
- [115] J.E. Martin, C.P. Tigges, R.A. Anderson, and J. Odinek. Enhanced dielectric standoff and mechanical failure in field-structured composites. *Physical Review B*, 60(10):7127–7139, 1999.
- [116] V. Tomer, C.A. Randall, G. Polizos, J. Kostelnick, and E. Manias. High- and low-field dielectric characteristics of dielectrophoretically aligned ceramic/polymer nanocomposites. *Journal of Applied Physics*, 103(034115), 2008.
- [117] R. Eberhardt, H.M. Muhr, W. Lick, F. Baumann, and G. Pukel. Comparison of alternative insulating fluids. In *Annual Report Conference on Electrical Insulation and Dielectric Phenomena*, pages 591–593, 2008.
- [118] T. Takada, Y. Tanaka, and N. Adachi. Comparison between the pea method and the pwp method for space charge measurement in solid dielectrics. *IEEE Transactions on Dielectrics and Electrical Insulation*, 5:944–951, 1998.
- [119] J. Beyer. *Space Charge and Partial Discharge Phenomena in HVDC Devices*. PhD thesis, Delft University of Technology, 2002.
- [120] K.L. Drehler. Toxicological highlight - health and environmental impact of nanotechnology: Toxicological assessment of manufactured nanoparticles. *Toxicological Sciences*, 77:3–5, 2004.
- [121] C. Lam, J.T. James, R. McCluskey, and R.L. Hunter. Pulmonary toxicity of single-wall carbon nanotubes in mice 7 and 90 days after intratracheal instillation. *Toxicological Sciences*, 77:126–134, 2004.
- [122] D.B. Warheit, T.R. Webb, C.M. Sayes, V.L. Colvin, and K.L. Reed. Pulmonary instillation studies with nanoscale tio2 rods and dots in rats: Toxicity is not dependent upon particle size and surface area. *Toxicological Sciences*, 91:227–236, 2006.

- [123] C.M. Sayes, R. Wahi, P.A. Kurian, Y. Liu, J.L. West, K.D. Ausman, D.B. Warheit, and V.L. Colvin. Correlating nanoscale titania structure with toxicity: A cytotoxicity and inflammatory response study with human dermal fibroblasts and human lung epithelial cells. *Toxicological Sciences*, 92:174–185, 2006.
- [124] C.A. Poland, R. Duffin, I. Kinloch, A. Maynard, W.A.H. Wallace, A. Seaton, V. Stone, S. Brown, W. MacNee, and K. Donaldson. Carbon nanotubes introduced into the abdominal cavity of mice show asbestos-like pathogenicity in a pilot study. *Nature Nanotechnology*, 3:423–428, 2008.
- [125] J. Muller, F. Huaux, N. Moreau, P. Misson, J.-F. Heilier, M. Delos, M. Arras, A. Fonseca, J.B. Nagy, and D. Lison. Respiratory toxicity of multi-wall carbon nanotubes. *Toxicology and Applied Pharmacology*, 207:221–231, 2005.
- [126] Editors J. Nijenhuis and V.C.L. Butselaar-Orthlieb. Tnw nanosafety guidelines. Delft University of Technology, Faculty of Applied Sciences, SHE Committee of DelftChemTech, September 2008.
- [127] D. Bello, B.L. Wardle, N. Yamamoto, R. Guzman deVilloria, E.J. Garcia, A.J. Hart, K. Ahn, M.J. Ellenbecker, and M. Hallock. Exposure to nanoscale particles and fibers during machining of hybrid advanced composites containing carbon nanotubes. *Journal of Nanoparticle Research*, 11:231–249, 2008.

LIST OF PUBLICATIONS

T. Andritsch. *Nanotechnologie in der Energietechnik*. Diploma thesis, Graz University of Technology, 2006.

T. Andritsch, A. Lunding, P.H.F. Morshuis, H. Negle and J.J. Smit. "Dielectric behavior of syntactic foams at low temperatures and frequencies", In *Annual Report Conference on Electrical Insulation and Dielectric Phenomena (CEIDP)*, Vancouver, Canada, 2007.

T. Andritsch, A. Lunding, P.H.F. Morshuis, H. Negle and J.J. Smit. "Changes in Permittivity of Syntactic Foam at low Temperatures and Frequencies", In *IEEE Young Researchers Symposium in Electrical Power Engineering*, Eindhoven, The Netherlands, 2008.

T. Andritsch, A. Lunding, P.H.F. Morshuis, H. Negle and J.J. Smit. "Permittivity in Epoxy based Syntactic Foam Nanocomposites", In *Annual Report Conference on Electrical Insulation and Dielectric Phenomena (CEIDP)*, Quebec City, Canada, 2008.

T. Andritsch, A. Lunding, P.H.F. Morshuis, H. Negle and J.J. Smit. "The Investigation of the Permittivity of Syntactic Foam under varying Humid-

ity", In *Annual Report Conference on Electrical Insulation and Dielectric Phenomena (CEIDP)*, Quebec City, Canada, 2008.

R. Kochetov, T. Andritsch, U. Lafont, P.H.F. Morshuis, S.J. Picken, J.J. Smit. "Preparation and Dielectric Properties of Epoxy-BN and Epoxy-AlN Nanocomposites", In *IEEE Electrical Insulation Conference (IEC)*, Montreal, QC, Canada, pp. 397-400, 31 May-3 June, 2009.

R. Kochetov, T. Andritsch, U. Lafont, P.H.F. Morshuis, S.J. Picken, J.J. Smit. "Thermal Behaviour of Epoxy Resin Filled with High Thermal Conductivity Nanopowders", In *IEEE Electrical Insulation Conference (IEC)*, Montreal, QC, Canada, pp. 524-528, 31 May-3 June, 2009.

T. Andritsch, R. Kochetov, Y.T. Gebrekiros, U. Lafont, P.H.F. Morshuis and J.J. Smit. "Space Charge Behavior of Epoxy based Nanocomposites with Al₂O₃ and AlN filler", In *Proceedings of the 21st Nordic Insulation Symposium*, Göteborg, Sweden, 2009.

T. Andritsch, R. Kochetov, P.H.F. Morshuis and J.J. Smit. "Comparison of the dielectric behavior of epoxy based Al₂O₃- and SiO₂-nanocomposites". In *Proceedings of the 21st Nordic Insulation Symposium*, Göteborg, Sweden, 2009.

T. Andritsch, A. Lunding, P.H.F. Morshuis, H. Negle and J.J. Smit. "A lightweight alternative to conventional insulation materials: Syntactic Foam". In *Proceedings of the 21st Nordic Insulation Symposium*, Göteborg, Sweden, 2009.

R. Kochetov, T. Andritsch, U. Lafont, P.H.F. Morshuis, J.J. Smit. "The Thermal Conductivity in Epoxy - Aluminum Nitride and Epoxy - Aluminum Oxide Nanocomposite Systems", In *Nordic Insulation Symposium (Nord-IS 09)*, Gothenburg, Sweden, pp. 27-30, June 15-17, 2009.

T. Andritsch, R. Kochetov, Y.T. Gebrekiros, U. Lafont, P.H.F. Morshuis and J.J. Smit. "Space Charge Accumulation in Epoxy based Magnesium

Oxide and Boron Nitride Nanocomposites". In *Proceedings of the 16th international symposium on high voltage engineering*, Capetown, South Africa, 2009.

T. Andritsch, R. Kochetov, P.H.F. Morshuis and J.J. Smit. "Comparison of the dielectric response of Alumina-epoxy composites with nano- and conventional sized filler". In *Proceedings of the 16th international symposium on high voltage engineering*, Capetown, South Africa, 2009.

T. Andritsch, R. Kochetov, Y.T. Gebrekiros, U. Lafont, P.H.F. Morshuis and J.J. Smit. "Synthesis and Dielectric Properties of Epoxy based Nanocomposites". In *Annual Report Conference on Electrical Insulation and Dielectric Phenomena*, Virginia Beach, USA, 2009.

R. Kochetov, T. Andritsch, U. Lafont, P.H.F. Morshuis, J.J. Smit. "Thermal Conductivity of Nano-filled Epoxy Systems", In *IEEE Conference on Electrical Insulation and Dielectric Phenomena (CEIDP)*, Virginia Beach, Virginia, USA, October 18-21, 2009.

R. Kochetov, T. Andritsch, U. Lafont, P.H.F. Morshuis, J.J. Smit. "Effects of Inorganic Nanofillers and Combinations of them on the Complex Permittivity of Epoxy-based Composites", In *IEEE International Symposium on Electrical Insulation (ISEI)*, San Diego, California, USA, June 6-9, 2010.

R. Kochetov, T. Andritsch, P.H.F. Morshuis, J.J. Smit. "Thermal and Electrical Behaviour of Epoxy Based Microcomposites Filled with Al_2O_3 and SiO_2 Particles", In *IEEE International Symposium on Electrical Insulation (ISEI)*, San Diego, California, USA, June 6-9, 2010.

T. Andritsch, R. Kochetov, Y.T. Gebrekiros, P.H.F. Morshuis and J.J. Smit. "Short term DC Breakdown Strength in Epoxy based BN Nano- and Microcomposites". In *Proceedings of the 10th IEEE International Conference on Solid Dielectrics*, Potsdam, Germany, July 2010.

T. Andritsch, R. Kochetov, P.H.F. Morshuis and J.J. Smit. "Dielectric Properties and Space Charge Behavior of MgO-Epoxy Nanocomposites". In *Proceedings of the 10th IEEE International Conference on Solid Dielectrics*, Potsdam, Germany, July 2010.

P.H.F. Morshuis, T. Andritsch, R. Kochetov, M.F. Fréchette, H.D. Martinez, S. Savoie, A. Krivda, L.E. Smith and D. Zegarac. "Dielectric Frequency Response of Epoxy-based Composites with Various Silica Filler Sizes". In *Proceedings of the 10th IEEE International Conference on Solid Dielectrics*, Potsdam, Germany, July 2010.

M.F. Fréchette, A. Vijn, L. Utracki, M.L. Trudeau, A. Sami, C. Laurent, P.H.F. Morshuis, T. Andritsch, R. Kochetov, A. Vaughan, E. David, J. Castellon, D. Fabiani, S. Gubanski, J. Kindersberger, C. Reed, A. Krivda, J. Fothergill, S. Dodd, F. Guastavino and H. Alamdari. "Nanodielectrics - A Universal Panacea for Solving All Electrical Insulation Problems?" In *Proceedings of the 10th IEEE International Conference on Solid Dielectrics*, Potsdam, Germany, July 2010.

T. Andritsch, R. Kochetov, P.H.F. Morshuis and J.J. Smit. "Short term DC Breakdown and Complex Permittivity of Al₂O₃- and MgO-Epoxy Nanocomposites". In *Annual Report Conference on Electrical Insulation and Dielectric Phenomena*, West Lafayette, IL, USA, October 2010.

T. Andritsch, R. Kochetov, P.H.F. Morshuis and J.J. Smit. "DC Conduction in Epoxy based Nano- and Mesocomposites". In *Annual Report Conference on Electrical Insulation and Dielectric Phenomena*, West Lafayette, IL, USA, October 2010.

T. Andritsch, R. Kochetov, P.H.F. Morshuis and J.J. Smit. "Short term DC Breakdown and Complex Permittivity of Al₂O₃- and MgO-Epoxy Nanocomposites". In *Annual Report Conference on Electrical Insulation and Dielectric Phenomena*, West Lafayette, IL, USA, October 2010.

R. Kochetov, T. Andritsch, P.H.F. Morshuis and J.J. Smit. "Dielectric Response and Thermal Conductivity of Epoxy Resin filled with Nanoa-

lumina Particles of Different Size in α , γ and δ Phase". In *Annual Report Conference on Electrical Insulation and Dielectric Phenomena*, West Lafayette, IL, USA, October 2010.

R. Kochetov, T. Andritsch, P.H.F. Morshuis and J.J. Smit. "Effect of Filler Size on Complex Permittivity and Thermal Conductivity of Epoxy-based Composites filled with BN Particles". In *Annual Report Conference on Electrical Insulation and Dielectric Phenomena*, West Lafayette, IL, USA, October 2010.

ACKNOWLEDGEMENTS

Writing a thesis is often considered a solitary act. However, there are a lot of persons involved in the process of writing a thesis, some without even noticing it.

First of all, I would like to express my gratitude to my promotor prof. Johan Smit, for giving me the opportunity to work in this department and his advice in times when I was getting lost in details.

Of great importance for this work was my supervisor dr. Peter Morshuis. I am deeply grateful for his guidance during the last four years and the inspiration I could draw from him.

I also want to thank prof. Picken from Delft ChemTech for his support and prof. Muhr from the TU Graz, who encouraged me to go to the Netherlands in 2006.

It was a great pleasure to work within the framework of the Triumvirate group, which funded this research, chaired by Dipl.-Ing. Hans Negle and later Dipl.-Ing. Arne Lunding. I want to express my gratitude to the Triumvirate members, who showed patience with me in the beginning and shared their ideas since day one. I also want to express my appreciation to the experts on nanodielectris, with whom I had fruitful discussions at various conferences and the *brainstorm at the institute*: D. Fabiani, prof. J. Fothergill, M. Frechette, A. Krivda, prof. K. Nelson, S. Rätzke, prof.

C. Reed and prof. A. Vaughan among others.

I would like to thank my colleagues - Gautam, Jur, Lukasz, Mo, Pantelis, Qikai, Rogier, Roy, Winnie and Xiaolin - at the high voltage group for generating a splendid working environment. Special thanks to my friend and comrade Roman, who spent the better part of one and a half years with me in the laboratories of DCT on our search for nanomaterials. Your determination (or stubbornness) was an inspiration in times when not everything worked out as planned. Fellow geek (and now prof.!) Dhiradj, thank you for everything you helped me with ever since I arrived in Delft and the insights into Dutch culture. Fellow globetrotter Tom, thanks for all the distractions at 3 p.m. and after working hours. Many thanks also to Barry, who helped me out with space charge measurements, and Yonas, who destroyed a lot of nanomaterials on my behalf. And Piotr, my long-time neighbour, thanks for not stealing *all* of my chocolate (j/k).

I am also in debt of Aad van der Graaf, Bertus Naagen, Wim Termorshuizen and ing. Paul van Nes of the high voltage laboratory, as well as Ben Norder and ing. Marcel Bus of Delft Chemtech. Their experience and advice was fundamental for my research and can't be stressed out strong enough.

I also want to thank my friends, who made the last four years a breeze and helped me keep my sanity intact: Adolfo, Dana, Javier, Joanna, Joe, Katka, Kedar, Lina, Nirali and Vera just to name a few.

Finally I want to thank my family for their support. Meinen Eltern Inge und Viktor. Nicht zuletzt dafür, dass sie mein HTL-Anmeldeformular falsch ausgefüllt haben, wodurch ich überhaupt erst in der E-Technik gelandet bin. Olga für die andauernde Unterstützung und die allwöchentlichen Anrufe. Opensource-Rebell Kevin und mindestzeit-Studierer Pascal für den ganz normalen Wahnsinn. Trudi, Hilda, Eva, Helga und Lea dafür, dass sie bis nach Holland gekommen sind, um mich im Pinguin-Anzug zu sehen.

This work was written with MiKTeX, using the T_EXnicCenter. Software used for calculations, figures and illustrations: Matlab, Reliasoft Weibull, QtiPlot, Adobe Illustrator, Microsoft Powerpoint, Microsoft Excel and the Windows Calculator.

CURRICULUM VITAE



Thomas Andritsch was born on the 17th of August 1980 in Innsbruck, Austria. He achieved his secondary school degree with distinction at the HTL Innsbruck Anichstrasse vocational school of engineering from 1994 to 1999. He received his diploma in electrical engineering from the Graz University of Technology in 2006 with honors, specializing in energy management technology. Title of his diploma thesis is '*Nanotechnology in Power Engineering*'.

He started his Ph.D. research project on nanocomposites for HVDC applications in 2006. The research was conducted at the High Voltage group of Delft University of Technology, in cooperation with Delft ChemTech and funded by industry partners of the Triumvirate group.

